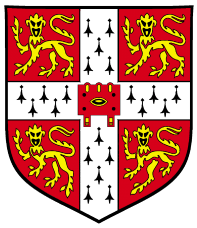

University of Cambridge
Department of Chemistry

Computer simulation and theoretical prediction of thermally induced polarisation

This dissertation is submitted to the University of Cambridge
for the degree of Doctor of Philosophy

Peter Wirnsberger
Selwyn College
May 2018

Abstract

Computer simulation and theoretical prediction of thermally induced polarisation

Peter Wirnsberger

In this thesis, we study the phenomenon of thermally induced polarisation using a combination of theory and computer simulation. Molecules of sufficiently low symmetry exhibit thermo-molecular orientation when subjected to a temperature gradient, leading to considerable electrostatic fields in polar liquids. Here, we first use non-equilibrium molecular dynamics simulations to study this interesting effect numerically. To this end, we propose an integration algorithm to impose a constant heat flux in simulations and show that it greatly improves energy conservation compared to a previous algorithm. We next investigate the thermal polarisation of water and find that truncation of electrostatic interactions can lead to severe artefacts, such as the wrong sign of polarisation and an overestimation of the electric field. We further show that the quadrupole-moment contribution to the electric field is significant and responsible for an inversion of its sign. To facilitate the theoretical description of electrostatic interactions, we propose a new dipolar model fluid as a perturbation of a Stockmayer fluid. Using this modified Stockmayer model, we provide numerical evidence for the recently proposed phenomenon of thermally induced monopoles. We show that the electrostatic field generated by a pair of heated/cooled colloidal particles immersed in such a solvent can be trivially described by two Coulomb charges. Finally, we propose a mean-field theory to predict the thermo-polarisation effect exhibited by our model fluid theoretically, and demonstrate near quantitative agreement with simulation results.

Declaration

The work described in this dissertation was carried out by the author in the Department of Chemistry at the University of Cambridge between April 2014 and May 2018 under the supervision of Professor Daan Frenkel.

This dissertation is the result of my own work and includes nothing which is the outcome of work done in collaboration except as declared in the Preface and specified in the text.

It is not substantially the same as any that I have submitted or is being concurrently submitted for a degree or diploma or other qualification at the University of Cambridge or any other University or similar institution except as declared in the Preface and specified in the text. I further state that no substantial part of my dissertation has already been submitted or is being concurrently submitted for any such degree, diploma or other qualification at the University of Cambridge or any other University or similar institution except as declared in the Preface and specified in the text.

It does not exceed the prescribed word limit for the relevant Degree Committee.

Peter Wirnsberger
May 2018

Acknowledgements

The past four years have been a truly exciting and stimulating episode of my life and there are many people whom I would like to thank for this experience.

I would first like to thank my supervisor Professor Daan Frenkel. From the day I first entered his office, he has treated me like a fully fledged researcher and given me the freedom to explore my own ideas. His fine sense of humour and his inexhaustible interest in science have shown me how much fun research can be. I would further like to thank Professor Christoph Dellago, who has co-supervised the project and supported me in many ways throughout my PhD. He has been a great source of inspiration to me ever since I attended my first lecture at the University of Vienna. I would also like to express my deepest gratitude to Dr Aleks Reinhardt for his immense support and the exciting collaboration that led to the last chapter of this thesis. To all co-authors of my publications, I am grateful for their help and the time they invested in our research. I also acknowledge funding from the Austrian Academy of Sciences, the Erwin Schrödinger Institute for Mathematics and Physics, and the Cambridge Philosophical Society with gratitude.

Understanding the electrostatics involved in this work has been a challenge and I would like to thank Professors Martin Neumann and Michiel Sprik, and Drs Chao Zhang and Stephen Cox for many discussions on Ewald summation and finite-field simulations. Without their help I would have got deeply lost in reciprocal space. I am grateful also to Drs Raman Ganti and Oliver Strickson, Ms Chongli Qin and Mr Lukas Wutschitz for many discussions and for sharing the excitement and frustration involved in our work. To current and former colleagues and the Downing Lunch Group, I am grateful for stimulating discussions. I would especially like to thank Drs Anđela Šarić, Tine Curk, Stefano Martiniani, Carl Poelking, Robert Jack, Jacob Stevenson, Andy Ballard and Mr Clemens Moritz.

Finally, I would like to thank my family for their support. They have always believed in me and encouraged me no matter what I was pursuing. I consider myself extremely lucky to have grown up in such a precious environment. To my future wife Hiroe, thank you for all your help and wisdom, and for listening to my complaints.

Le mieux est l'ennemi du bien.

VOLTAIRE

Publications

Chapter 2

P. Wirnsberger, D. Frenkel and C. Dellago. *An enhanced version of the heat exchange algorithm with excellent energy conservation properties*. J. Chem. Phys. **2015**, 143 (12), 124104.

Chapter 3

P. Wirnsberger, D. Fijan, A. Šarić, M. Neumann, C. Dellago and D. Frenkel. *Non-equilibrium simulations of thermally induced electric fields in water*. J. Chem. Phys. **2016**, 144 (22), 224102.

Chapter 4

P. Wirnsberger, D. Fijan, R. A. Lightwood, A. Šarić, C. Dellago and D. Frenkel. *Numerical evidence for thermally induced monopoles*. Proc. Natl. Acad. Sci. U. S. A. **2017**, 114 (19), 4911–4914.

Chapter 5

P. Wirnsberger, C. Dellago, D. Frenkel and A. Reinhardt. *Theoretical prediction of thermal polarisation*. arXiv:1804.03624 **2018** (accepted for publication in Phys. Rev. Lett.).

Other Publications

I have also contributed to the following publication during my PhD:

T. Curk, P. Wirnsberger, J. Dobnikar, D. Frenkel and A. Šarić. *Controlling cargo trafficking in multicomponent membranes*. arXiv:1712.10147 **2018** (accepted for publication in Nano Letters).

Contents

1

Introduction

In this thesis, we study the behaviour of polar liquids far from thermal equilibrium using a combination of theory and computer simulation. Thermally induced non-equilibrium effects have been an active field of research for more than a century [1,2] with a wide range of interesting applications on the micro- and nanoscale [3–6]. In mixtures or solutions, for example, a temperature gradient can exert forces on particles, giving rise to thermophoresis. Different particles experience different thermophoretic forces so that the effect can be utilised to achieve mass separation [1,2]. However, the magnitude of the thermophoretic drift velocity and even the direction of motion, i.e. whether a particle moves parallel or antiparallel to the temperature gradient, have proved challenging to predict so that even small changes in the experimental parameters, like salt and solvent concentration, can flip the direction of motion [6]. Computer simulations allow for tuning interactions precisely and individually [7] and therefore provide a valuable tool for understanding the microscopic driving forces involved.

In recent years, thermophoresis has gained significant research attention for its potential to drive self-propelled motion of microswimmers [5]. Metal-capped Janus particles represent one experimental realisation of such a microswimmer [8]. Under optical illumination with a laser, this type of Janus particle exhibits directed and self-propelled motion due to its asymmetric heat absorption that generates a local temperature gradient and drives flow in the vicinity of the particle [8–11]. The ability to actuate nanomotors and transport cargo on the nanoscale is of great practical interest for drug delivery, and poses one of the key challenges in nanoscience [5,12]. Another important question in nanotechnology is how to drive flow efficiently on the micro- and nanoscale [13]. A temperature gradient is known to affect interfacial stresses near a solid surface, which can lead to thermo-osmotic slip or, similarly, thermo-osmotic flow within a microchannel [6,14]. Understanding the physical mechanisms involved in

these processes is of practical interest for nanofluidic devices, where the size reduction down to the nanoscale opens a range of new possibilities and promising functionalities in biotechnology[13].

In addition to their important role in self-propelled motion, metal nanoparticles (NPs) have received considerable attention recently for their ability to heat a volume of fluid locally[15–17]. Metal NPs as heaters have the advantage that their energy absorption can be controlled precisely using visible and infrared light, and that the total amount of heat generated is relatively easy to estimate[16]. The supplied heat diffuses from the NP to the surrounding medium, where it induces a temperature gradient. These 'nano-heaters' have promising biomedical applications, for example in cancer therapy[16], and are well suited to the study of thermally induced non-equilibrium phenomena[17]. NPs immersed in dilute suspensions have also been shown to have surprising effects on heat transfer properties compared to the bulk fluid[18]. Experiments on ethylene glycol, for example, suggest a significant increase in the thermal conductivity upon dispersion of copper NPs at very low volume fractions[19,20]. Although the precise physical origin of this anomalous increase is still unclear, the improved heat transfer properties are interesting for the design of more efficient cooling systems[18,21–23]. A related challenge is the efficient conversion of waste heat into electrical power or the conversion of electrical power into heating or cooling. The physical mechanism underlying the former is the Seebeck effect while the latter is based on the Peltier effect. Experimentally, both conversions can be achieved by nanoscale thermoelectric devices based on semiconductor systems[24].

The research interest in thermo-electric effects is not limited to solids but also extends to polar liquids and electrolytes[11,25–30], where these effects have been shown to affect complex non-equilibrium interactions to a significant extent[25,27]. In colloidal suspensions in an electrolyte, for example, thermophoretic forces can lead to a charge separation of positive and negative ions and thereby generate a macroscopic thermo-electric field[25]. If a colloidal particle carries a finite charge, it will couple to the electric field generated by the ions so that the particle experiences a dragging force. In agreement with experimental results, this mechanism was demonstrated to be the predominant cause of thermophoretic motion of colloids in an electrolyte[25]. However, even a pure electrolyte can exhibit interesting thermo-electric behaviour. If a small volume of the electrolyte is heated locally, for example using metal NPs, phoretic motion of the ions leads to a charge accumulation close to the heat source[27]. Interestingly, this 'thermo-charge' generates an electric field that decays as $1/r^2$ and is therefore long-ranged[27]. Theoretical estimates of the charge suggest that it may be as high as hundreds of elementary charges if the substance is heated by 10 K

compared to the bulk temperature, and therefore of relevance to thermal actuation of colloidal suspensions and electrolytes[29].

While the thermo-charge discussed above arises due to the phoretic motion of ions in the electrolyte, thermo-electric fields can occur even in pure polar liquids, such as water, in the absence of any free charges[26]. Numerical simulations revealed that a range of polar and non-polar liquids experience thermo-molecular orientation when subjected to a temperature gradient, indicating a generic non-equilibrium phenomenon exhibited by fluids of sufficiently low symmetry[31]. If molecules carry a dipole moment, the thermo-orientation of dipoles polarises the solvent and generates an electric field. This phenomenon, termed the 'thermo-polarisation' (TP) effect, was discovered a decade ago[26] and is clearly more general than the one observed in an electrolyte, as it occurs even in the absence of ions. Since its discovery, the TP effect has attracted considerable research attention[26,28,30–37], but only moderate progress has been made towards understanding the physical origin of this fascinating effect. Theoretical approaches to explaining thermal polarisation are typically based on phenomenological equations[26,28,31–35] and involve phenomenological coefficients whose estimation requires expensive computer simulations. Recent theoretical advances, however, have provided new insights into this complex non-equilibrium phenomenon. Firstly, a mean-field treatment has been demonstrated to capture the scaling of the thermo-orientation as a function of molecular asymmetry correctly for the case of a simple liquid[30]. Secondly, it has been shown theoretically that the TP effect gives rise to an apparent thermo-charge that generates a long-range electric field[38]. This interesting observation implies that, in principle, it should be possible to map the entire solvent-mediated net electrostatic force due to the temperature gradient, say in water, on to a much simpler macroscopic arrangement of these thermally induced monopoles. We therefore think it is desirable to explore these recent theories in more detail, both theoretically and using computer simulations, to shed further light on this curious non-equilibrium phenomenon.

1.1 Thesis outline

We first introduce the relevant simulation techniques and algorithms typically used to study the TP effect in Chapter 2. In particular, we focus on non-equilibrium molecular dynamics (NEMD) simulations, for which we derive an improved thermostatting algorithm, its time discretisation and the underlying equations of motion from first principles. In Chapter 3, we then explore the thermal polarisation of water under the influence of a strong temperature gradient. After a brief summary of the literature,

we concentrate on the treatment of electrostatic interactions, which turned out to be particularly sensitive to truncation and were handled incorrectly in previous work. In Chapter 4, we demonstrate the existence of thermally induced monopoles numerically, using a simple model of a polar liquid, which we devised specifically for this purpose. In Chapter 5, we derive a mean-field approach to explain the TP effect exhibited by our model fluid and carry out a comparison with simulation data. Finally, we conclude with a summary and future outlook in Chapter 6.

2

Computational techniques

Preface

This chapter is based on the publication 'An enhanced version of the heat exchange algorithm with excellent energy conservation properties' by P. Wirnsberger, D. Frenkel and C. Dellago, which was published in the *Journal of Chemical Physics* (2015)[39]. A free version of the article is available for download on the arXiv (https://arxiv.org/abs/1507.07081).

The author contributions are as follows: I implemented the software, performed the simulations, analysed the data and wrote the initial draft of the manuscript. D. Frenkel, C. Dellago and I designed the research together and wrote the final version of the manuscript.

2.1 Simulating a thermal gradient

In atomistic simulations, a temperature gradient is typically studied either directly using NEMD[40] or indirectly using equilibrium MD simulations, often in combination with Linear Response Theory[41]. Here, we focus on the former because the method is straightforward to employ for our purposes and allows for direct comparison with existing literature on the TP effect[26].

In NEMD studies of heat conduction, an external field is applied to the system thereby driving it to a steady state. The nature of the coupling between the external field and the system differs between algorithms and determines whether a spatially homogeneous state[42], a temperature gradient[43–45] or a heat flux is imposed[46–49]. A suitable algorithm for a particular application depends on its ability to model the underlying physics correctly. If energy is supplied at a constant rate in an experiment, for example metal NPs under optical illumination[16], a thermostat which imposes

a heat flux would lend itself for the simulation. From a computational point of view, generating a flux might be preferable, because it is simpler to measure the temperature than the heat flux.

One way to generate a heat flux in computer simulations involves swapping kinetic energy between two subdomains of the simulation box[46,47]. In the heat exchange (HEX) algorithm developed by Ikeshoji and Hafskjold[46,50], a specific amount of heat is periodically removed from one subdomain or reservoir, and supplied to the other. These two regions thus act as a heat sink and source, respectively. The HEX method adjusts the non-translational kinetic energy by velocity rescaling while preserving the individual center of mass velocities of the two heat reservoirs. Other methods use different procedures to generate heat fluxes. In the reverse NEMD (RNEMD) method developed by Müller-Plathe[47], the heat transfer is established by continuously identifying hot and cold particles inside the reservoirs and exchanging their momenta. Extensions of the RNEMD method were proposed by Kuang and Gezelter[48,49], who replaced the momenta swaps by velocity rescaling moves. The velocity scaling and shearing (VSS) RNEMD method[49] allows for imposing a momentum flux in addition to the thermal flux. However, we note that in the absence of any momentum flux, the method is identical to the HEX algorithm. Although these methods are widely applicable, they all lack an attractive feature which is a formulation based on time continuous equations of motion. Knowing the equations of motion is advantageous, for example, if one is interested in studying system properties such as phase space compressibility or the development of accurate integration schemes.

Due to its simplicity, the HEX algorithm is an attractive choice for simulating a fluid in the absence of solid inhomogeneities. Since the same amount of energy is added and removed, one would expect the algorithm to conserve the total energy exactly. However, as pointed out in one of the original papers[50] and subsequent work[51], numerical implementations of the algorithm lead to a considerable energy drift over simulation time scales of a few nanoseconds. A change in total energy of several percent of the initial value was considered acceptable in past work. Nevertheless, the energy drift is a severe restriction limiting the accessible simulation time scales. Remedies to this problem either involve employing a smaller timestep or compensating the energy drift with an additional thermostat[52] which is undesirable, because such thermostats may affect the very temperature profile that one aims to study.

In this chapter, we identify the underlying cause of the energy loss and suggest a new algorithm to achieve improved energy conservation. The chapter is organised as follows: In Sec. 2.2, we summarise the HEX algorithm and its numerical implementation. We then show that the integration scheme leads to an unphysical energy drift.

In order to understand the origin of this problem, we derive the equations of motion for continuous time in Sec. 2.3. This allows us to express the integration scheme as a Trotter factorisation of the Liouville operator. In Sec. 2.4, we work out the leading-order error term of the employed operator splitting. Based on our analysis, we propose an enhanced algorithm in Sec. 2.5 and compare the results in Sec. 2.6.

2.2 Heat exchange algorithm

The goal of the HEX algorithm is to impose a constant heat flux onto the system. This is accomplished by adding heat ΔQ_{Γ_k} at each timestep to N_Γ pair-wise disjoint subdomains Γ_k, of the simulation box Ω (Fig. 2.1). Heat is subtracted if ΔQ_{Γ_k} is negative. We label those parts of the simulation box which are not thermostatted with Γ_0. The box contains N atoms each labelled with a unique index. If there is no net energy flux into the simulation box as we assume here, i.e. $\sum_k \Delta Q_{\Gamma_k} = 0$, the system will approach a steady state in which heat fluxes are established between the subdomains. The position and velocity vectors of atom i are $\boldsymbol{r}_i$ and $\boldsymbol{v}_i$, respectively. Furthermore, we use $\boldsymbol{v}_{\Gamma_k}$ and $\boldsymbol{v}_\Omega$ to denote the centre of mass velocities of the regions Γ_k and the box Ω, respectively.

2.2.1 Energy supply

Energy is added or removed by rescaling the velocities of all particles contained in region Γ_k by the same factor ξ_k and shifting them by a constant. The value of ξ_k is chosen such that the non-translational kinetic energy of that region,

$$\mathcal{K}_{\Gamma_k} = \sum_{i \in \gamma_k} \frac{m_i v_i^2}{2} - \frac{m_{\Gamma_k} v_{\Gamma_k}^2}{2}, \tag{2.1}$$

changes by ΔQ_{Γ_k} leaving $\boldsymbol{v}_{\Gamma_k}$ unchanged, where m_{Γ_k} is the total mass contained in Γ_k. The time-dependent index set γ_k comprises all particles which are located in Γ_k. Particles outside any thermostatted region are not affected by this procedure. For the individual region Γ_k, the velocity update can be formulated as[46,53]

$$\boldsymbol{v}_i \mapsto \bar{\boldsymbol{v}}_i = \xi_k \boldsymbol{v}_i + \big(1 - \xi_k\big)\boldsymbol{v}_{\Gamma_k}, \tag{2.2}$$

where the rescaling factor is given by

$$\xi_k = \sqrt{1 + \frac{\Delta Q_{\Gamma_k}}{\mathcal{K}_{\Gamma_k}}}. \tag{2.3}$$

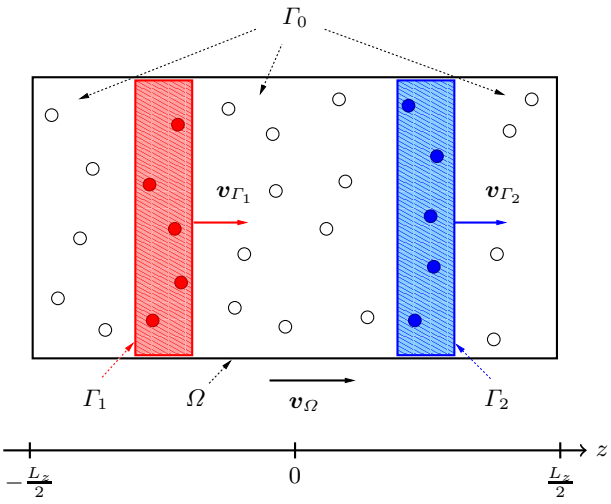

Figure 2.1: Illustration of the simulation box, Ω, with Hamiltonian regions, Γ_0, a hot region, Γ_1 (red), and a cold region, Γ_2 (blue). The centre of mass velocities of Ω, Γ_1 and Γ_2 are $\boldsymbol{v}_\Omega$, $\boldsymbol{v}_{\Gamma_1}$ and $\boldsymbol{v}_{\Gamma_2}$, respectively. Atoms are represented by red/blue circles, if they are located in the hot/cold region and by empty circles otherwise.

Here, updated quantities are denoted with an overbar. It can easily be verified that the update step given by Eq. (2.2) satisfies $\bar{\mathcal{K}}_{\Gamma_k} = \mathcal{K}_{\Gamma_k} + \Delta Q_{\Gamma_k}$ and $\bar{\boldsymbol{v}}_{\Gamma_k} = \boldsymbol{v}_{\Gamma_k}$. Since there is no net energy flux into the system according to our assumptions, this also implies that the total system energy E remains constant.

We note that the above formulation of the velocity update as presented by Aubry *et al.*[53] is simpler than the one which was originally proposed by Ikeshoji and Hafskjold[46]. In the latter case, ξ_k is a more complex function of the velocities, but it is easy to see that both formulations are equivalent.

2.2.2 Time integration

In order to keep track of the time evolution, it is convenient to introduce some additional notation. We label all quantities sampled at time $t = n\Delta t$ with a superscript n, where Δt is the timestep. In addition we define ξ_0 to be unity at all times and $k(\boldsymbol{r}_i)$ to be the index of the region in which particle i is located. The current state of the system is fully described by a $6N$-dimensional vector $\boldsymbol{x} = (\boldsymbol{r}, \boldsymbol{v})$ in phase space, where the vectors $\boldsymbol{r}$ and $\boldsymbol{v}$ contain all particle positions and velocities,

respectively. The HEX algorithm for velocity Verlet can then be formulated as

$$\bar{\boldsymbol{v}}_i^n = \xi_{k(\boldsymbol{r}_i)}^n \boldsymbol{v}_i^n + \left(1 - \xi_{k(\boldsymbol{r}_i)}^n\right) \boldsymbol{v}_{\Gamma_{k(\boldsymbol{r}_i)}}^n, \tag{2.4a}$$

$$\bar{\boldsymbol{v}}_i^{n+\frac{1}{2}} = \bar{\boldsymbol{v}}_i^n + \frac{\Delta t}{2m_i} \boldsymbol{f}_i^n, \tag{2.4b}$$

$$\boldsymbol{r}_i^{n+1} = \boldsymbol{r}_i^n + \Delta t \; \bar{\boldsymbol{v}}_i^{n+\frac{1}{2}}, \tag{2.4c}$$

$$\boldsymbol{f}_i^{n+1} = -\nabla_{\boldsymbol{r}_i} \, U(\boldsymbol{r}) \, |_{\boldsymbol{r}=\boldsymbol{r}^{n+1}} \, , \tag{2.4d}$$

$$\bar{\boldsymbol{v}}_i^{n+1} = \bar{\boldsymbol{v}}_i^{n+\frac{1}{2}} + \frac{\Delta t}{2m_i} \boldsymbol{f}_i^{n+1}, \tag{2.4e}$$

$$\boldsymbol{v}_i^{n+1} = \bar{\xi}_{k(\boldsymbol{r}_i)}^{n+1} \bar{\boldsymbol{v}}_i^{n+1} + \left(1 - \bar{\xi}_{k(\boldsymbol{r}_i)}^{n+1}\right) \bar{\boldsymbol{v}}_{\Gamma_{k(\boldsymbol{r}_i)}}^{n+1}, \tag{2.4f}$$

where $U(\boldsymbol{r})$ is the potential energy and $\boldsymbol{f}_i$ the force acting on particle i. For the entire scheme to be symmetric, half the energy is supplied at the beginning of the timestep and the other half at the end. The scaling factors $\xi_{k(\boldsymbol{r}_i)}^n$ and $\bar{\xi}_{k(\boldsymbol{r}_i)}^{n+1}$ are evaluated using Eq. (2.3) at the states $\left(\boldsymbol{r}^n, \boldsymbol{v}^n\right)$ and $\left(\boldsymbol{r}^{n+1}, \bar{\boldsymbol{v}}^{n+1}\right)$, respectively.

We note that in the original work[46,50], the authors do not provide any details about when exactly the thermostatting step should happen. For comparison, we also tested an asymmetric version of the algorithm (HEX/a), where all the energy is supplied at the end of the timestep. In this case, the initial velocity update reduces to the identity operation.

2.2.3 Model system

We studied the energy conservation of the HEX algorithm for a Lennard-Jones (LJ) fluid using the simulation package LAMMPS (version 9Dec14)[54]. The symmetric, pairwise LJ potential is given by[7]

$$u_{\mathrm{LJ}}(r) = 4\varepsilon \left[\left(\frac{\sigma}{r}\right)^{12} - \left(\frac{\sigma}{r}\right)^{6} \right], \tag{2.5}$$

where ε is the depth of the potential and σ the effective atomic diameter. In order to rule out any effects due to simple spherical truncation of the potential, we employed a slightly modified potential which is given by[55]

$$u_{\mathrm{SF}}(r) = u_{\mathrm{LJ}}(r) - u_{\mathrm{LJ}}(r_{\mathrm{s}}) - (r - r_{\mathrm{s}}) u'_{\mathrm{LJ}}(r_{\mathrm{s}}) \tag{2.6}$$

for $r \leq r_{\mathrm{s}}$ and zero otherwise, where r_{s} is the cutoff. From the functional form of Eq. (2.6) it is clear that $u_{\mathrm{SF}}(r)$ and $u'_{\mathrm{SF}}(r)$ are both continuous at the cutoff. We employed a value of $r_{\mathrm{s}}^* = 3$ for all simulations in this section. Quantities labelled

with an asterisk are expressed in reduced units (Appendix A.1).

2.2.4 Equilibration

The rectangular simulation box with dimensions $L_z^*/2 = L_x^* = L_y^* = 10.58$ comprised $N = 2000$ atoms resulting in a density of $\rho^* = 0.8444$. The thermodynamic conditions considered in this work are similar to those in Ref. 46. Starting from an initial lattice structure with zero linear momentum, the system was heated up to twice the target temperature of $T^* = 0.72$ and subsequently cooled down again at the same rate. The thermostatting during this initial period was achieved by velocity rescaling and the entire annealing process took 2.5×10^4 timesteps. The equations of motion were integrated with the velocity Verlet algorithm using a timestep of $\Delta t^* = 0.002$. We then increased the timestep to $\Delta t^* = 0.004$ and carried out a 2×10^5 timestep NVT simulation using a Nosé–Hoover thermostat[56,57] with a relaxation time of $\tau^* = 0.5$. During this run we computed the average system energy. Using the HEX algorithm, we then adjusted the energy of the last configuration and used it as input for another 2×10^5 timestep NVE equilibration run. This procedure allowed us to achieve an average equilibrium temperature of $T^* = (0.7200 \pm 0.0002)$. The error bar corresponds to one standard deviation of the error of the mean, the variance of which was estimated using block average analysis[7].

As a reference for the energy conservation in equilibrium, we carried out an additional set of NVE simulations at various timesteps. With the above protocol we matched the temperature of these runs to be close to the one inside the hot reservoir in the NEMD case. The average temperature was $T^* = (0.8400 \pm 0.0002)$.

2.2.5 Energy conservation

The previously equilibrated structures were subjected to a temperature gradient along the z-axis using the HEX algorithm. Always starting from the same phase space point, we varied the timestep for a fixed energy flux $\mathcal{F}_{\Gamma_k} = \Delta Q_{\Gamma_k}/\Delta t$ into the reservoir. The two thermostatted regions are centred at the points $z = \pm L_z/4$ and have a width of 2 in reduced units (Fig. 2.1). During each timestep, the heat ΔQ is taken from Γ_2 and added to Γ_1 ($\Delta Q_{\Gamma_1} = -\Delta Q_{\Gamma_2} = \Delta Q > 0$). We waited for 100 reduced time units for any transient behaviour to disappear and to allow the system to reach a steady state. The production run of 5000 reduced time units started at $t^* = 0$.

In order to capture the spatial variation of the temperature, we divided the z-axis into N_b bins. We use the notation X_j for the evaluation of a quantity X over bin j

and assign the value to the centre of the bin. The instantaneous kinetic temperature of bin j is then given by

$$T_j = \frac{2\mathcal{K}_j}{(N_j f - 3)k_\mathrm{B}}, \tag{2.7}$$

where $\mathcal{K}_j$ is the total non-translational kinetic energy of the bin, N_j the number of atoms contained in the bin and k_B Boltzmann's constant. The quantity f is the number of degrees of freedom per atom ($f_\mathrm{LJ} = 3$ and $f_\mathrm{SPC/E} = 2$). We subtracted three degrees of freedom to account for the centre of mass velocity of the bin. In the stationary state, the heat flux between the reservoirs in Fig. 2.1 is given by

$$J_{Q,z} = \frac{\Delta Q}{2\Delta t L_x L_y} = \frac{\mathcal{F}}{2L_x L_y}, \tag{2.8}$$

where the factor of 2 in the denominator accounts for the periodic setup. Considering a reference layer, this is intuitively clear, because half the supplied heat will flow to the other reservoir in the reference box and the other half to its image in the neighbouring box. The heat flux is an input parameter of the HEX algorithm, which we set to 0.15 in reduced units. The dependence of the energy loss at the final time on the timestep is shown in Fig. 2.2. From the quadratic fit, it is clear that the HEX algorithm exhibits an energy drift which scales as $\mathcal{O}(\Delta t^2)$. On the other hand, the energy was conserved perfectly well in *NVE* simulations at the peak temperature inside the hot reservoir. (The temperature profiles are discussed in Sec. 2.6.)

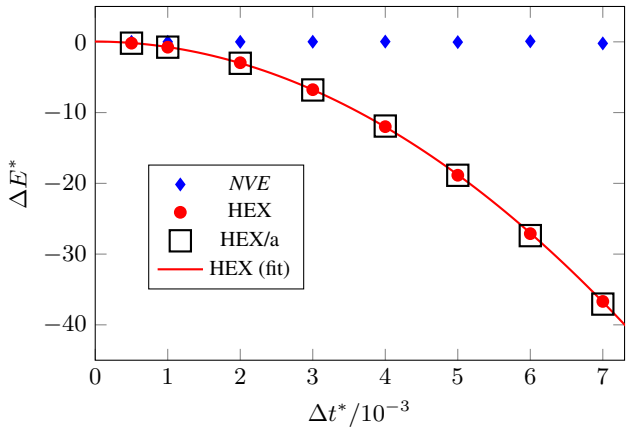

Figure 2.2: Energy loss for LJ at the final time $t^* = 5000$ as a function of the timestep. Each point in the figure corresponds to a separate simulation. The equilibrium run (blue diamonds) is compared to the symmetric (red circles) and asymmetric (black squares) versions of the HEX algorithm, respectively. A quadratic fit (red, solid line) was carried out for the symmetric version.

2.3 Equations of motion

To gain a better understanding of the energy drift of the HEX algorithm, we first derive the ordinary differential equations (ODEs) solved by the algorithm in the limit $\Delta t \to 0$. To this end we consider the velocity update for continuous time. Dropping all particle and region indices for readability and eliminating the intermediate velocities, we can cast Eq. (2.4f) into

$$\begin{aligned} \boldsymbol{v}^{n+1} = \quad & \bar{\xi}^{n+1}\left[\xi^n \boldsymbol{v}^n + (1-\xi^n)\,\boldsymbol{v}_\Gamma^n + \frac{\Delta t}{2m}\left(\boldsymbol{f}^n + \boldsymbol{f}^{n+1}\right)\right] \\ & + \left(1-\bar{\xi}^{n+1}\right)\bar{\boldsymbol{v}}_\Gamma^{n+1}. \end{aligned} \tag{2.9}$$

If we subtract $\boldsymbol{v}^n$ on both sides and divide by the timestep, we get

$$\begin{aligned} \frac{\boldsymbol{v}^{n+1}-\boldsymbol{v}^n}{\Delta t} = \quad & \frac{\bar{\xi}^{n+1}}{2m}\left(\boldsymbol{f}^n + \boldsymbol{f}^{n+1}\right) \\ + \quad & \frac{\left(\bar{\xi}^{n+1}\xi^n - 1\right)\boldsymbol{v}^n}{\Delta t} \\ + \quad & \frac{\bar{\xi}^{n+1}\left(1-\xi^n\right)\boldsymbol{v}_\Gamma^n + \left(1-\bar{\xi}^{n+1}\right)\bar{\boldsymbol{v}}_\Gamma^{n+1}}{\Delta t}. \end{aligned} \tag{2.10}$$

It is straightforward to show that

$$\frac{\left(\bar{\xi}^{n+1}\xi^n - 1\right)\boldsymbol{v}^n}{\Delta t} \to \frac{\mathcal{F}_\Gamma \boldsymbol{v}(t^n)}{2\mathcal{K}_\Gamma(t^n)}$$

and

$$\frac{\bar{\xi}^{n+1}\left(1-\xi^n\right)\boldsymbol{v}_\Gamma^n + \left(1-\bar{\xi}^{n+1}\right)\bar{\boldsymbol{v}}_\Gamma^{n+1}}{\Delta t} \to -\frac{\mathcal{F}_\Gamma \boldsymbol{v}_\Gamma(t^n)}{2\mathcal{K}_\Gamma(t^n)}$$

in the limit of $\Delta t \to 0$. From Eq. (2.4c), it is immediately obvious that the derivative of the coordinates is given by the velocities.

The continuous equations of motion solved by the HEX algorithm are therefore given by

$$\dot{\boldsymbol{r}}_i = \boldsymbol{v}_i, \tag{2.11a}$$

$$\dot{\boldsymbol{v}}_i = \frac{\boldsymbol{f}_i}{m_i} + \frac{\boldsymbol{\eta}_i}{m_i}, \tag{2.11b}$$

where the thermostatting force is defined as

$$\boldsymbol{\eta}_i = \begin{cases} m_i \frac{\mathcal{F}_{\Gamma_{k(\boldsymbol{r}_i)}}}{2\mathcal{K}_{\Gamma_{k(\boldsymbol{r}_i)}}} \left(\boldsymbol{v}_i - \boldsymbol{v}_{\Gamma_{k(\boldsymbol{r}_i)}} \right) & \text{if } k(\boldsymbol{r}_i) > 0, \\ 0 & \text{otherwise.} \end{cases} \tag{2.12}$$

In order for the equations to be well-defined, we assume that there are sufficiently many particles inside any reservoir, i.e. regions with $k(\boldsymbol{r}_i) > 0$, such that the non-translational kinetic energy never vanishes. Outside the reservoirs the thermostatting force is zero and the particles obey Hamiltonian motion. Some further properties of the equations are analysed in Appendix A.

2.4 Operator splitting

Our goal is to show that the energy drift is caused by higher-order truncation terms, which are not taken into account in the time integration. These terms can be derived easily once the integration scheme is expressed in terms of a Trotter factorisation of the Liouville operator.

2.4.1 Trotter factorisation

Tuckerman *et al.*[58] showed that reversible integrators can be generated based on a Trotter factorisation of the Liouville operator iL. Utilising the same theoretical framework, we consider the splitting

$$iL = iL_1 + iL_2, \tag{2.13a}$$

$$iL_1 = \sum_{j=1}^{N} \sum_{\alpha \in \{x,y,z\}} \frac{\eta_{j,\alpha}}{m_j} \frac{\partial}{\partial v_{j,\alpha}}, \tag{2.13b}$$

$$iL_2 = \sum_{j=1}^{N} \sum_{\alpha \in \{x,y,z\}} \left[\frac{f_{j,\alpha}}{m_j} \frac{\partial}{\partial v_{j,\alpha}} + v_{j,\alpha} \frac{\partial}{\partial r_{j,\alpha}} \right] \tag{2.13c}$$

and apply it to the current state of the system which is fully described by $\boldsymbol{x}$ in the $6N$-dimensional phase space. The exact time evolution of the system is formally given by

$$\boldsymbol{x}_{\mathrm{ex}}(t) = \mathrm{e}^{tiL} \boldsymbol{x}(0). \tag{2.14}$$

Unfortunately, it is not feasible to evaluate this expression analytically for the equations we are interested in. The problem can be simplified, however, by considering

the approximation

$$\boldsymbol{x}(t) = \left[\mathrm{e}^{\frac{\Delta t}{2}iL_1}\mathrm{e}^{\Delta t i L_2}\mathrm{e}^{\frac{\Delta t}{2}iL_1}\right]^P \boldsymbol{x}(0), \tag{2.15}$$

where P is an integral number which implicitly defines the timestep through $\Delta t = t/P$. The operator $\mathrm{e}^{\frac{\Delta t}{2}iL_1}$ acts on the velocities and adds the energy $\Delta Q/2$ to the system. In fact, as shown in Appendix A.2, the velocity update of the HEX algorithm is the exact solution of this operation. Hamilton's equations of motion are then integrated with $\mathrm{e}^{\Delta t i L_2}$ followed by the second energy supply. For the analysis in the next section, we assume that all operations in Eq. (2.15) can be carried out analytically, although in the simulation we use an additional approximation of $\mathrm{e}^{\Delta t i L_2}$, as discussed in Sec. 2.5.

2.4.2 Local truncation error

The splitting given by Eq. (2.15) is known as Strang splitting[59]. It has the local truncation error[60]

$$\boldsymbol{x}(\Delta t) - \boldsymbol{x}_{\mathrm{ex}}(\Delta t) = \Delta t^3 \mathcal{E} \boldsymbol{x}_{\mathrm{ex}}(0) + \mathcal{O}\left(\Delta t^4\right), \tag{2.16}$$

where the first term on the RHS is determined by the operator

$$\mathcal{E} = \frac{1}{12}\big[iL_2, [iL_2, iL_1]\big] - \frac{1}{24}\big[iL_1, [iL_1, iL_2]\big] \tag{2.17}$$

and $[A, B] = AB - BA$ is the commutator. Rearranging terms, we find

$$\boldsymbol{x}(\Delta t) - \Delta t^3 \mathcal{E} \boldsymbol{x}_{\mathrm{ex}}(0) = \boldsymbol{x}_{\mathrm{ex}}(\Delta t) + \mathcal{O}\left(\Delta t^4\right). \tag{2.18}$$

This means that the key to improving the accuracy of the numerical approximation is to apply the correction $-\Delta t^3 \mathcal{E} \boldsymbol{x}_{\mathrm{ex}}(0)$ to the original solution. Alternatively, we can also use a correction $-\Delta t^3 \mathcal{E} \tilde{\boldsymbol{x}}(\Delta t)$, where $\tilde{\boldsymbol{x}}(\Delta t) = \boldsymbol{x}_{\mathrm{ex}}(0) + \mathcal{O}(\Delta t)$, without changing the order of the truncation error.

2.5 Enhanced heat exchange algorithm

The analysis of the previous section remains valid for any approximation of $\mathrm{e}^{\Delta t i L_2}$ which is sufficiently accurate. This is necessarily the case if the local truncation error is $\mathcal{O}\left(\Delta t^4\right)$ or higher. Velocity Verlet integration is less accurate than that and has a local truncation error of $\mathcal{O}\left(\Delta t^3\right)$. Nevertheless, we found that it is fully sufficient to consider a coordinate correction of the form of Eq. (2.18) to get hold of the energy loss. We therefore ignored the additional velocity Verlet truncation error and all

other correction terms in Eq. (2.18) affecting velocities only.

This analysis leads us directly to the *enhanced heat exchange (eHEX)* algorithm, which is defined through the update sequence

$$\bar{\boldsymbol{v}}_i^n = \xi_{k(\boldsymbol{r}_i)}^n \boldsymbol{v}_i^n + \left(1 - \xi_{k(\boldsymbol{r}_i)}^n\right) \boldsymbol{v}_{\Gamma_{k(\boldsymbol{r}_i)}}^n, \tag{2.19a}$$

$$\bar{\boldsymbol{v}}_i^{n+\frac{1}{2}} = \bar{\boldsymbol{v}}_i^n + \frac{\Delta t}{2m_i} \boldsymbol{f}_i^n, \tag{2.19b}$$

$$\bar{\boldsymbol{r}}_i^{n+1} = \boldsymbol{r}_i^n + \Delta t \; \bar{\boldsymbol{v}}_i^{n+\frac{1}{2}}, \tag{2.19c}$$

$$\boldsymbol{f}_i^{n+1} = -\nabla_{\boldsymbol{r}_i} U(\boldsymbol{r}) \,|_{\boldsymbol{r}=\bar{\boldsymbol{r}}^{n+1}}, \tag{2.19d}$$

$$\bar{\boldsymbol{v}}_i^{n+1} = \bar{\boldsymbol{v}}_i^{n+\frac{1}{2}} + \frac{\Delta t}{2m_i} \boldsymbol{f}_i^{n+1}, \tag{2.19e}$$

$$\boldsymbol{v}_i^{n+1} = \bar{\xi}_{k(\bar{\boldsymbol{r}}_i)}^{n+1} \bar{\boldsymbol{v}}_i^{n+1} + \left(1 - \bar{\xi}_{k(\bar{\boldsymbol{r}}_i)}^{n+1}\right) \bar{\boldsymbol{v}}_{\Gamma_{k(\bar{\boldsymbol{r}}_i)}}^{n+1}, \tag{2.19f}$$

$$\boldsymbol{r}_i^{n+1} = \bar{\boldsymbol{r}}_i^{n+1} - \Delta t^3 \mathcal{E} \bar{\boldsymbol{r}}_i^{n+1}. \tag{2.19g}$$

Apart from the last integration step and some relabelling, this scheme is identical to the HEX algorithm. As shown in Appendix A, the correction term is given by

$$\begin{aligned} \mathcal{E} r_{i,\alpha} = & \frac{\eta_{i,\alpha}}{m_i \mathcal{K}_{\Gamma_{k(\boldsymbol{r}_i)}}} \left[\frac{\mathcal{F}_{\Gamma_{k(\boldsymbol{r}_i)}}}{48} + \frac{1}{6} \sum_{j \in \gamma_{k(\boldsymbol{r}_i)}} \boldsymbol{f}_j \cdot \left(\boldsymbol{v}_j - \boldsymbol{v}_{\Gamma_{k(\boldsymbol{r}_i)}} \right) \right] \\ & - \frac{\mathcal{F}_{\Gamma_{k(\boldsymbol{r}_i)}}}{12 \mathcal{K}_{\Gamma_{k(\boldsymbol{r}_i)}}} \left[\frac{f_{i,\alpha}}{m_i} - \frac{1}{m_{\Gamma_{k(\boldsymbol{r}_i)}}} \sum_{j \in \gamma_{k(\boldsymbol{r}_i)}} f_{j,\alpha} \right] \end{aligned} \tag{2.20}$$

and evaluated at the state $\bar{\boldsymbol{x}}^{n+1}$. We note that this expression vanishes for particles outside any reservoir, because the thermostatting force is zero in that case. The scaling factors $\xi_{k(\boldsymbol{r}_i)}^n$ and $\bar{\xi}_{k(\bar{\boldsymbol{r}}_i)}^{n+1}$ are calculated at the system states $\boldsymbol{x}^n$ and $\bar{\boldsymbol{x}}^{n+1}$, respectively. As in the formulation of the original algorithm, we also consider the case where all the energy is supplied asymmetrically in Eq. (2.19f). We refer to this version of the algorithm as eHEX/a.

2.5.1 Rigid molecules

Employing constraining forces, we can extend the eHEX algorithm to a system of rigid bodies, such as SPC/E water[61]. In the SHAKE algorithm[62], originally devised for Verlet integration, rigidity is imposed by solving iteratively for a set of Lagrange multipliers. If the underlying equations are integrated with the velocity Verlet algorithm, a second set of constraining forces is required to eliminate velocity components along any fixed bond. This is taken into account by the RATTLE

algorithm[63] which we implemented in LAMMPS.

To be compatible with the treatment of constraining forces in LAMMPS, we consider the eHEX/a algorithm for rigid bodies. We use RATTLE to ensure that the velocities and positions are satisfied up to the target tolerance after the second velocity update (Eq. (2.19e)). Provided that all sites of a reference molecule are located in the same region, the scaling and shifting in Eq. (2.19f) does not violate the constraints. For this reason, we only rescale an individual site of a molecule if its centre of mass is located within the reservoir.

For the small fraction of molecules inside a reservoir, the coordinate correction in Eq. (2.19g) introduces an $\mathcal{O}(\Delta t^3)$ error in the bond distances. This error is small and of the same order as the local error of the RATTLE algorithm itself[63]. For this reason, we consider an unconstrained update acceptable. However, we monitor the maximum relative errors throughout all simulations. The constraining forces for the coordinates are recalculated at the end of the timestep to ensure that the positions are correct after the subsequent velocity Verlet update.

2.5.2 Model system

In addition to the monatomic system, we tested the eHEX/a algorithm for the SPC/E water model[61]. The simulation box with dimensions $L_z/2 = L_x = L_y = 25.26$ Å contained 1024 molecules resulting in a density of 0.95 g/cm^3. We used a real-space cutoff of 11 Å for the LJ and Coulomb interactions, which were evaluated with standard Ewald summation[7]. The damping parameter was $\alpha = 6.816/L_x$ with 9841 $\boldsymbol{k}$-vectors (before employing symmetry properties of the reciprocal sum).

Starting from a lattice structure, we rescaled velocities for 10 ps to drive the system close to a target temperature of 400 K. We employed a timestep of 1 fs and the equations were integrated with velocity Verlet. This was followed by a 2×10^5 timestep NVT simulation using a Nosé–Hoover thermostat with a relaxation time of 1 ps. The total energy of the last configuration was then adjusted such that it corresponds to the average of the NVT run. The average temperature over a subsequent 2×10^5 timestep NVE simulation was (400.5 ± 0.2) K.

We then switched on the thermostat and waited for 100 ps for the system to reach a steady state before starting with the 1 ns production run. The reservoirs of width 4 Å were centred at the points $z = \pm L_z/4$ and we imposed a heat flux of 4.08×10^{10} W/m^2. As a reference for the energy conservation, we carried out an additional set of 1 ns NVE simulations at various timesteps. The temperature in these runs was (468.0 ± 0.2) K.

2.6 Results

The effect of the additional coordinate integration in the eHEX algorithm on the total energy conservation is shown in Figs 2.3–2.4. As can be seen, the new algorithm exhibits excellent energy conservation. Even for large timesteps close to the stability limit for a *NVE* simulation at the peak temperature ($\Delta t^*_{\text{max, LJ}} \approx 0.0075$ and $\Delta t_{\text{max, SPC/E}} \approx 3.5$ fs), there is no noticeable drift on this scale. The energy loss of the HEX algorithm, on the other hand, is substantial. At the largest timestep, the total system energy changed by about 0.45% for LJ and 1.6% for SPC/E, respectively. Although an energy loss of several percent was considered acceptable in the past[46,50,51], it sets an upper limit to the accessible simulation time scales. The only way to circumvent this problem apart from coupling the system to an additional thermostat is to decrease the timestep and thereby waste valuable computing time. Based on a series of eight simulations at the largest timestep and with different initial conditions, we can give a conservative estimate of the improvement due to the new algorithms. For LJ we found that the eHEX algorithm loses at least 500 times less energy than the HEX algorithm (450 for eHEX/a compared to HEX/a). For SPC/E water we found that the eHEX/a algorithm improves the energy conservation by at least a factor of 100 compared to the HEX/a algorithm. The accessible simulation time scale therefore increased by two orders of magnitude.

The spatial variation in temperature is shown in Figs 2.5–2.6. For the monatomic system, the results agree well without any marked differences (Fig. 2.5). We note that in both cases there are some visible discontinuities in the vicinity of the reservoirs.

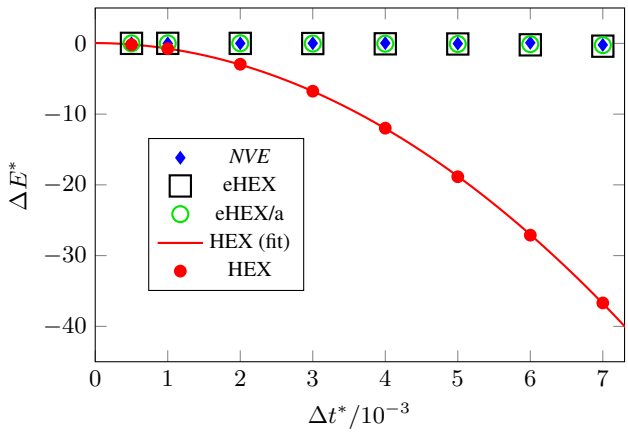

Figure 2.3: Energy loss for LJ at the final time $t^* = 5000$ for various timesteps. The equilibrium run (blue diamonds) and the symmetric (black squares) and asymmetric (green, open circles) versions of the eHEX algorithm, respectively, do not show any appreciable drift. The energy loss of the HEX algorithm (red, full circles) together with a quadratic fit (red, solid line) is shown for comparison.

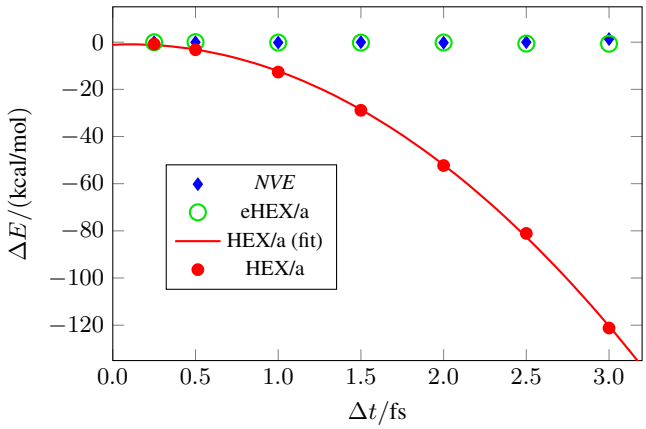

Figure 2.4: Energy loss for SPC/E water at the final time $t = 1$ ns for various timesteps. The equilibrium run (blue diamonds) is compared to the asymmetric eHEX algorithm (green, open circles) and the asymmetric HEX algorithm (red, full circles) together with a quadratic fit (red, solid line).

This should not be very surprising, since the thermostatting force is also discontinuous. We found that the gap decreases as we go to lower temperature gradients, because the fluid can dissipate the heat sufficiently fast. A possible way of controlling this gap is to employ a weight function and to redefine temperature such that it is continuous at the boundary of the reservoir[44]. This procedure allows for better control and is numerically convenient, but it is not obvious which weight function is physically most meaningful. Furthermore, generalising this approach to arbitrary reservoir shapes is challenging, because it requires some sort of signed distance information to the boundary.

For SPC/E water the energy loss at large timesteps is reflected in a slight drop of temperature (Fig. 2.6). The overall profiles agree well, but they are shifted by a few Kelvin. This shift is consistent with the energy loss of about 1% for the 2.5 fs timestep. There are no visible temperature discontinuities in the vicinity of the reservoirs. This might be related to the fact that in our scheme the boundaries are naturally smeared out as we only rescale entire molecules which could be intersected by the reservoir boundary.

Although we omitted a constrained coordinate update in the eHEX/a algorithm, the relative deviation from the ideal bond distance never exceeded 1.1×10^{-5}. This was the case for the largest timestep of 3 fs, but the error decays rapidly (with Δt^3) such that it reduced to 3.6×10^{-7} for a timestep of 1 fs. The maximum induced relative velocity along any rigid bond was an order of magnitude lower for both timesteps, respectively. Only a small fraction of molecules inside a reservoir ($\approx 16\%$) suffers from this inconsistency. We consider this error acceptable and an unconstrained update justified. An extension of the eHEX algorithm to a constrained

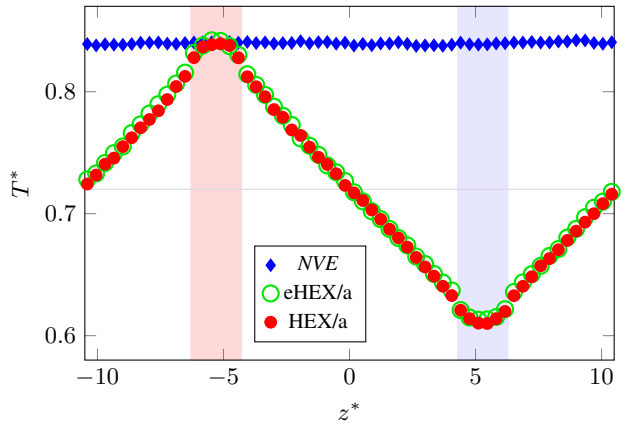

Figure 2.5: Comparison of the temperature profiles for LJ.

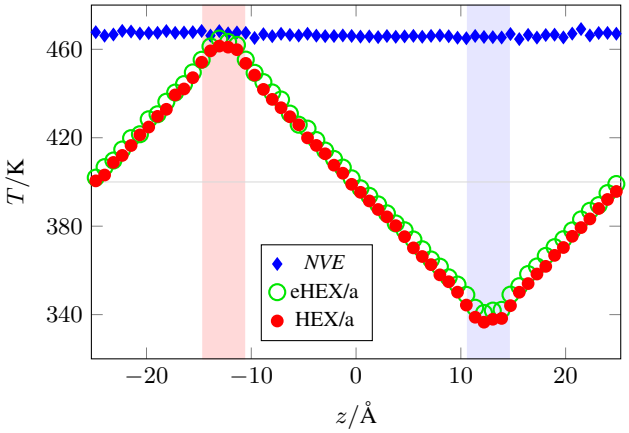

Figure 2.6: Comparison of the temperature profiles for SPC/E water.

update is possible in case higher precision is required.

With regard to conservation of total linear momentum, we found that both algorithms satisfied this condition perfectly. We initialised the linear momentum of the box to zero at the beginning and it remained close to machine precision throughout the entire simulation.

2.7 Conclusions

In this chapter, we have presented a new algorithm for NEMD simulations of thermal gradients. The method comprises an extension to the HEX algorithm, which rescales and shifts velocities of particles inside reservoirs to impose a constant heat flux. The problem with the original algorithm is that it exhibits a drift in the total energy whose origin remained hitherto unclear. For long simulations, this energy loss becomes restrictive, limiting the accessible simulation time scales to a few nanoseconds. In our approach, we reformulated the HEX algorithm as a Trotter factorisation of

the Liouville operator. Using this theoretical framework, it is straightforward to determine higher-order truncation terms which are a consequence of the employed operator splitting. We demonstrated that the leading-order truncation error of the coordinates is responsible for the observed energy drift.

To test the accuracy of the method, we implemented the eHEX algorithm in LAMMPS and ran simulations on a LJ system and SPC/E water. In both cases, we observed at least a hundredfold reduction in the energy loss compared to the HEX algorithm. With the eHEX algorithm, it is therefore possible to carry out constant heat flux simulations which are on the order of a hundred nanoseconds and based on fully deterministic equations of motion.

3

Challenges in the simulation of thermal polarisation

Preface

This chapter is based on the publication 'Non-equilibrium simulations of thermally induced electric fields in water' by P. Wirnsberger, D. Fijan, A. Šarić, M. Neumann, C. Dellago and D. Frenkel, which was published in the *Journal of Chemical Physics* (2016)[36]. A free version of the article is available for download on the arXiv (https://arxiv.org/abs/1602.02734).

The author contributions are as follows: I implemented the software, performed the simulations, analysed the data and wrote the initial version of the manuscript. M. Neumann, C. Dellago, D. Frenkel and I designed the research and interpreted the results; D. Fijan and A. Šarić helped with performing the research; A. Šarić, M. Neumann, C. Dellago, D. Frenkel and I wrote the final version of the paper.

We note that a similar article (Ref. 35) appeared online shortly before submission of our manuscript. That article is not cited in the current chapter but we included references in subsequent chapters whenever appropriate.

3.1 Motivation

Bresme and co-workers showed that the theory of non-equilibrium thermodynamics (NET) predicts a linear relationship between the temperature gradient and the thermally induced electric field in a polar medium, which is known as the TP effect[26]. Within the theoretical formalism of NET, the entropy production in the steady state is related to non-equilibrium fluxes and generalised forces[3] that are coupled by phenomenological relations. For the specific case of thermal polarisation, the

relevant fluxes were identified to be the heat flux $\boldsymbol{J}_q$ and the displacement current $\partial \boldsymbol{P}/\partial t$, where $\boldsymbol{P}$ is the polarisation[26]. The specific entropy production (per volume) can therefore be written as

$$\dot{s}_v = -\frac{1}{T}\frac{\partial \boldsymbol{P}}{\partial t} \cdot (\boldsymbol{E}_{\text{eq}} - \boldsymbol{E}) - \frac{1}{T^2}\boldsymbol{J}_q \cdot \nabla T, \tag{3.1}$$

where $\boldsymbol{E}_{\text{eq}} = \boldsymbol{P}/(\chi_e \epsilon_0)$ is the electric field present already in equilibrium, $\chi_e = \epsilon_r - 1$ is the electric susceptibility and ϵ_r and ϵ_0 are the relative dielectric constant and the vacuum permittivity[26]. We note that, without further justification, the density gradient is neglected entirely in the expression above. The phenomenological relations corresponding to Eq. (3.1) are

$$\frac{\partial \boldsymbol{P}}{\partial t} = -\frac{L_{pp}}{T}(\boldsymbol{E}_{\text{eq}} - \boldsymbol{E}) - \frac{L_{pq}}{T^2}\nabla T \tag{3.2}$$

and

$$\boldsymbol{J}_q = -\frac{L_{qp}}{T}(\boldsymbol{E}_{\text{eq}} - \boldsymbol{E}) - \frac{L_{qq}}{T^2}\nabla T, \tag{3.3}$$

where L_{pp}, L_{pq}, L_{qp} and L_{qq} are phenomenological coefficients satisfying $L_{pq} = L_{qp}$. Assuming a steady state in the absence of free charges, we have $\partial \boldsymbol{P}/\partial t = 0$ and $\boldsymbol{P} = -\epsilon_0 \boldsymbol{E}$, so that Eqs (3.2)–(3.3) yield[26]

$$\boldsymbol{E} = \left(1 - \frac{1}{\epsilon_r}\right)\frac{L_{pq}}{L_{pp}}\frac{\nabla T}{T}. \tag{3.4}$$

Using NEMD simulations, Bresme and co-workers reported electric fields as high as 10^8 V/m for gradients of 5 K/Å[28,64] and confirmed that the electric field scales linearly with the temperature gradient[28,32,64].

In molecular simulations, Coulomb interactions are regularly treated via Ewald summation[65] (including approximations to it) or a form of truncated interactions[66]. In most studies on the thermo-polarisation effect[26,28,32,64], electrostatic interactions were handled with the truncated, short-ranged Wolf method[67]. It was argued that Ewald summation can introduce artefacts, which can be avoided by using the short-ranged method[26]. Very recently, however, Bresme and co-workers found that the Wolf method overestimates the induced electric field in a spherical droplet of water by an order of magnitude compared to Ewald summation[68].

The Wolf method and other short-ranged methods[66,69–77] are attractive because they achieve linear scaling with the number of particles compared to the fastest approximations to Ewald summation, such as Particle-mesh Ewald, which scale as $\mathcal{O}(N \log N)$[78,79]. However, it is well known that truncation of long-ranged Coulomb

interactions in simulations can lead to severe artefacts[80–87]. In particular, short-ranged methods often fail for heterogeneous systems containing interfaces, even though they are known to perform well in bulk equilibrium simulations provided that the parameters are chosen carefully[83,86–88]. In simulations of the liquid–vapour interface, for example, the Wolf method was found inadequate for predicting the electrostatic potential and dipole orientations, regardless of the choice of parameters[89]. In the context of local molecular field (LMF) theory it has been demonstrated recently that averaged long-range effects can be taken into account self-consistently through an external potential[76,83]. In this approach, short-ranged interactions are modelled through a pairwise potential which bears strong similarities to the Wolf method[90]. However, in the absence of the external potential the short-ranged method failed to reproduce the correct results as obtained with Ewald summation and molecules were found to overorient[83].

In this chapter, using a full treatment of electrostatic interactions with Ewald summation we investigate the validity of the electric fields and induced orientations observed by Bresme and co-workers[26,28,32,64,68]. The field calculation requires especially careful consideration, as the large body of work published thus far relies on the formulation which is inconsistent with the dynamics of the simulation[26,28,32,64,68]. The correct calculation of the field requires a modified kernel (rather than r^{-1}) that is consistent with the effective truncated Coulomb interactions[91,92]. We discuss this issue in detail and carry out a comparison of the thermally induced fields and multipole moments as obtained both with Ewald summation and the Wolf method.

Another important aspect that deserves consideration, is the spatial averaging of the potential and the field. In order to resolve the spatial variation of these quantities, it is advantageous to consider a quasi one-dimensional setup to enhance sampling. Usually, the charge density is first spatially averaged over small slabs (bins) and then convoluted with an appropriate kernel to obtain, for example, the potential[93–96]. As a consequence, the potential calculated in this way does, in general, not represent the exact average over the individual bin. However, as we demonstrate in this chapter, calculating the exact analytical average can be done straightforwardly for both summation methods and can lead to huge reductions in the error bars for low resolutions. Therefore, this approach frees us from the constraint of employing an unnecessarily high, submolecular resolution.

The remainder of this chapter is structured as follows: In Sec. 3.2, we briefly summarise the electrostatic kernels for Ewald summation and the Wolf method, respectively, and discuss important differences using a simple model system. Then, in Sec. 3.3, we reduce the three-dimensional problem to one spatial dimension employing

symmetry properties of the setup. The two different multipole expansions considered in this chapter are derived in Sec. 3.4. The simulation protocol is explained in Sec. 3.5 and all simulation results are presented in Sec. 3.6.

3.2 Electrostatic interactions

In MD simulations, periodic boundary conditions (PBCs) are usually employed to reduce finite-size or surface effects[7]. This implies that the simulated system is infinite, but can be fully described with knowledge of the state of a reference box. The electrostatic potential, Φ, is governed by Poisson's equation,

$$\nabla^2\Phi = -4\pi\rho_q, \tag{3.5}$$

where ρ_q is the charge density and all quantities are expressed in Gaussian units. One way of determining the potential is to solve this equation directly for the fictitious infinite system. Alternatively, the task can be mapped onto the problem of finding a generalised kernel or Green's function, G, compatible with a finite volume with PBCs, considering nearest images only[97]. Once G is known, the potential and the field can then be calculated as

$$\Phi(\boldsymbol{r}) = \int_\Omega \mathrm{d}^3r'\; G(\boldsymbol{r}-\boldsymbol{r}')\rho_q(\boldsymbol{r}'), \tag{3.6}$$

and

$$\boldsymbol{E}(\boldsymbol{r}) = -\nabla\Phi(\boldsymbol{r}), \tag{3.7}$$

where Ω is the simulation box of volume V. Throughout this chapter, we assume that PBCs are explicitly taken into account whenever expressions that depend on an argument of the form $\boldsymbol{r}-\boldsymbol{r}'$ are evaluated (see for example Appendix B.1).

Although both approaches lead to the same result, there is an important conceptual difference: In the former case, we consider the infinite system of charges interacting with the potential that scales as r^{-1} (in three dimensions) plus surface term, whereas in the latter case, we only consider the charge distribution in our reference box with an effective interaction. The periodicity of the setup is then fully mimicked by the Green's function, which no longer decays as r^{-1} and is not even spherically symmetric.

Let us consider a charge-neutral system consisting of N molecules each comprising n partial charges $q_{i\alpha}$ located at positions $\boldsymbol{r}_{i\alpha}$ (i labels molecules and α sites within a

molecule). The total electrostatic energy is then given by[97,98]

$$\begin{aligned} U(\boldsymbol{R}) = \quad & \frac{1}{2}\sum_{i\neq j}\sum_{\alpha,\beta} q_{i\alpha}q_{j\beta}\; G(\boldsymbol{r}_{i\alpha j\beta}) \\ & + \frac{1}{2}\sum_{j}\sum_{\alpha\neq\beta} q_{j\alpha}q_{j\beta}\left[G(\boldsymbol{r}_{j\alpha j\beta}) - \frac{1}{r_{j\alpha j\beta}}\right] \\ & + \frac{1}{2}\sum_{j}\sum_{\alpha} q_{j\alpha}^2 \lim_{r\to 0}\left[G(\boldsymbol{r}) - \frac{1}{r}\right], \end{aligned} \tag{3.8}$$

where $\boldsymbol{r}_{i\alpha j\beta} = \boldsymbol{r}_{j\beta} - \boldsymbol{r}_{i\alpha}$ is the distance vector between the nearest pair of images, $r = |\boldsymbol{r}|$ and $\boldsymbol{R} = (\boldsymbol{r}_{11}, \ldots, \boldsymbol{r}_{Nn})$ is a $3n \times N$-dimensional vector. In the above equation we have omitted the summation bounds for readibility.

In Eq. (3.8) the surface term of de Leeuw and co-workers[91] has been omitted, because we employ conducting (tin-foil) boundary conditions. We can see that the functional form of G directly affects the forces, which are calculated from the negative gradient of the energy, and therefore the dynamics of the simulation. In what follows, we briefly summarise the kernels for Ewald summation and the Wolf method.

3.2.1 Ewald summation

Ewald summation is a numerical approximation to the exact solution of Eq. (3.5) for PBCs, whose Green's function is formally given by

$$G_{\mathrm{PBC}}(\boldsymbol{r}) = \frac{1}{V}\sum_{\boldsymbol{k}\neq\boldsymbol{0}} \frac{4\pi}{k^2} \mathrm{e}^{i\boldsymbol{k}\cdot\boldsymbol{r}}. \tag{3.9}$$

Here, the summation extends over reciprocal vectors $\boldsymbol{k}$ with components $k_\alpha = 2\pi p_\alpha / L_\alpha$, where p_α is an integer and L_α the box size in direction α. Introducing the convergence factor $\mathrm{e}^{-k^2/4\eta^2}$, the expression is split up into two terms, one of which is converted back to real space. This leads to the representation[98]

$$\begin{aligned} G_{\mathrm{E,full}}(\boldsymbol{r}) = \quad & \sum_{\boldsymbol{n}} \frac{\operatorname{erfc}(\eta|\boldsymbol{r}+\boldsymbol{n}|)}{|\boldsymbol{r}+\boldsymbol{n}|} - \frac{\pi}{\eta^2 V} \\ & + \frac{1}{V}\sum_{\boldsymbol{k}\neq\boldsymbol{0}} \frac{4\pi}{k^2} \mathrm{e}^{-\frac{k^2}{4\eta^2}} \mathrm{e}^{i\boldsymbol{k}\cdot\boldsymbol{r}}, \end{aligned} \tag{3.10}$$

where $\boldsymbol{n}$ is a shift vector between a molecule and its periodic image and the summation runs over all periodic images. Choosing η carefully, it is possible to achieve fast convergence of the first sum and small contributions for $\boldsymbol{n} \neq \boldsymbol{0}$. If we ignore these terms and introduce a spherical cutoff, r_c, for better performance, Eq. (3.10) finally

reduces to

$$G_{\mathrm{E}}(\boldsymbol{r}) = \Theta(r_{\mathrm{c}} - r)\frac{\operatorname{erfc}(\eta r)}{r} - \frac{\pi}{\eta^2 V} + \frac{1}{V}\sum_{\boldsymbol{k}\neq\boldsymbol{0}} \frac{4\pi}{k^2} \mathrm{e}^{-\frac{k^2}{4\eta^2}} \mathrm{e}^{i\boldsymbol{k}\cdot\boldsymbol{r}}, \tag{3.11}$$

where $\Theta(r)$ is the Heaviside function. Inserting this expression back into Eq. (3.8) yields the standard Ewald summation expression[97] as presented in textbooks, e.g. in Ref. 7.

3.2.2 Wolf method

Wolf and co-workers showed that in a condensed ionic system the net Coulomb potential is effectively short-ranged[67]. Based on this insight, they devised a summation method that avoids the expensive k-space term in Eq. (3.11) altogether. Instead, the potential is damped and shifted in a way that enforces charge neutrality within the cutoff sphere for improved convergence properties. The corresponding kernel is given by

$$G_{\mathrm{W}}(\boldsymbol{r}) = \Theta(r_{\mathrm{c}} - r)\left[\frac{\operatorname{erfc}(\zeta r)}{r} - \frac{\operatorname{erfc}(\zeta r_{\mathrm{c}})}{r_{\mathrm{c}}}\right] \tag{3.12}$$

and reproduces the correct Madelung energy as suggested by Wolf and co-workers[67]. Later the method was extended to eliminate also higher-order multipoles inside the cutoff sphere[73,74]. However, it was pointed out that the entire approach embodies certain assumptions on the underlying physical system[74], such as the availability of charges outside the cutoff region for screening[72]. Whether these assumptions are reasonable is not always clear a priori, especially for inhomogeneuous systems such as the one considered here.

We note that the first term in G_{W} is identical to the one in G_{E}, although the optimal choice of the damping parameter, ζ, is not necessarily the same as for Ewald summation. A good value can be found by analysing the convergence of the Madelung energy per ion[67]. Furthermore, in the Wolf method the force is not exactly given by the negative gradient of the potential energy. The reason for this inconsistency is that the expression $G'_{\mathrm{W}}(r) - G'_{\mathrm{W}}(r)|_{r=r_{\mathrm{c}}}$ is used for the evaluation rather than $G'_{\mathrm{W}}(r)$ in order for the force to vanish at the cutoff distance[67]. There are extensions of the Wolf method which address this issue (for example Ref. 70). However, given a reasonable combination of damping parameter and cutoff value, we expect the effects of this inconsistency on the electric field to be negligible.

3.2.3 Model system

To illustrate the difference between the electrostatic kernels, we consider a test case based on calculating the potential generated by a single SPC/E water[61] molecule. This simple example should draw attention to the fact that, for an identical arrangement of charges, the results for the Wolf method sensitively depend on the choice of kernel, damping parameter and cutoff radius. The quality of the Wolf approximation to the electrostatic potential, computed according to Eq. (3.6), is assessed by comparison with the results of Ewald summation, which approximates the exact solution.

Considering only a single molecule may seem atypical for the Wolf method, since it relies on the idea that long-range contributions average out in a dense system. However, this comparison serves as a guideline for the choice of new parameters which help us to reduce the dependence on this crucial assumption. This is achieved by tuning the potential to get better agreement with Ewald summation already on the level of a single molecule. The comparison in Sec. 3.6 will then allow us to assess the performance of the Wolf method for a wider range of parameters, but it is not the intention of this work to single out an optimal choice.

Figure 3.1 shows the potential due to a single SPC/E water molecule in a fully periodic system. The molecule is located at the centre of a rectangular simulation box with dimensions $L = L_x = L_y = L_z/3 = 36.35$ Å. The three charges, $q_\mathrm{O} = 0.8476 q_\mathrm{e}$ and $q_{\mathrm{H}_{1/2}} = -q_\mathrm{O}/2$, where q_e is the elementary charge, are located in the $x = 0$–plane at positions $\boldsymbol{r}_\mathrm{O} = (0, 0, -0.289)$ Å and $\boldsymbol{r}_{\mathrm{H}_{1/2}} = (0, \pm 0.816, 0.289)$ Å, respectively. Ewald summation was carried out taking $r_\mathrm{c} = L/2$ with $\eta L = 5.85$, and choosing the set of $\boldsymbol{k}$-vectors for Eq. (3.11) such that the estimated relative error of the force was approximately 10^{-5}. For the Wolf method, we compare two sets of parameters: $(\zeta L = 1.0, r_\mathrm{c} = L/2)$ and $(\zeta L = 7.2, r_\mathrm{c} = 11$ Å$)$. The latter combination was employed by Armstrong and Bresme[28] and the former with considerably weaker damping and a larger cutoff is added for comparison. We note that we also investigated the effects of a large cutoff combined with strong damping, i.e. $(\zeta L = 7.2, r_\mathrm{c} = L/2)$. However, we did not observe any substantial differences for the main results of this work compared with the 11 Å cutoff and therefore omitted the comparison.

It is obvious that for the strong damping (dashed lines) the potential decays too quickly compared to the result we get with Ewald summation (solid lines). Only the short-range behaviour in the immediate vicinity of the molecule is captured correctly. The weaker damping parameter (dotted lines), on the other hand, yields a reasonable agreement with Ewald summation within a distance of about 6 Å from the origin, but shows some deviation further away. Employing even lower values

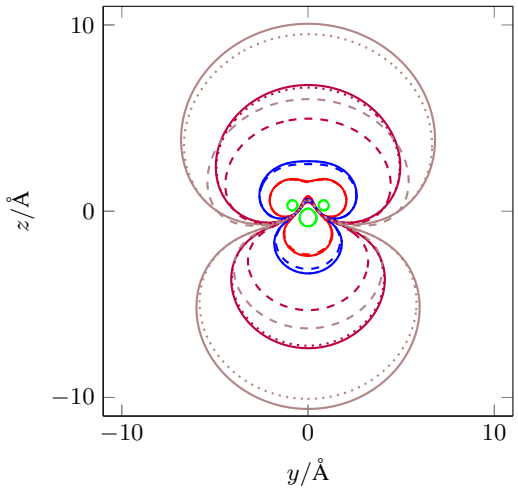

Figure 3.1: Absolute value of the electrostatic potential of a single SPC/E water molecule computed by Ewald summation (solid lines) and the Wolf method with $\zeta L = 1.0$ (dotted lines) and $\zeta L = 7.2$ (dashed lines). With increasing distance from the origin, the isolines of the potential correspond to the values 14.4 V, 1.44 V, 0.72 V, 0.144 V and 0.072 V, respectively.

for ζ, for example $0.5/L$, reduces the discrepancy between the outermost contour lines only minimally (not shown). Since the value of the potential represented by the lowest contour level in Fig. 3.1 corresponds to only 0.5% of the highest one, we conclude that the parameters ($\zeta L = 1.0, r_\mathrm{c} = L/2$) yield a reasonable approximation to the Ewald result within the cutoff sphere of 11 Å. Validation of both sets of parameters in bulk simulations also reveals good agreement with Ewald summation (see Appendix B.3).

3.3 Spatial averaging

Once the method to treat electrostatic interactions is chosen and optimised, one typically wishes to improve the statistics of the collected averages. For this purpose a simulation setup with high spatial symmetry is advantageous[28]. Here, we focus on the case where the underlying three-dimensional problem can be reduced to one spatial dimension, as illustrated in Fig. 3.2. For such a system, the average charge density can only depend on z for sufficiently long simulation times, because the system is isotropic in all other directions. Therefore, this approach is justified only if one considers sufficiently long simulations. Assuming $\rho_q(\boldsymbol{r}') \equiv \rho_q(z')$, we can then

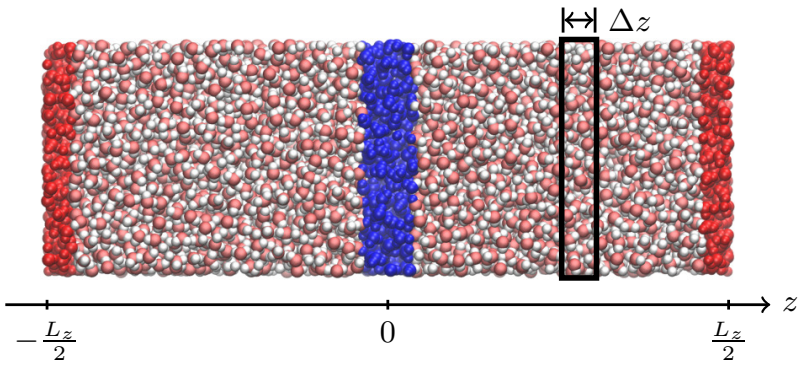

Figure 3.2: Simulation setup with a hot reservoir (coloured in red) wrapped around the boundaries and a cold reservoir (coloured in blue) in the centre of the simulation box. The superimposed rectangle (black solid lines) schematically illustrates a bin of width Δz.

rewrite Eq. (3.6) as

$$\Phi(z) = \int_{-L_z/2}^{L_z/2} \mathrm{d}z' \; G_{\mathrm{1D}}(z - z')\rho_q(z'), \tag{3.13}$$

where we introduced the one-dimensional kernel

$$G_{\mathrm{1D}}(z) = \int_{-L_x/2}^{L_x/2} \mathrm{d}x' \int_{-L_y/2}^{L_y/2} \mathrm{d}y' \; G(x - x', y - y', z). \tag{3.14}$$

Taking the negative gradient of Eq. (3.13) yields the electrostatic field

$$E_z(z) = -\int_{-L_z/2}^{L_z/2} \mathrm{d}z' \; G'_{\mathrm{1D}}(z - z')\rho_q(z'), \tag{3.15}$$

where G'_{1D} denotes the derivative of G_{1D}. The above integrals can be evaluated readily for Ewald summation and the Wolf method (see Appendix B.1). The results can be improved considerably by averaging the potential and the microscopic field over small spatial regions, such that we obtain the macroscopic Maxwell field for the latter. The centre of each control volume then represents its exact spatial average. To this end, we consider N_{b} bins of width Δz, as depicted in Fig. 3.2. The lower and upper boundaries of bin j, where $j = 1, \ldots, N_{\mathrm{b}}$, are given by $z_{j,1} = -L_z/2 + (j-1)\Delta z$ and $z_{j,2} = z_{j,1} + \Delta z$, respectively. The spatial average of the potential over bin j is

then given by

$$\bar{\Phi}_j = \frac{1}{\Delta z} \int_{z_{j,1}}^{z_{j,2}} \mathrm{d}z \; \Phi(z) \tag{3.16a}$$

$$= \int_{-L_z/2}^{L_z/2} \mathrm{d}z' \; \bar{G}_{1\mathrm{D},j}(z') \rho_q(z'), \tag{3.16b}$$

where the overbar denotes the spatially averaged kernel

$$\bar{G}_{1\mathrm{D},j}(z') = \frac{1}{\Delta z} \int_{z_{j,1}}^{z_{j,2}} \mathrm{d}z \; G_{1\mathrm{D}}(z - z'). \tag{3.17}$$

For our effectively one-dimensional system of point charges, we can decompose the charge density according to

$$\rho_q(z) = \frac{1}{L_x L_y} \sum_i q_i \; \delta(z - z_i), \tag{3.18}$$

where $\delta(z)$ is the one-dimensional Dirac delta function. Inserting this expression back into our previous result for the potential yields

$$\bar{\Phi}_j = \frac{1}{L_x L_y} \sum_i q_i \; \bar{G}_{1\mathrm{D},j}(z_i). \tag{3.19}$$

Analogously, the averaged field is given by

$$\bar{E}_{z,j} = -\frac{1}{L_x L_y} \sum_i q_i \; \bar{G}'_{1\mathrm{D},j}(z_i). \tag{3.20}$$

The corresponding expressions for $\bar{G}_{1\mathrm{D}}$ and $\bar{G}'_{1\mathrm{D}}$ for Ewald summation are derived in Appendix B.1. The above averages for potential and field depend on all particle positions and therefore implicitly on time. The time average of any quantity X is defined as

$$\langle X \rangle = \frac{1}{\tau} \int_0^\tau \mathrm{d}t \; X(t), \tag{3.21}$$

where τ is the total simulation time of the production run. It is straightforward to evaluate $\langle \bar{\Phi}_j \rangle$ and $\langle \bar{E}_{z,j} \rangle$ for the discrete trajectory obtained from the NEMD simulation.

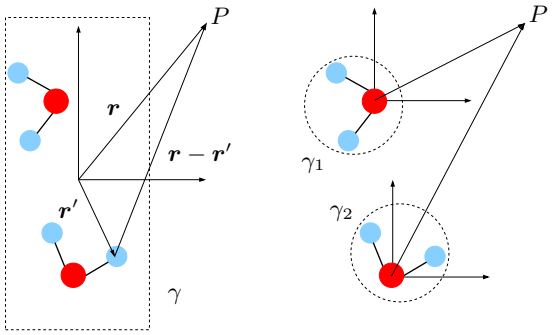

Figure 3.3: Illustration of two different multipole expansions: a) with respect to the centre of the region γ ('slab expansion') and b) for each molecule γ_j individually with the oxygen site at the origin ('molecule expansion'). Both approaches give rise to the same field at a distant point P.

3.4 Multipole expansion

In what follows, we outline how the exact potential, as calculated from the charge density, can be decomposed into individual multipole contributions. This helps us to gain insight into how the alignment of the molecules with respect to the temperature gradient affects the field. We consider two different expansions for comparison which are illustrated in Fig. 3.3. In the slab expansion (Fig. 3.3a), the multipole moments due to the charges located inside a bin are calculated relative to its centre. In the molecule expansion (Fig. 3.3b), separate multipole expansions are carried out for each individual molecule and the multipoles are located at the respective oxygen sites. If all moments were considered in the expansion, both approaches would give rise to the same potential at a distant point P. We note that both types of expansion have already been considered in the past for interfacial systems[96,99]. However, here we use a more general formulation[100] which is also applicable to modified kernels representing truncated Coulomb interactions.

The potential generated by a charge distribution enclosed in a volume γ is given by

$$\Phi(\boldsymbol{r}) = \int_{\gamma} \mathrm{d}^3 r' \; G(\boldsymbol{r} - \boldsymbol{r}') \rho_q(\boldsymbol{r}'). \tag{3.22}$$

From this equation we can obtain the contributions of the individual multipole

moments by expanding $G(\boldsymbol{r}-\boldsymbol{r}')$ into a Taylor series around $\boldsymbol{r}$,

$$\begin{aligned}\Phi(\boldsymbol{r}) \approx \quad & G(\boldsymbol{r}) \underbrace{\int_\gamma \mathrm{d}^3 r' \rho_q(\boldsymbol{r}')}_{q} \\ & - \sum_\alpha \nabla_\alpha G(\boldsymbol{r}) \underbrace{\int_\gamma \mathrm{d}^3 r' r'_\alpha \rho_q(\boldsymbol{r}')}_{\mu_\alpha} \\ & + \sum_{\alpha,\beta} \nabla_\alpha \nabla_\beta G(\boldsymbol{r}) \underbrace{\frac{1}{2} \int_\gamma \mathrm{d}^3 r' r'_\alpha r'_\beta \rho_q(\boldsymbol{r}')}_{Q_{\alpha\beta}},\end{aligned} \tag{3.23}$$

where q is the total charge in γ, $\boldsymbol{\mu}$ the dipole moment and Q the quadrupole moment. The symbol ∇_α denotes the derivative with respect to the Cartesian component r_α. Moving the origin of the charge distribution to $\tilde{\boldsymbol{r}}$ and taking into account the symmetry properties of our effectively one-dimensional system, we find

$$\begin{aligned}L_x L_y \Phi(z) \approx \quad & \underbrace{G_{1\mathrm{D}}(z-\tilde{z})\, q}_{\text{monopole contribution}} - \underbrace{G'_{1\mathrm{D}}(z-\tilde{z})\, \mu_z}_{\text{dipole contribution}} \\ & + \underbrace{G''_{1\mathrm{D}}(z-\tilde{z})\, Q_{zz}}_{\text{quadrupole contribution}} .\end{aligned} \tag{3.24}$$

From the simulated trajectory, we then compute time averages of the multipole densities $\bar{\rho}_{q,j}$, $\bar{\rho}_{\mu,j}$ and $\bar{\rho}_{Q,j}$ for the monopole, dipole and quadrupole moments of every bin j, respectively. Before defining these quantities, we first introduce some additional notation to distinguish between the two types of expansion. We use superscripts $\cdot^{(m)}$, where $m = 1$ for slabs (Fig. 3.3a) and $m = 2$ for molecules (Fig. 3.3b). The density of $X = q, \mu_z, Q_{zz}$ [cf. Eq. (3.23)] is then given by

$$\bar{\rho}^{(1)}_{X,j} = \frac{1}{\Delta v} \times \{\text{moment of bin } j\} \tag{3.25}$$

for the case $m = 1$ and

$$\bar{\rho}^{(2)}_{X,j} = \frac{1}{\Delta v} \times \{\text{sum of molecular moments in bin } j\} \tag{3.26}$$

for the case $m = 2$, where $\Delta v = L_x L_y \Delta z$ is the volume of the bin. Since we only consider the multipole moments q, μ_z and Q_{zz}, from now on we omit the subscripts for readability.

In general, the multipole moments depend on the way the charge distribution is partitioned[101,102] and consequently the multipole densities for slabs and molecules

are not directly comparable. For example, the quadrupole moment of a reference bin will, in general, not be equal to the sum of the molecular quadrupole moments. Furthermore, we make an intentional, small mistake in the evaluation of $\bar{\rho}^{(2)}_{\mu,j}$ and $\bar{\rho}^{(2)}_{Q,j}$ for the sake of computational convenience, because we ignore the precise location of the molecular moments within the bin j. However, as we will see in Sec. 3.6, the error in the electrostatic potential introduced by this approximation is negligible.

The electrostatic potential (at the centre of bin j) is then calculated as the sum of the three contributions in Eq. (3.24),

$$\Phi^{(m)}_j = \Phi^{(m)}_{q,j} + \Phi^{(m)}_{\mu,j} + \Phi^{(m)}_{Q,j}, \tag{3.27}$$

which are given by

$$\Phi^{(m)}_{q,j} = \quad \Delta z \sum_{l=1}^{N_\mathrm{b}} G_\mathrm{1D}(z_j - z_l)\bar{\rho}^{(m)}_{q,l}, \tag{3.28a}$$

$$\Phi^{(m)}_{\mu,j} = -\Delta z \sum_{l=1}^{N_\mathrm{b}} G'_\mathrm{1D}(z_j - z_l)\bar{\rho}^{(m)}_{\mu,l}, \tag{3.28b}$$

$$\Phi^{(m)}_{Q,j} = \quad \Delta z \sum_{l=1}^{N_\mathrm{b}} G''_\mathrm{1D}(z_j - z_l)\bar{\rho}^{(m)}_{Q,l}, \tag{3.28c}$$

respectively. Since the molecules are charge-neutral, it follows that all values $\rho^{(2)}_{q,j}$ and consequently $\Phi^{(2)}_{q,j}$ vanish identically.

3.5 Simulation protocol

For production runs, we prepared the system in the same state as Armstrong and Bresme[28] in order to carry out a quantitative comparison. The simulation box (Fig. 3.2) has exactly the same dimensions as the one used for the model system. For two of the three NEMD simulations we used the Wolf method and the remaining one was performed with Ewald summation (the relevant parameters are summarised in Sec. 3.2.3). LJ interactions were truncated at 11 Å in all cases. The box contains $N = 4500$ SPC/E molecules resulting in a mass density of $\rho_m = 0.934$ g/cm^3. All simulations were carried out using a modified version of the software package LAMMPS (9Dec14)[54] which we augmented with the eHEX/a algorithm[39].

3.5.1 Equilibration

The system was first equilibrated and validated. Starting from an initial lattice structure with zero linear momentum, we integrated the equations of motion with the velocity Verlet algorithm[103] employing a timestep of $\Delta t = 1$ fs. For the first 20 ps we rescaled the velocities to drive the system close to the target temperature of 400 K. This was followed by a short 200 ps NpT run using a Nosé–Hoover thermostat with a relaxation time of $\tau_T = 1$ ps and a Nosé–Hoover barostat with a relaxation time of $\tau_p = 2.5$ ps[56,57]. We then rescaled the box to the target dimensions and carried out a 500 ps NVT run during which we monitored the average system energy. Next, we adjusted the kinetic energy of the last configuration by velocity rescaling and used it as input for another 1 ns NVE equilibration run. The average temperature during this run was $T = (400 \pm 0.1)$ K, where the error bar was estimated using block average analysis[7]. We computed the pair-correlation function, the velocity autocorrelation function, the dielectric constant and the distance-dependent Kirkwood g-factor (see Appendix B.3). The validation suggests that our implementation is correct and our choice of parameters reasonable.

3.5.2 Non-equilibrium stationary state

To investigate the effect of a thermal gradient after the equilibration, the system was driven to a non-equilibrium stationary state by imposing a constant heat flux between two reservoirs, Γ_1 and Γ_2 (Fig. 3.2). The equations were solved numerically using the eHEX/a algorithm developed in the previous chapter with a timestep of $\Delta t = 2$ fs. After switching on the thermostat, we waited for 10 ns for any transient behaviour to disappear before starting with the $\tau = 60$ ns run. The energy conservation was excellent ($|\Delta E/E| \approx 0.005\%$) and the centre of mass velocity of the simulation box remained close to machine precision throughout the simulation. The heat fluxes are input parameters of the eHEX algorithm which were adjusted by trial and error. The employed values are summarised in Tab. 3.1.

We note that lower heat fluxes are required for the Wolf method in order to achieve the same temperature gradient as for Ewald summation. This is consistent with the observation that the truncation of electrostatic interactions results in lower thermal conductivities[87].

Table 3.1: Imposed heat fluxes and measured values for the tempature gradients. We note that our heat flux for the Wolf ($\zeta L = 7.2$) run is about 1.7% larger than the value used by Armstrong and Bresme[28].

	$J_{Q,z}$ (10^{10} W/m^2)	∇T (K/Å)
Ewald	4.243	-5.14 ± 0.04
Wolf ($\zeta L = 1.0$)	4.166	-5.17 ± 0.04
Wolf ($\zeta L = 7.2$)	3.875	-5.18 ± 0.04

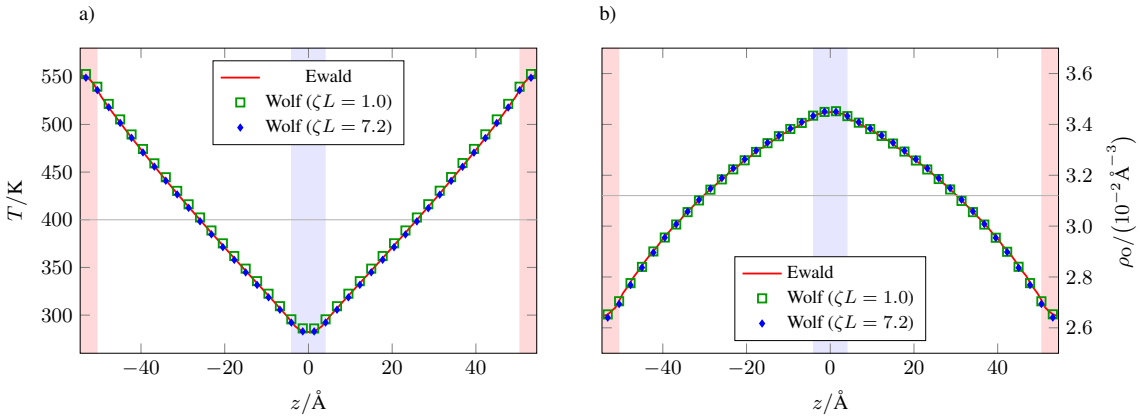

Figure 3.4: Spatial variation of a) temperature and b) oxygen number density obtained with Ewald summation and the Wolf method. The horizontal lines indicate the spatial and temporal equilibrium averages of the temperature and the number density, respectively. The vertical stripes indicate the locations of the hot (coloured in red) and cold (coloured in blue) reservoirs.

3.6 Results

In this section, we present the key results for the temperature and density profiles (Sec. 3.6.1), the multipole expansions (Sec. 3.6.2), the potential (Sec. 3.6.3), the field (Sec. 3.6.4) and the polarisation (Sec. 3.6.5). We estimated error bars for all results in this section. To this end we divided the entire trajectory into 600 blocks (of length 100 ps) and assumed the results for the individual blocks to be uncorrelated. The size of the individual error bar then corresponds to twice the standard deviation of the mean. This estimate comprises the statistical error as well as the methodological error arising, for example, from the employed quadrature.

3.6.1 Temperature and density

Figures 3.4a-b show the spatial variations in temperature and density along the z-direction with a resolution of $\Delta z = 2.73$ Å ($N_\mathrm{b} = 40$). The temperature of an individual bin was calculated from the non-translational kinetic energy of the atoms

inside that bin[39]. There are only small differences between the results obtained with the Ewald and Wolf methods. The peak temperature at the centre of the hot reservoir is about 552 K and the lowest temperature at the centre of the cold reservoir is about 285 K (Fig. 3.4a). The temperature profile is linear outside the reservoirs and symmetric with respect to the origin of the simulation box, which is in accordance with the setup.

The measured average number densities (Fig. 3.4b) obtained with Ewald summation and the Wolf method agree well apart from slight differences in the vicinity of the cold reservoir. The mass density varies by up to 15% (cold reservoir) with respect to ρ_m. We note that on this scale, we did not observe any appreciable discontinuities of the temperature or density close to the reservoir boundaries, although the thermostatting force is discontinuous.

3.6.2 Molecular orientation and multipole moments

In this section, we discuss the induced molecular alignment and multipole moments due to the thermal gradient for both expansions in Fig. 3.3. The left column in Fig. 3.5 corresponds to the slab (centre-of-bin) expansion and the right column to the molecule expansion. The monopole in the molecule expansion vanishes identically, hence it is not shown. The spatial variations of all quantities are shown with a resolution of $\Delta z = 5.45$ Å ($N_\mathrm{b} = 20$).

Let us consider the time averaged charge density for slabs first (Fig. 3.5a). For Ewald summation the error of the average is so large that it swamps the signal even after 60 ns of simulation time. We also note that the curve is not symmetric in the vicinity of the cold reservoir within the statistical uncertainty shown in the plot. We believe that this may be due to the fact that we computed the error bars as if neighbouring bins were independent, which is not the case, because molecules are charge neutral. The real error bars may be larger due to long-wavelength fluctuations. We confirmed that the results become symmetric (within the statistical error) upon doubling the simulation time.

For the Wolf method there is an accumulation of positive charge in the vicinity of the hot reservoir, which is enhanced by stronger damping. This result agrees qualitatively with the findings of Rodgers and Weeks for a different inhomogeneous system, where the authors compared the (Gaussian-smoothed) charge density obtained with Gaussian-truncated (GT) water to that of Ewald summation[83]. Furthermore, we note that the error bar increases by about one order of magnitude upon refining the resolution by a factor of 10, which corresponds to $\Delta z \approx 0.54$ Å ($N_\mathrm{b} = 200$) used by Armstrong and Bresme[28].

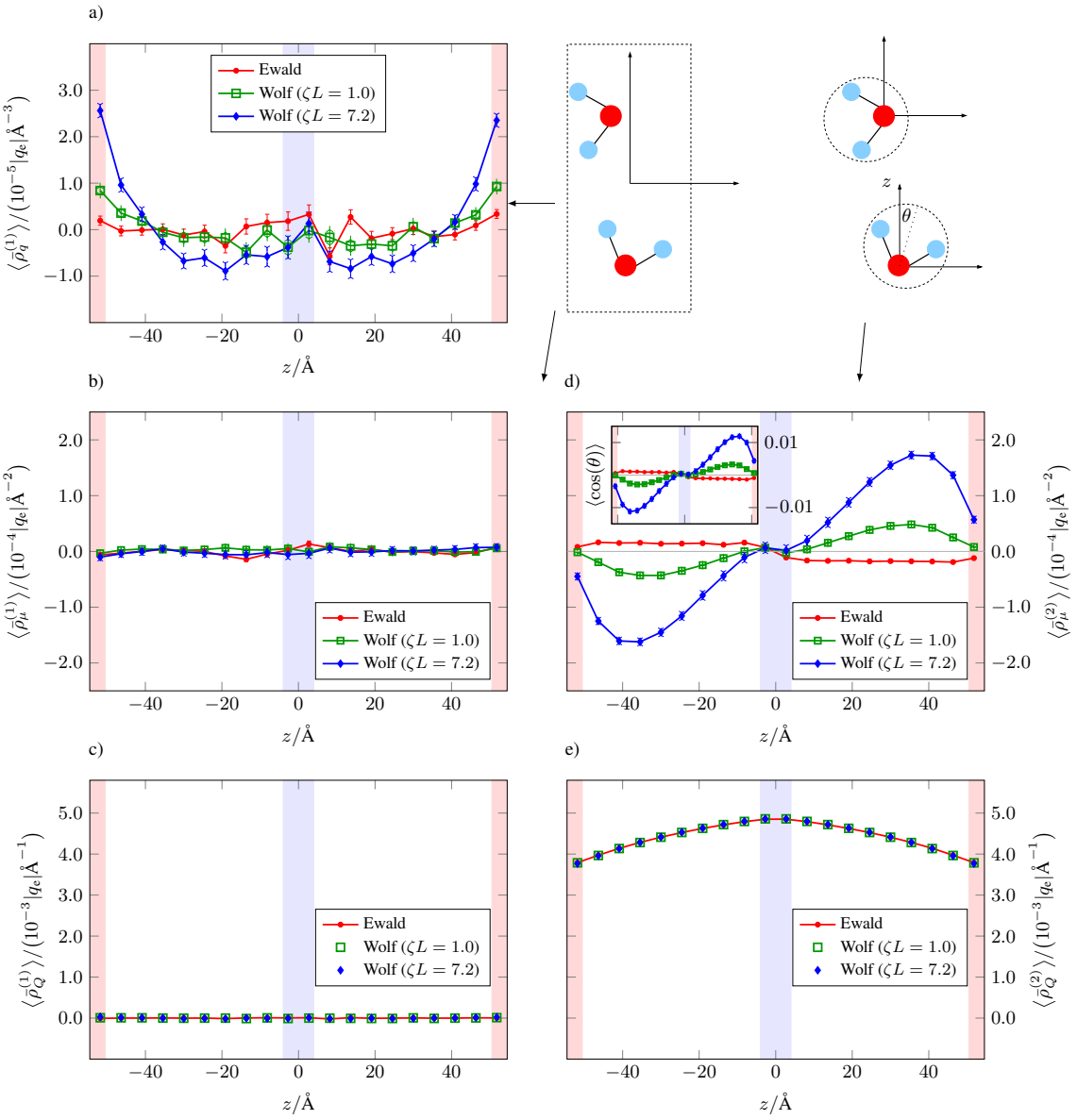

Figure 3.5: Multipole densities for the slab expansion (left column) and molecule expansion (right column). The panels a-c) show the charge density, dipole density and quadrupole density, respectively, for the slab expansion. The panels d) and e) show the dipole density and quadrupole density, respectively, for the molecule expansion. The inset in panel d) shows the average molecular alignment with the temperature gradient. Horizontal lines in the inset and the full figure were added to highlight the symmetry of the result.

Figures 3.5b and d show the dipole densities for both expansions, respectively. For the slabs (Fig. 3.5b), there is no noticable trend of the dipole density within the statistical uncertainity. However, for the molecule expansion (Fig. 3.5d) we find a strong disagreement between the two electrostatic kernels. For this case, we also quantified the average molecular alignment using the order parameter[31]

$$\cos(\theta) = \boldsymbol{n} \cdot \boldsymbol{e}_z, \tag{3.29}$$

where $\boldsymbol{n} = \boldsymbol{\mu}/\mu$ defines the orientation of a molecule and $\boldsymbol{e}_z$ is the unit vector in the direction of the temperature gradient. In the case of Ewald summation molecules, on average, point to the cold reservoir and the alignment is fairly constant outside the reservoirs (see inset in Fig. 3.5d). The Wolf method entirely fails to capture this behaviour. For the wide range of parameters considered here (including the ones previously employed in the literature), the method predicts opposite orientations and overestimates the magnitude of alignment by a factor of about 7 for the strong damping. Employing a lower value for the damping parameter reduces the overestimation, but cannot correct the wrong sign. We also note that our results for the average molecular orientation (inset in Fig. 3.5d) are in agreement with the ones reported by Armstrong and Bresme[28].

The quadrupole densities, shown in Figs 3.5c and e, agree well with each other within each expansion. Similarily to the dipole density, considering slabs for the expansion (Fig. 3.5c) yields results which are negligible compared to the molecule expansion (Fig. 3.5e). We note that in the latter case, the profile is proportional to the oxygen number density (Fig. 3.4b) and can lead to considerable contributions to the potential.

Repeating our simulation with Ewald summation and vacuum boundary conditions (see Refs 97 and 91 for more details), we found consistent results for the multipole densities (not shown). We can therefore rule out any artefacts arising from the boundary conditions at infinity on the results shown in this section. However, we noticed that the statistical error of the molecular dipole density decays much faster for vacuum boundary conditions relative to tin-foil boundary conditions.

3.6.3 Electrostatic potential

In the previous section, we analysed the thermally induced multipole moments for two different multipole expansions, namely slabs and molecules. The aim of this section is to compare three different ways of calculating the electrostatic potential: Firstly, we consider the exact analytical average given by Eq. (3.19). Secondly, we approximate

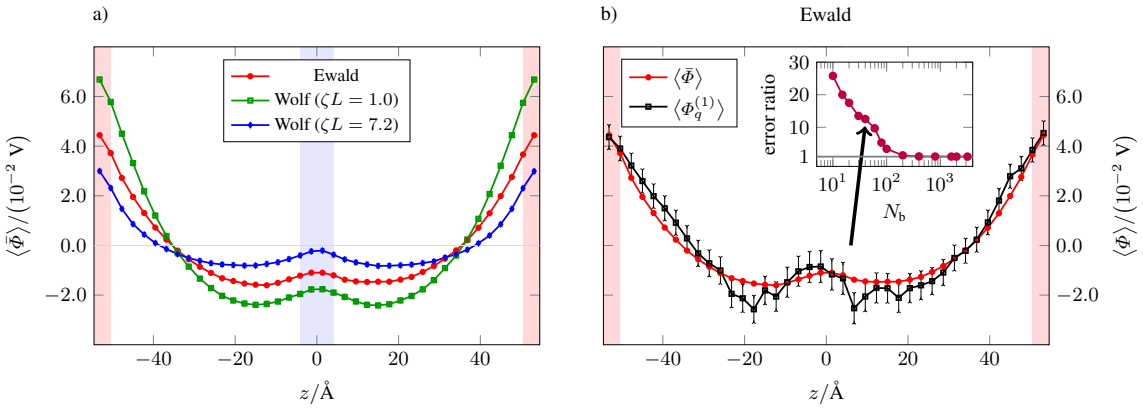

Figure 3.6: The exact potential is shown in panel a) and a comparison between the potential calculated solely from the monopole density in the slab expansion and the exact result calculated with Ewald summation is shown in b). The inset compares the ratio of the maximum errors which were calculated from 600 blocks of length 100 ps as a function of the number of bins. The arrow indicates the error ratio for the resolution shown in the full figure.

the potential using only the average charge density given by the slab expansion, Eq. (3.28a), which is the approach regularly employed in the literature [28,93–95]. Thirdly, we approximate the potential using also the dipole and quadrupole densities, i.e. Eqs (3.28b-c).

Let us consider the results for the exact calculation first, which are shown in Fig. 3.6a. All graphs are symmetric with respect to the origin of the simulation box and periodic, indicating that the field vanishes at the centres of the reservoirs. Although the shape of the potential predicted by the short-ranged method is similar to the one for Ewald summation, the results are sensitive to the choice of damping parameter. Weak damping overestimates the potential, whereas strong damping leads to an underestimation. Both our choices fail to reproduce the Ewald summation result correctly, although it seems plausible that intermediate values for the damping parameter could lead to a better agreement.

Figure 3.6b compares (for Ewald summation) the exact result for the electrostatic potential to that given by the monopole density in the slab expansion. We recall that the latter approach corresponds to averaging the charge density first and integrating it with the appropriate kernel afterwards [Eq. (3.28)a]. It is clear from comparison of the two curves including error bars that the exact calculation yields a huge improvement over the approximation. For the resolution shown in the plot ($N_\mathrm{b} = 40$, $\Delta z = 2.73$ Å), the error bars are reduced by more than one order of magnitude. The inset shows the ratio of the maximum error of the approximation to the maximum error of the exact calculation as a function of the number of bins. (We define the maximum error to be half the length of the largest error bar throughout the entire

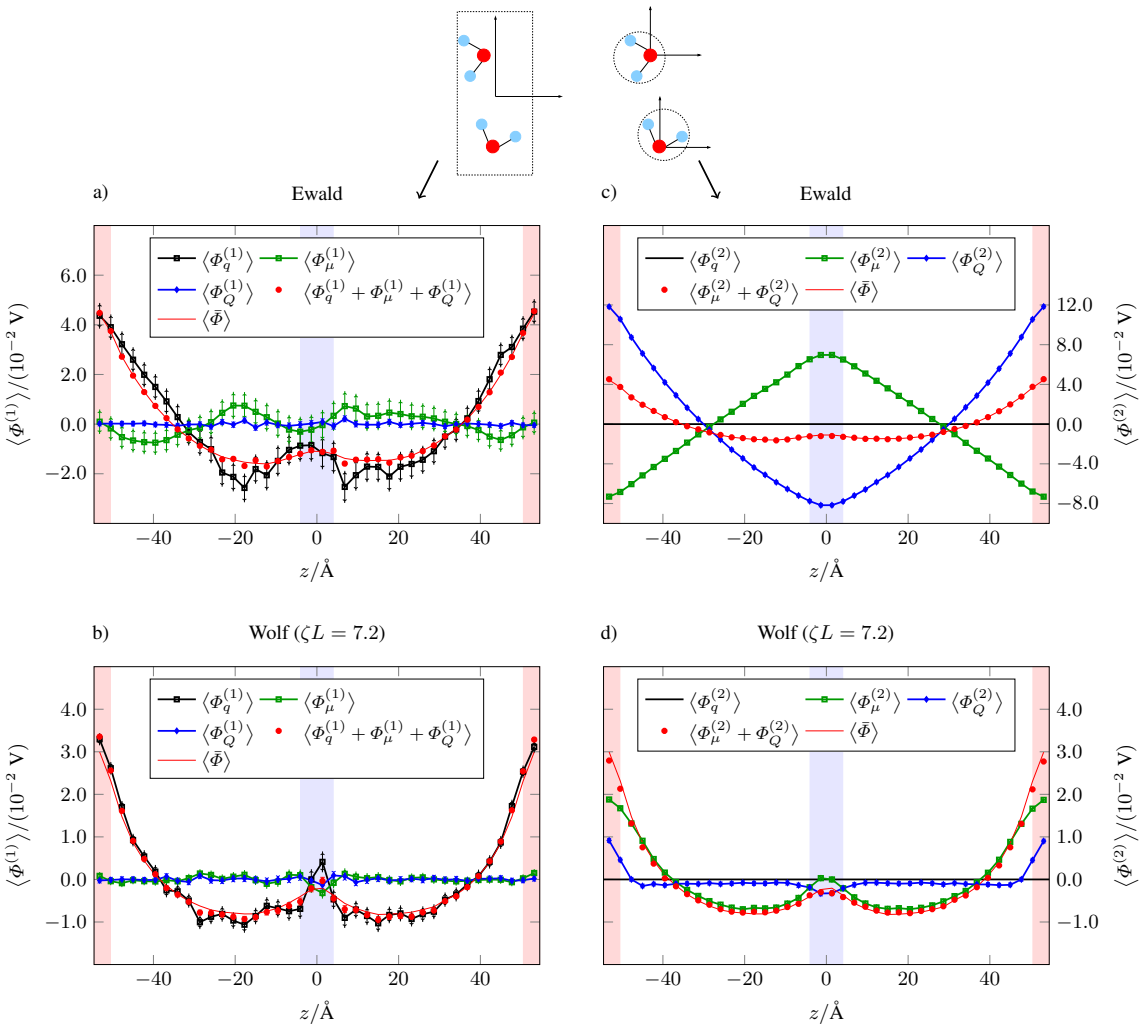

Figure 3.7: Individual contributions to the potential for the slab expansion (left column) and molecule expansion (right column). The results for Ewald summation are shown in panels a) and c) in the first row and for the Wolf method in panels b) and d) in the second row.

interval.) For a very low resolution of 10 grid points ($\Delta z = 10.9$ Å), the maximum error decreases by about a factor of 26. For high resolutions of $\Delta z \leq 0.5$ Å the error ratio approaches unity implying that both methods become comparable, which is the expected behaviour in the limit $\Delta z \to 0$. At the same time the magnitude of the error naturally increases for higher resolutions because fewer molecules contribute to a particular bin (for 400 bins the maximum error increases by about 50% compared to the resolution of 40 bins shown in the figure).

Given that molecules point, on average, in opposite directions for the two electrostatic kernels (Fig. 3.5d), it is counterintuitive that the potentials are qualitatively comparable. To understand the origin of this seeming contradiction, we singled out the individual multipole contributions, which are illustrated in Figs 3.7a-d for

both expansions. Let us consider the slab expansion first. For both electrostatic kernels (Figs 3.7a-b) we found the monopole contribution (black curve) to capture the exact potential (red line) reasonably well for the chosen spatial resolution ($N_\mathrm{b} = 40$, $\Delta z = 2.73$ Å). However, if we consider a point dipole and a point quadrupole (representative for the respective bin average) in addition to the point monopole located at the centre of each bin, we obtain a much better approximation to the exact result (red circles). In fact, for Ewald summation we recover the exact potential almost perfectly, whereas we observe an overshoot inside the hot reservoir for the Wolf method. We believe that a more accurate approximation for the short-ranged method might be obtained by considering octupole and hexadecapole contributions in addition, but we did not investigate this further.

The situation changes entirely for the molecule expansion shown in Figs 3.7c-d, where the monopole contribution is zero. For Ewald summation (Fig. 3.7c), the dipole density leads to a linear potential outside the reservoirs (green curve) corresponding to a negative field in the left half of the simulation box. However, close to the hot reservoir the quadrupole contribution (blue curve) outweighs the dipole contribution causing the slope of the overall potential to be negative and therefore the field to be positive. In the vicinity of the cold reservoir the dipole contribution dominates over the quadrupole contribution and the field is negative. The sum of both terms (red circles) agrees perfectly with the exact average (red line). For the Wolf method we found that the quadrupole density constitutes a much smaller correction to the dipole contribution which is almost negligible outside the reservoirs. This might seem surprising at first given that the results for the quadrupole densities agree well for both summation methods (Fig. 3.5e). The apparent contradiction is explained by the fact that the derivatives of the kernels in the evaluation of the potential are very different for both methods. We will get back to this point in Sec. 3.6.5 when we discuss the macroscopic polarisation.

With regard to the accuracy of the full multipole approximations (up to the quadrupole term), we observed different trends for the maximum error of the potential within each expansion. For the slab expansion we found the maximum error to be about 6 times larger than the error of the exact potential for the lowest resolution ($N_\mathrm{b} = 10$, $\Delta z = 10.9$ Å). Upon increasing the resolution, the error ratio approaches unity, which is the expected behaviour. However, this is not the case for the molecule expansion, where the error is only about 20% larger than the error of the exact potential initially, but the difference increases to about 100% for the highest resolution ($N_\mathrm{b} = 3200$, $\Delta z = 0.034$ Å). We believe that this behaviour is reasonable, because we never intersect molecules and cannot resolve the potential inside a molecule correctly.

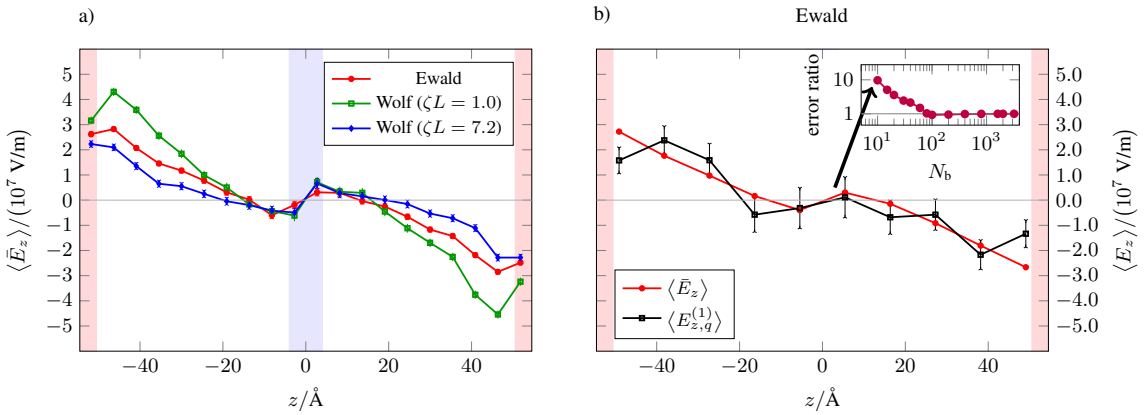

Figure 3.8: The exact field is shown in figure a) and a comparison between the field calculated from the monopole density in the slab expansion and the exact result is shown in b). The inset compares the ratio of the maximum errors which were calculated from 600 blocks of length 100 ps as a function of the number of bins. The arrow indicates the error ratio for the resolution shown in the full figure.

The higher the resolution the worse we expect the approximation to become in the vicinity of the point multipoles. Averaging the potential exactly is preferable on all scales, rendering it clearly the method of choice.

3.6.4 Electrostatic field

The exact results for the field in the sense of Eq. (3.20) are shown in Fig. 3.8a. Focusing on the left half of the simulation box, we notice that the field is positive and strongest in the vicinity of the hot reservoir. For the peak field strength we measured values of about 2.8×10^7 V/m, 4.4×10^7 V/m and 2.2×10^7 V/m for Ewald summation and the Wolf method with weak and strong damping, respectively. Close to the hot reservoir, the short-ranged method overshoots the Ewald summation result for low damping and vice versa for high damping. We also infer from the figure that the field changes its sign in the vicinity of the cold reservoir. From the discussion of the potentials in the previous section (Fig. 3.7c) we know that the inversion happens exactly when the dipole contribution to the field dominates over the quadrupole contribution.

Comparing our results to the ones reported by Bresme and co-workers, we find a major discrepancy: In the original work[28] the reported fields are about one order of magnitude higher than what we found. Recently, however, it was suggested that the thermally induced field in a spherical droplet of SPC/E water is of the order of 10^7 V/m after comparison with Ewald summation (PPPM)[68]. Nevertheless, the discrepancy still persists as the authors[68] suggest that the Wolf method itself is responsible for the overestimated field, whereas, in fact, the opposite is true for the

set of parameters employed in Ref. 28. The Wolf method slightly underestimates the field if it is calculated consistently, namely using the correct kernel (see Fig. 3.8a). We can reproduce the results of Armstrong and Bresme closely if we calculate the field as[28]

$$E_z(z) = 4\pi \int_{-L_z/2}^{z} \mathrm{d}z' \rho_q(z'), \tag{3.30}$$

considering Gaussian units and taking the lower integration bound to be $-L_z/2$ rather than $-\infty$. (A comparison is omitted for brevity.) For Ewald summation this expression is correct and equivalent to Eq. (3.15) with $G'_{\mathrm{1D,E}}$ as long as the net dipole density of the box,

$$\bar{\rho}_{\mu,L_z} = \frac{1}{L_z} \int_{-L_z/2}^{L_z/2} \mathrm{d}z' z' \rho_q(z'), \tag{3.31}$$

vanishes. Considering sufficiently long simulations, this is necessarily the case for our system because of the symmetric setup (see Figs 3.2, 3.5b and d). If this was not the case, an additional term $4\pi\bar{\rho}_{\mu,L_z}$ would have to be added to the right-hand side of Eq. (3.30). The equivalence is trivially shown by rewriting the integral in Eq. (3.15) taking into account periodicity and charge neutrality. Alternatively, one can integrate Poisson's equation directly and impose periodicity by choosing the integration constants accordingly[104]. However, applying Eq. (3.30) for the Wolf method is wrong and the discrepancy between our result and the one of Armstrong and Bresme[28] can therefore be traced back to using the incorrect expression in the calculation.

Similarly to what we observed for the potential, considering exact averages rather than estimating the field from the average charge density yields a huge improvement for low resolutions. The comparison in Fig. 3.8b is carried out for a resolution of $N_\mathrm{b} = 10$ ($\Delta z = 10.9$ Å) and, as shown in the inset, the error of the approximative field, i.e. using the negative derivative of $G_{\mathrm{1D,E}}$ in Eq. (3.28a), is about 10 times larger than the exact one. For resolutions higher than $N_\mathrm{b} = 80$ bins ($\Delta z \leq 1.36$ Å), both approaches yield similar errors. Comparing the insets of Figs 3.6b and 3.8b, we notice that the enhancement of the exact method over the approximative one is much higher for the potential. This can be partly explained by looking at the functional form of $G'_{\mathrm{1D,E}}$ (Eq. (B.9a) in Appendix B.1). The function is piecewise linear and the midpoint rule, which corresponds to multiplying the function value at the centre of the bin by Δz, is exact in the absence of any discontinuity. Therefore, the advantage of using $\bar{G}'_{\mathrm{1D,E}}$ over $G'_{\mathrm{1D,E}}$ for the evaluation of the field is less significant than for the potential.

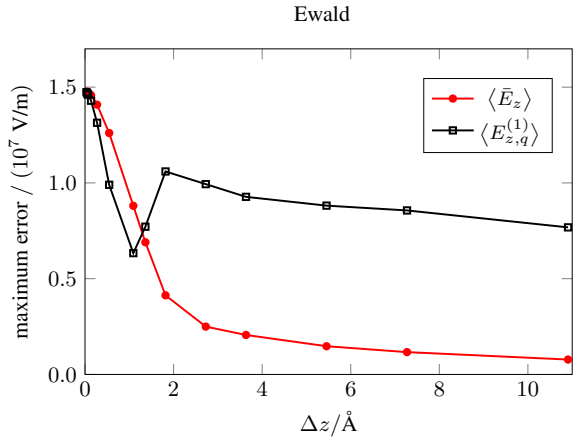

Figure 3.9: Spatial maximum error as a function of the resolution Δz for the exact field (red circles) and the monopole field (black, open squares), respectively. (The error is defined as one standard deviation of the mean and the error bar in Fig. 3.8b corresponds to twice the value for $\Delta z = 10.9$ Å.)

Figure 3.9 compares the spatial maximum errors for varying resolutions. Interestingly, for sufficiently high resolutions of $\Delta z \leq 1$ Å we found the maximum error of the approximative method to be up to almost 30% lower than the one for the exact average. We attribute this to cancellation of errors, since convergence tests support a correct implementation. Far more important is the magnitude of the error for high resolutions. For simulation time scales of 100 ns the error is comparable to the signal itself requiring even longer runs for the statistics to be satisfactory. Suppose we wanted to get a rough idea of what the field looked like. With the conventional method, i.e. averaging the charge density first and then integrating it, the best we can do is to calculate the results on a sufficiently high resolution and then perform some sort of averaging. On the one hand, this approach is problematic because the coarse-grained values do not represent the correct bin averages. On the other hand, it is not straightforward to propagate the statistical errors from the fine resolution to the coarse one since the values are highly correlated. Our proposed method of averaging the potential and the field analytically eliminates both issues and yields a huge improvement for low resolutions reducing the required simulation time scales by up to two orders of magnitude for the same quality of statistics.

3.6.5 Macroscopic polarisation

Our final goal in this section is to relate the molecular multipole densities to the macroscopic polarisation. We show that the macroscopic Maxwell equation

$$\bar{E}_z(z) = \bar{D}_z(z) - 4\pi \bar{P}_z(z) \tag{3.32}$$

holds locally for the bin averages calculated with Ewald summation, where $\bar{P}_z$ and $\bar{D}_z$ are the z-components of polarisation and displacement field, respectively. We do not make any a priori assumptions about the locality[105] and use the multipole expansions developed in Sec. 3.4 as a general starting point for the discussion. We then identify the quantities on the right-hand side of Eq. (3.32) after simplifying the expressions. We note that our analysis only holds in the context of sufficiently long simulations (like in Sec. 3.4), because we use $\rho_q(z)$ in place of the full $\rho_q(\boldsymbol{r})$. This simplifies the discussion in that we only need to consider the z-component of the spatially averaged dipole density, $\bar{\rho}_\mu$, and the density of Q_{zz} given by $\bar{\rho}_Q$, respectively.

The water molecules comprise the polarisable background medium and there are no free charges. From our discusion in Sec. 3.6.3, we know that the dipole contribution alone yields a poor approximation to the potential (Figs 3.7c and d). As a natural extension we considered the quadrupole contribution[106], which was also found to be important in simulation studies of interfacial electric fields[96,99,107]. With the inclusion of this contribution, the potentials from the molecular multipole expansions match the exact potentials very well for both methods, respectively. The corresponding expression for the field extends to

$$\bar{E}_z(z) = \int_{-\frac{L_z}{2}}^{\frac{L_z}{2}} \mathrm{d}z' \, \left[G''_{1\mathrm{D}}(z-z')\bar{\rho}_\mu(z') - G'''_{1\mathrm{D}}(z-z')\bar{\rho}_Q(z') \right] \tag{3.33a}$$

$$= \int_{-\frac{L_z}{2}}^{\frac{L_z}{2}} \mathrm{d}z' \, G''_{1\mathrm{D}}(z-z') \left[\bar{\rho}_\mu(z') - \bar{\rho}'_Q(z') \right], \tag{3.33b}$$

where the derivatives of the kernels are given in Appendix B.1. To get to Eq. (3.33b) we integrated the second term in Eq. (3.33a) by parts taking into account the periodicity. We can solve the above integral analytically for Ewald summation and find that

$$\bar{E}_z(z) = -4\pi \left[\bar{\rho}_\mu(z) - \bar{\rho}_{\mu,L_z} - \bar{\rho}'_Q(z) \right], \tag{3.34}$$

where $\bar{\rho}_{\mu,L_z}$ is the box average of $\bar{\rho}_\mu(z)$. In general, we can identify this contribution with $\bar{D}_z$ as it corresponds to the (constant) field arising from an induced surface charge density at infinity (tin-foil boundary conditions). We refer to Refs 108 and 109 for a more general discussion. Although the instantaneous value of $\bar{D}_z$ may fluctuate, we know that its time average vanishes, because our system does not exhibit a net dipole moment (Figs 3.5b and d). For Ewald summation the definition

of polarisation as

$$\bar{P}_z(z) = \bar{\rho}_\mu(z) - \bar{\rho}_Q^{'}(z) \tag{3.35}$$

therefore naturally leads to the correct proportionality of $\langle \bar{P}_z(z) \rangle = -\langle \bar{E}_z(z) \rangle / 4\pi$. For the Wolf method the relation between electric field and polarisation (as defined above) is more complicated, because we cannot solve the integral in Eq. (3.33b) analytically. More importantly, we cannot expect the short-ranged method to predict fields accurately in general, because its kernel is not a solution of Poisson's equation. The estimates for the thermally induced fields might be reasonable, but it is trivial to come up with an example, such as a plate capacitor, for which the method would fail.

Finally, we would like to discuss the macroscopic Maxwell equation (3.32) in the context of the slab expansion. As shown in Figs 3.7a-b, we can identify all relevant multipole contributions to the potential and recover a good approximation to the exact solution implying overall consistency. Due to the nature of the spatial averaging, we obtain a non-vanishing charge density (Fig. 3.5a) for our inhomogeneous system. This is inconsistent, however, with the derivation of Eq. (3.32), where charges within a molecule are summed first in order to get from the microscopic to the macroscopic description[101,106] and the charge density vanishes identically. Identification of displacement field and polarisation is therefore not meaningful for the slab expansion. This problem is avoided altogether in the molecule expansion, which is consistent with Eq. (3.32), and we can unambiguously identify all terms in the macroscopic Maxwell equation.

3.7 Conclusions

In this chapter, we have analysed the electric fields and multipole moments induced by a strong thermal gradient in NEMD simulations of water in a setup which was previously studied by Armstrong and Bresme[28]. Our comparison comprises results for two different treatments of Coulomb interactions, namely Ewald summation and the short-ranged Wolf method. The latter was employed in most of the previous studies on the thermo-polarisation effect[26,28,32,64,68]. We identified two key differences to the literature data: Firstly, the Wolf method fails to reproduce the dipole density correctly for parameters that work well in equilibrium simulations. The molecules point, on average, in opposite directions compared to Ewald summation and the alignment is strongly enhanced.

Secondly, for both methods the peak field strength is of the order of 10^7 V/m. However, for the Wolf method the result depends sensitively on the employed

parameters. For low damping the Wolf method slightly overestimates the field obtained with Ewald summation and vice versa for high damping. The results are therefore in direct constrast to very recent findings of Bresme and co-workers[68] who reported that the Wolf method overestimates the field by an order of magnitude. In fact, we argue that the employed formula for the calculation of the field is incorrect. Taking such truncation into account correctly results in comparable results for the electric field.

Another key result of this chapter are the highly improved spatial averages of the potential and the field for low resolutions. We propose to integrate these quantities analytically over the bins rather than calculating them from the time-averaged charge density, as is usually done in the literature. Potentials and fields then truly represent the exact spatial averages over the microscopic or macroscopic control volumes. We showed that this procedure is straightforward for both summation methods and requires no computational overhead. Comparing the ratio of maximum errors, we found a more than 20-fold reduction of the error for the potential and a 10-fold reduction for the field at the coarsest resolution of $\Delta z \approx 10.9$ Å. Consequently, employing the new method can reduce the simulation time scales by up to two orders of magnitude for the same quality of statistics. The advantage of calculating analytical averages becomes less significant with increasing spatial resolution and both methods are comparable for resolutions of $\Delta z \leq 1$ Å. However, in this case the magnitude of the statistical error is comparable to the signal itself rendering the results meaningless.

In addition, we found that accurate estimates of the potential and the field can be obtained by approximating the water molecules as ideal point dipoles and quadrupoles. For low spatial resolutions we found this approach to yield considerably better results than the calculation from the averaged charge density. Our detailed comparison of the results for the slab and molecule expansions illustrates that the ratio of the individual contributions depends on the control volume we choose for the expansion. For slabs almost all the information can be recovered by considering the monopole, as is usually done in the literature. However, in the molecule expansion the dipole and the quadrupole contributions are significant and both have to be considered in order to recover results from the exact calculation accurately.

Finally, taking into account the quadrupole contribution leads to the expected proportionality between the polarisation and the macroscopic Maxwell field in accordance with the macroscopic Maxwell equations. The Wolf method fails to satisfy this relation entirely. Based on its shortcomings, we therefore conclude that the method is not suitable for reproducing the electrostatic key quantities in

inhomogeneous systems reliably. This is in agreement with the findings of Takahashi and co-workers[89], who reported poor predictions for the electrostatic potential and dipolar orientations in simulations of the liquid–vapour interface, even for cutoff radii almost six times larger than the maximum value considered here.

4

Thermally induced monopoles

Preface

This chapter is based on the publication 'Numerical evidence for thermally induced monopoles' by P. Wirnsberger, D. Fijan, R. A. Lightwood, A. Šarić, C. Dellago and D. Frenkel, which was published in the *Proceedings of the National Academy of Sciences USA* (2017)[37]. A free version of the article is available for download on the arXiv (https://arxiv.org/abs/1610.06840).

The author contributions are as follows: I implemented the software, performed the simulations, analysed the data and wrote an initial draft of the manuscript. C. Dellago, D. Frenkel and I designed the research; D. Fijan, R. A. Lightwood and A. Šarić assisted in performing the research; A. Šarić, C. Dellago, D. Frenkel and I wrote the final version of the paper.

4.1 Hypothesis

The existence of quasi-monopoles in a system of heated or cooled colloidal particles in a polar or paramagnetic fluid follows directly from non-equilibrium thermodynamics, combined with the equations of electro/magneto-statics[38]. Although suggested theoretically, they have thus far not been studied experimentally. In this chapter, we provide numerical evidence indicating that the predicted effects are real and robust. In what follows, we consider the case of thermally induced quasi-monopoles in a dipolar liquid, but all our results also apply to paramagnetic liquids. It has been shown that a thermal gradient will create an electric field in a liquid of dipolar molecules with sufficiently low symmetry[26,31]. In the absence of any external electric field, a heated or cooled colloidal particle placed in such a liquid, will generate an

electric field according to the phenomenological relation [26,30,35]

$$\boldsymbol{E}_{\mathrm{TP}}(\boldsymbol{r}) = S_{\mathrm{TP}} \nabla T(\boldsymbol{r}), \tag{4.1}$$

where $T(\boldsymbol{r})$ is the temperature and S_{TP} the thermo-polarisation coefficient, with a magnitude that is not known *a priori*. For water near room temperature, S_{TP} has been estimated to be $S_{\mathrm{TP}} \approx 0.1$ mV/K [35,36].

Let us next consider the electric polarisation around a heated (or cooled) colloidal particle, for brevity also referred to simply as colloid. We note that the sole function of the colloid is to generate a temperature gradient field in the solvent, which in turn couples to the electric field via Eq. (4.1). Other heat sources (sinks) would lead to the same effect. In steady state the temperature profile at a distance r from the centre of an isolated, spherical colloid of radius R satisfies

$$T(r) = T_\infty + (T_R - T_\infty)\frac{R}{r}, \tag{4.2}$$

and hence

$$\boldsymbol{E}_{\mathrm{TP}}(\boldsymbol{r}) = -S_{\mathrm{TP}}(T_R - T_\infty)\frac{R}{r^2}\hat{\boldsymbol{r}}, \tag{4.3}$$

where T_∞ is the temperature in the bulk liquid and $\hat{\boldsymbol{r}}$ the radially outward pointing unit vector. We note that E_{TP} decays as $1/r^2$. Using Gauss's theorem, we can then write

$$\oiint \boldsymbol{E}_{\mathrm{TP}}(\boldsymbol{r}) \cdot \mathrm{d}\boldsymbol{S} = -4\pi S_{\mathrm{TP}}(T_R - T_\infty)R \equiv \frac{q_{\mathrm{TP}}}{\epsilon_0}, \tag{4.4}$$

where ϵ_0 is the dielectric permittivity of vacuum. In words: the flux through a closed surface around a neutral colloid is non-zero, and is equal to the flux due to an apparent charge $q_{\mathrm{TP}} = -4\pi\epsilon_0 S_{\mathrm{TP}}(T_R - T_\infty)R$. This effective charge is proportional to the radius of the particle, hence larger colloids will have a larger apparent charge.

4.2 Simulation strategy

To verify the existence of thermally induced charges numerically, we performed NEMD and equilibrium MD simulations of a heated and a cooled colloid immersed into a modified ('off-centre') Stockmayer fluid [110]. The modification is such that the LJ centre is displaced from the dipole by $\Delta\boldsymbol{r} = \alpha\hat{\boldsymbol{\mu}}$, where $\alpha = -\sigma/4$ controls the asymmetry and $\hat{\boldsymbol{\mu}}$ is the unit vector of the dipole moment $\boldsymbol{\mu}$. This modification leads to additional torque contributions which are summarised in Appendix C.2. A non-zero value for α is necessary for molecules to undergo thermo-molecular orientation (see Appendix C.5), in accordance with simulation studies on dumbbell

molecules which identified shape or mass asymmetry as a requirement for this effect[31]. An important property of our model fluid is that S_{TP} is effectively constant in the temperature and density range investigated (see Appendix C.4), thereby facilitating the analysis compared to the polar models considered previously[26,28,32–36,111].

4.2.1 Setup

All equilibrium and non-equilibrium MD simulations were performed using a modified version of the software package LAMMPS[54] (version 14Jun16). We employed a fully periodic rectangular simulation box with dimensions $(L_x, L_y, L_z) = (L/2, L/2, L)$, where $L = 41.93\sigma$, containing 13422 solvent particles of LJ diameter σ, which defines the unit of length (see Appendix A.1), and two colloids centred at $\boldsymbol{r}_{\mathrm{h/c}} = (0, 0, \mp L/4)$. Each colloid was modelled with an elastic network of 201 beads with 2808 harmonic springs connecting nearest, second-nearest and third-nearest neighbours. The initial colloid configuration was cut out of an fcc lattice with a density of $0.75/\sigma^3$ matching the solvent density. Springs were then added to all beads within a distance of $R = 4\sigma$ of the centre of mass positions of the two colloids. The equilibrium distances of the harmonic spring potentials were taken to be the initial bead separations and the spring constant was set to $5\epsilon/\sigma^2$, where the LJ parameter ϵ defines the energy scale. During the simulation the colloids were held in place by two additional stiff harmonic springs ($100\epsilon/\sigma^2$) tethering the centres of mass to the equilibrium positions.

The colloidal bead-solvent interactions were modelled with a LJ potential using the same parameters, ϵ and σ, as for the solvent-solvent interactions, and both solvent particles and colloidal beads have the same mass m. Electrostatic interactions were treated with Ewald summation and tin-foil boundary conditions[91]. Cutoff radii for all LJ and real space Coulomb interactions were set to 8σ and the k-space settings were chosen such that the relative accuracy of the force was approximately 10^{-5}, as estimated with the formulas provided in Ref. 112. The equations of motion were integrated using a timestep of $\Delta t = 0.002\tau$, where $\tau = \sigma\sqrt{m/\epsilon}$ is the unit of time.

4.2.2 Equilibration

The initial lattice structure was equilibrated in the NVT ensemble for a period of $2 \times 10^3\tau$ using a Nosé–Hoover thermostat[56,57] with a relaxation time of 0.5τ and a target temperature of $T_\infty = 1.15\epsilon/k_{\mathrm{B}}$, where k_{B} is the Boltzmann constant which was set to unity. Subsequently, all particle velocities of the last configuration were rescaled to match the average kinetic energy of the NVT run, which was followed by a $2 \times 10^3\tau$ long NVE equilibration run. A heat flux was then imposed onto the

system using the eHEX/a algorithm[39], where the rate of energy supplied to the hot (and withdrawn from the cold) colloid was set to $\mathcal{F} = 52.75\epsilon/\tau$. After waiting for a period of $10^4\tau$ for any transient behaviour to disappear and the system to reach a steady state, we started the $1.5 \times 10^5\tau$ long production run and stored snapshots of the trajectory for further post-processing of translational, kinetic temperature and dipole orientations. In addition, we carried out a $1.5 \times 10^5\tau$ long *NVE* simulation in order to subtract non-vanishing equilibrium averages of the spatially averaged field and the dipolar orientations from the NEMD results. The relative increase in the total energy throughout the entire NEMD production run (75 million timesteps) was approximately 0.14%, which is comparable to the value of 0.12% for the equilibrium production run.

4.3 Results

As a first test of the theory, we measured two-dimensional steady state profiles for the temperature and the average dipolar orientations, both shown in Fig. 4.1. To improve statistics, we computed cylindrical averages (indexed by z and s), although the underlying problem does not exhibit full radial symmetry in the xy–plane due to effects of periodic boundary conditions. However, as the theoretical predictions were also cylindrically averaged, the comparison between simulation and theory is still valid. The dashed vertical line going through the origin of Fig. 4.1A corresponds to the equilibrium (or bulk) temperature T_∞. With the temperature values of the specific contour lines shown in the figure and a value of $S^*_{\mathrm{TP}} = 0.216 \pm 0.022$ computed in the vicinity of the origin (see Appendix C.4), we can employ Eq. (4.4) to obtain an estimate of $q^*_{\mathrm{TP}} \approx -0.134$ for the thermally induced charge. If we use the LJ parameters of SPC/E water[61] for the unit conversion, this corresponds to $q_{\mathrm{TP}} \approx 5.15 \times 10^{-3} q_e$, where q_e is the charge of an electron.

Figure 4.1B shows the average dipolar orientations superimposed onto the electric field lines generated by two virtual point charges located at the centres of the colloids. To single out the thermally induced alignment from contributions already present in equilibrium, e.g. the alignment caused by surface layering of solvent molecules in the vicinity of the colloids, we measured equilibrium orientations in a separate simulation and subtracted them from the non-equilibrium result. This procedure assumes that the coupling between the molecular alignment present in equilibrium and the thermally induced one is negligible. We found this assumption to be reasonable everywhere apart from the immediate vicinity of the colloids. Therefore we excluded the first layer of solvent molecules, i.e. all particles within a distance of $R^*_{\mathrm{TP}} = 5$ from

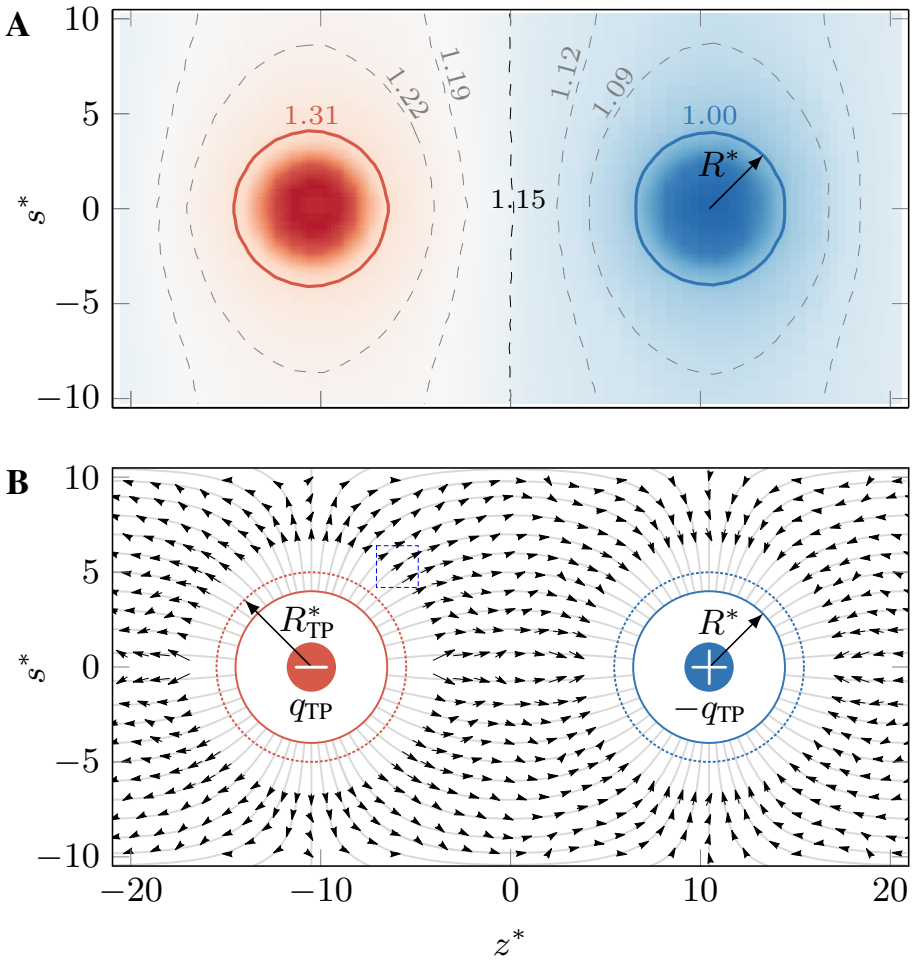

Figure 4.1: Temperature and dipole distributions generated by a pair of heated/cooled colloids. (*A*) Cylindrically averaged temperature profile with symmetry axis z^*, perpendicular direction s^*, and isosurfaces (solid and dashed lines) around two colloids of radius R^*, one heated and the other one cooled. Temperature and quantities labelled with an asterisk are expressed in reduced units. (*B*) Cylindrically averaged electric field lines generated by two point charges, $\pm q_{\mathrm{TP}}$, with fully periodic boundary conditions. The superimposed arrows indicate the average dipolar orientations obtained from the simulations. Averages were calculated inside small volumes (dashed rectangle). To avoid spurious boundary effects, we did not consider dipoles within a radius R^*_{TP} from the center of either colloid.

the colloid centres, from the averaging. The precise value of R_{TP} does not matter as long as it is chosen sufficiently large. We picked the smallest value that allows us to single out the effect. As we can see, the dipoles are aligned very well with the electric field lines generated by two point charges in a fully periodic system.

As a more quantitative test of the theory, we measured the electric field induced by the temperature gradient. To improve the statistical accuracy of our results, we averaged the field over planes perpendicular to the symmetry axis, such that all contributions apart from $E_{z,\mathrm{TP}}$ cancel out. The system behaves as if the two charges of opposite sign are distributed over thin spherical shells of radius R_{TP}, as depicted in Figs 4.2A and B. For this geometry, we obtain the analytical solution for the electric field (see Appendix C.1):

$$\frac{\langle E_{z,\mathrm{TP}}(z)\rangle}{\tilde{E}} = \begin{cases} -1 & \text{if } |z| > z_{\mathrm{c}} + R_{\mathrm{TP}}, \\ +1 & \text{if } |z| < z_{\mathrm{c}} - R_{\mathrm{TP}}, \\ (z - z_{\mathrm{h}})/R_{\mathrm{TP}} & \text{if } |z - z_{\mathrm{h}}| \leq R_{\mathrm{TP}}, \\ (z_{\mathrm{c}} - z)/R_{\mathrm{TP}} & \text{otherwise,} \end{cases} \tag{4.5}$$

where $z_{\mathrm{h/c}} = \mp L/4$ denote the locations of the hot and cold colloid, respectively, L is the box length in the z-direction, $\tilde{E} = q_{\mathrm{TP}}/(2A\epsilon_0)$ is the constant value of the averaged field between the colloids, and $A = L^2/4$ is the cross-sectional area. The left-hand side of the above expression can be related to the average dipole density such that[36]

$$\langle E_{z,\mathrm{TP}}(z)\rangle = -\frac{\langle \rho_\mu(z) - \bar{\rho}_\mu\rangle}{\epsilon_0}, \tag{4.6}$$

where $\bar{\rho}_\mu = 1/L \int \mathrm{d}z \langle \rho_\mu(z)\rangle$ is the box average of $\langle \rho_\mu(z)\rangle$. We note that the dipole density corresponds to the electric polarisation. Equation (4.6) enables us to link the theory and NEMD simulations quantitatively. We can estimate the right-hand side of the above equation readily by sampling the instantaneous dipole orientations and performing temporal and spatial averaging for slabs perpendicular to the symmetry axis. Using Eq. (4.5), we can then infer the value of $\tilde{E}$ from our results and obtain an independent numerical estimate of q_{TP}, in addition to the one provided by Eq. (4.4). Observing a good agreement for both estimates would provide strong support for the theory, since it would suggest that Gauss's theorem can be applied to arbitrary volumes enclosing the colloids, just as if they carried real Coulomb charges. We note, however, that there is an important conceptual difference between estimating the charge using Eq. (4.5) versus Eq. (4.4): the latter already *assumes* that Eq. (4.1) holds whereas the former *validates* it.

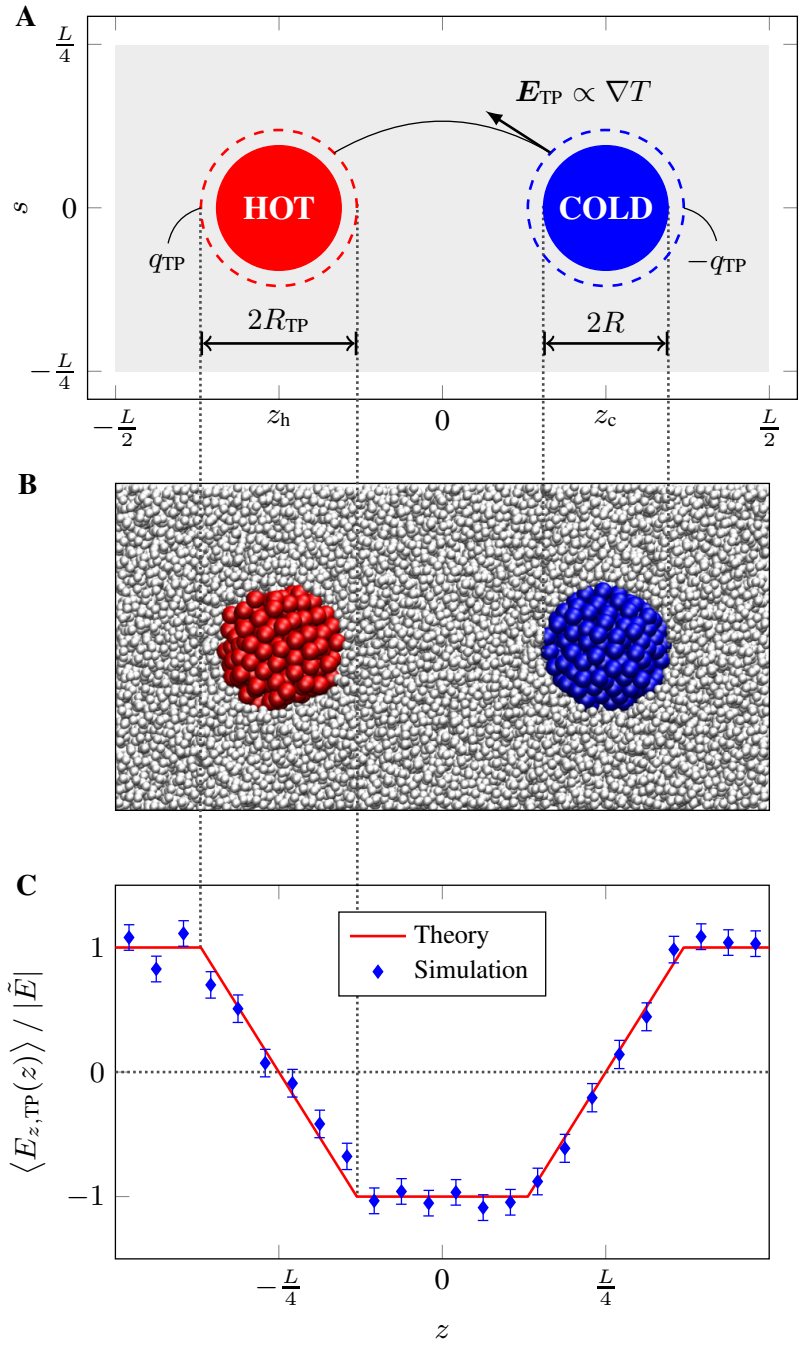

Figure 4.2: Electric field induced by a pair of heated/cooled colloids. (*A*) Illustration of the setup. The dashed lines of radius R_{TP} enclosing the hot and cold colloids represent infinitesimally thin spherical shells carrying the induced charges $\pm q_{\mathrm{TP}}$. The black solid line illustrates a field line and the arrow represents a field vector. (*B*) A typical configuration obtained from simulation showing the colloids immersed into the solvent particles. (*C*) Thermally induced field averaged over slabs perpendicular to the symmetry axis. The simulation results (blue symbols) were calculated from the averaged dipole density excluding two balls of radius R_{TP} centred around the colloids. The solid line shows the theoretical prediction given by Eq. (4.5). The dotted vertical and horizontal lines were added to guide the eye and to highlight the symmetry of the induced field.

Figure 4.2C shows the steady state result for the spatial variation of the averaged field calculated according to Eq. (4.6). Equilibrium averages were subtracted and solvent particles within a distance of R_{TP} from the colloid centres excluded from the averaging, which makes the effective radius of the charge distribution essentially an input parameter of our model. We can see that the simulation data are in excellent agreement with the theoretical expression (4.5): the average field is constant in the fluid region and changes linearly within a distance of R_{TP} from the colloid centre. From the plateau in the centre we estimate $\tilde{E}^* = (-1.96 \pm 0.20) \times 10^{-3}$ for the regions where the field is constant, and find a value of $q_{\mathrm{TP}} = (5.27 \pm 0.54) \times 10^{-3} q_e$ for the thermally induced charge using the SPC/E parameters for the unit conversion. Both estimates for q_{TP} are in excellent agreement. The sign of q_{TP} can be controlled either by changing the rate of energy, $\mathcal{F}$, supplied to or withdrawn from the colloid (flipping hot and cold) or by changing α, such that $\mathrm{sgn}(q_{\mathrm{TP}}) = \mathrm{sgn}(\alpha)\mathrm{sgn}(\mathcal{F})$.

4.4 Conclusions

A key question is whether the effective electric or magnetic charge of colloidal monopoles can be measured in experiments. The present simulations suggest that, at the very least the effect of the monopole fields on probe charges (or dipoles) should be observable. Of course, it would be attractive to make the effect as large as possible by increasing the temperature difference between the particle and the solvent. However, the temperature range is limited by the fact that extreme heating or cooling will bring the system out of the linear-response regime and possibly even induce phase transitions in the solvent. Moreover, the colloidal monopoles differ in an important respect from true monopoles: they cannot be moved by a uniform external field[38]. For an isolated thermal monopole, this follows from the fact that neither its self-energy, i.e. the energy of the electric field around it, nor the interaction energy between the external field and solvent dipoles exhibit a dependence on the position of the thermal monopole. It is therefore tempting (be it slightly frivolous) to call such colloidal monopoles 'quacks', as they quack like a duck (i.e. they create a field similar to that of a real monopole), but they don't swim like a duck (they cannot be used to transport charge). One of the main effects that may obscure observation of the Coulomb-like interaction between oppositely heated colloids is thermophoresis, which will also cause colloids to move in the temperature gradient caused by another colloid. However, at least in the linear regime, this effect should cause otherwise identical but oppositely heated colloids to move *in the same direction* with respect to the fluid rather than with respect to one another. Finally, there are many open

questions about the practical consequences of the existence of thermal monopoles. It is, for instance, conceivable that such particles in an electrolyte solution will get 'decorated' with real charges, and thereby acquire real charge (opposite and equal to the 'thermal' charge) that can be dragged along. That charge should respond to a uniform external field: the resulting electro-osmotic flow would cause motion of the colloids.

5

Prediction of thermal polarisation

Preface

The manuscript underlying this chapter is entitled 'Theoretical prediction of thermal polarisation' by P. Wirnsberger, C. Dellago, D. Frenkel and A. Reinhardt. It has been accepted for publication in *Physical Review Letters* and a free version of the article is available for download on the arXiv (https://arxiv.org/pdf/1804.03624.pdf).

The author contributions are as follows: A. Reinhardt and I performed the research and analysed the data; all authors designed the research together and wrote the manuscript following my initial draft.

5.1 Mean-field theory

Microscopic interactions in systems out of thermal equilibrium are typically limited to a phenomenological treatment based on the theory of non-equilibrium thermodynamics[3]. While this theory predicts a linear relationship between the TP field and the temperature gradient[26] [see Eq. (3.4)], as shown in Eq. (3.4), it involves phenomenological coefficients that are unknown and require fitting to simulation data. Recently, this shortcoming was addressed by using a different theoretical approach based on a mean-field treatment[30]. The theory was shown to capture the scaling of the induced alignment of size-asymmetric polar dumbbell molecules accurately, but it involves an unknown parameter that is either estimated from dimensional arguments or fitted to simulation data.

In principle, it should be possible to eliminate this restriction, so that quantitative predictions can be made solely based on the knowledge of the molecular geometry, the local thermodynamic state and the prevailing temperature and density gradients. In this chapter, we propose a mean-field approach to predict the thermally induced

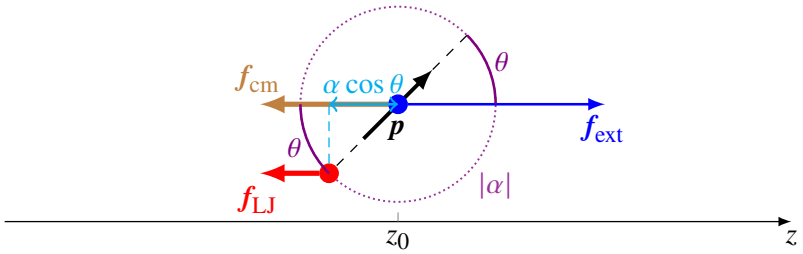

Figure 5.1: An off-centre Stockmayer particle and an illustration of the steady-state force balance. The centre of mass (blue circle) of the off-centre Stockmayer particle is located at z_0 and coincides with the location of the point dipole $\boldsymbol{p}$ (black arrow). At steady state, the external force $\boldsymbol{f}_{\mathrm{ext}}$ (blue arrow) is balanced by a force $\boldsymbol{f}_{\mathrm{cm}}$ (brown arrow) acting at the centre of mass and a force $\boldsymbol{f}_{\mathrm{LJ}}$ (red arrow) acting at the LJ centre. Upon rotating the dipole by an angle θ relative to the z-axis, the z-position of the LJ centre is $z_0 + \alpha\cos\theta$ (since $\alpha < 0$).

alignment of an off-centre Stockmayer liquid without the need for any additional fitting parameters. To avoid notational confusion with the chemical potential μ, we use $\boldsymbol{p}$ to denote the dipole moment in this chapter. The relative displacement of the LJ site of an off-centre Stockmayer particle is then given by $\alpha\hat{\boldsymbol{p}}$ (Fig. 5.1), where α controls the level of molecular asymmetry, and $\hat{\boldsymbol{p}} = \boldsymbol{p}/|\boldsymbol{p}|$[37]. Although we use reduced units (see Appendix A.1), we drop the asterisk for notational convenience and use $\alpha = -1/4$, in line with previous work[37].

To simplify the theoretical treatment, we assume that (i) the effect can be described by considering a single particle only, (ii) the average net force acting on this particle vanishes in the steady state, and (iii) the system is at local equilibrium. Suppose thermodynamic quantities and forces of interest vary along the z-axis. In this case, the orientation of the particle can be defined by the polar angle between its dipole moment vector and this axis, $\cos\theta = \hat{\boldsymbol{p}}\cdot\hat{\boldsymbol{z}}$. If we have an effective Hamiltonian $H(\cos\theta;\, z_0)$ that can account for the energy change upon rotating a particle about its centre of mass at position z_0 (Fig. 5.1), we can compute the Boltzmann-weighted average of the induced orientation[30],

$$\langle\cos\theta(z_0)\rangle = \frac{1}{Q(z_0)}\int_{-1}^{1} q\exp[-\beta(z_0)H(q;\, z_0)]\,\mathrm{d}q, \tag{5.1}$$

where $Q(z_0) = \int_{-1}^{1}\exp[-\beta H(q;\, z_0)]\,\mathrm{d}q$, $\beta(z_0) = 1/k_{\mathrm{B}}T(z_0)$, $T(z_0)$ is the absolute temperature and k_{B} is Boltzmann's constant. Integration over the azimuth angle is omitted because contributions in the numerator and the denominator cancel out.

According to assumption (ii), on average all forces acting on a particle add up to zero so that the system does not undergo continual net acceleration. Individual forces can, however, act at different locations within the particle and thereby generate a torque. There are three possible sites at which these forces could attach in our model

system: the LJ site, the point dipole and the centre of mass. Since the latter two coincide, any external force $f_{\mathrm{ext}}\hat{\boldsymbol{z}}$ acting on the particle must be balanced by the sum of a force $f_{\mathrm{cm}}\hat{\boldsymbol{z}}$ acting on the centre of mass and a force $f_{\mathrm{LJ}}\hat{\boldsymbol{z}}$ acting on the LJ site, such that

$$f_{\mathrm{LJ}} + f_{\mathrm{cm}} + f_{\mathrm{ext}} = 0. \tag{5.2}$$

The overall torque acting on the particle is therefore given by $\alpha\hat{\boldsymbol{p}} \times \boldsymbol{f}_{\mathrm{LJ}}$. An infinitesimal rotation changes the energy by $-f_{\mathrm{LJ}}\alpha\,\mathrm{d}(\cos\theta)$. However, this rotation polarises the liquid, and we thus also need to account for the coupling between the dipole and the mean electric field $\langle E(z_0)\rangle$. Combining both contributions, we can approximate the total work done to rotate the particle as

$$H(\cos\theta; z_0) = -\alpha\cos\theta f_{\mathrm{LJ}}(z_0) - p\cos\theta\langle E(z_0)\rangle. \tag{5.3}$$

Using this Hamiltonian, the integral in Eq. (5.1) yields

$$\langle\cos\theta(z_0)\rangle = \coth\xi - \xi^{-1} = \frac{\xi}{3} + O(\xi^3), \tag{5.4}$$

where $\xi = -\alpha f_{\mathrm{LJ}}(z_0) - p\langle E(z_0)\rangle$. For $|\xi| \ll 1$, we can truncate the series at linear order in ξ. We further approximate the field self-consistently using[30]

$$\langle E(z_0)\rangle \approx -4\pi\rho(z_0)p\langle\cos\theta(z_0)\rangle, \tag{5.5}$$

where $\rho(z_0)$ is the number density, and thus obtain our central result,

$$\langle\cos\theta(z)\rangle = \frac{\beta(z)\alpha f_{\mathrm{LJ}}(z)}{3 + 4\pi\rho(z)\beta(z)p^2}. \tag{5.6}$$

Apart from the nature of the force, this expression is analogous to Eq. (11) of Ref. 30.

We note that our choice of using the Maxwell field [Eq. (5.5)] for evaluating the energy in Eq. (5.3) is subject to debate. In fact, the question of what is the correct expression for predicting the magnitude of dipolar alignment in the presence of an external electric field has been studied extensively for more than a century[106]. Our particular choice may not be suitable for estimating the dielectric constant assuming linear response, because it can lead to negative values. However, the numerical results presented in the next section strongly suggest that it yields accurate predictions for the thermally induced orientation. We will therefore leave a detailed investigation into this matter for future work, as it is beyond the scope of this Chapter.

5.2 Simulation results

In order to benchmark the predictions of this equation against simulation results, we ran NEMD simulations of an off-centre Stockmayer fluid in a quasi one-dimensional geometry. We imposed temperature and density gradients by simulating a hot and a cold reservoir orthogonal to the z-axis[36], so that all thermodynamic driving forces varied only along z. Following the approach of Daub *et al.*[34], we disentangled the effects of temperature and density gradients by applying a body force to each particle. In '$\nabla\rho$-runs', we generated a density gradient by applying a body force to the centre of mass of each particle in an equilibrium NVT simulation. Similarly, in '∇T-runs', we eliminated the density gradient by applying a body force of opposite sign to the full NEMD-run. This procedure allowed us to decompose the full non-equilibrium phenomenon into an equilibrium problem at constant temperature and a non-equilibrium problem at constant density.

5.2.1 Off-centre Lennard-Jones particles

We show typical ρ and T profiles of all three runs for an off-centre LJ system (i.e. at zero dipole strength) in Fig. 5.2a. We adjusted the applied body forces to yield gradients within 1% of the NEMD results. Full technical details of the simulation set-up are given in Appendix D.1.

The applied body force in simulation corresponds to f_{ext} in Fig. 5.1. To determine f_{LJ}, we first compute f_{cm} and then invoke the force-balance argument [Eq. (5.2)], $f_{\text{LJ}} = -f_{\text{ext}} - f_{\text{cm}}$. In the absence of a dipole moment, the centre of mass itself does not exhibit any direct interaction with other particles. In simulations, forces are computed from gradients of the potential energy, and so do not include thermodynamic forces arising from momentum degrees of freedom. The z component of the average force derived from the potential energy, $\langle f_i \rangle$, balances such 'ideal' forces at steady state; we demonstrate in Appendix D.3 that $\langle f_i \rangle = f_{\text{ext}}^{\text{id}}$, where

$$f_{\text{ext}}^{\text{id}} = \begin{cases} \left(\dfrac{\partial \mu^{\text{id}}}{\partial \rho}\right)_T \dfrac{\mathrm{d}\rho}{\mathrm{d}z} = \dfrac{k_{\text{B}}T}{\rho}\dfrac{\mathrm{d}\rho}{\mathrm{d}z} & \text{for } \nabla\rho\text{-runs,} \\ \left[s^{\text{id}} + \left(\dfrac{\partial \mu^{\text{id}}}{\partial T}\right)_\rho\right] \dfrac{\mathrm{d}T}{\mathrm{d}z} = k_{\text{B}} \dfrac{\mathrm{d}T}{\mathrm{d}z} & \text{for } \nabla T\text{-runs,} \end{cases} \tag{5.7}$$

with μ^{id} being the ideal chemical potential and s^{id} the ideal entropy per particle. To compute f_{LJ}, we need to consider where the force compensating $f_{\text{ext}}^{\text{id}}$ acts. Although the attachment site of this force is not immediately obvious, comparison with simulation data for $\langle \cos\theta \rangle$ answers this question unambiguously: the term proportional

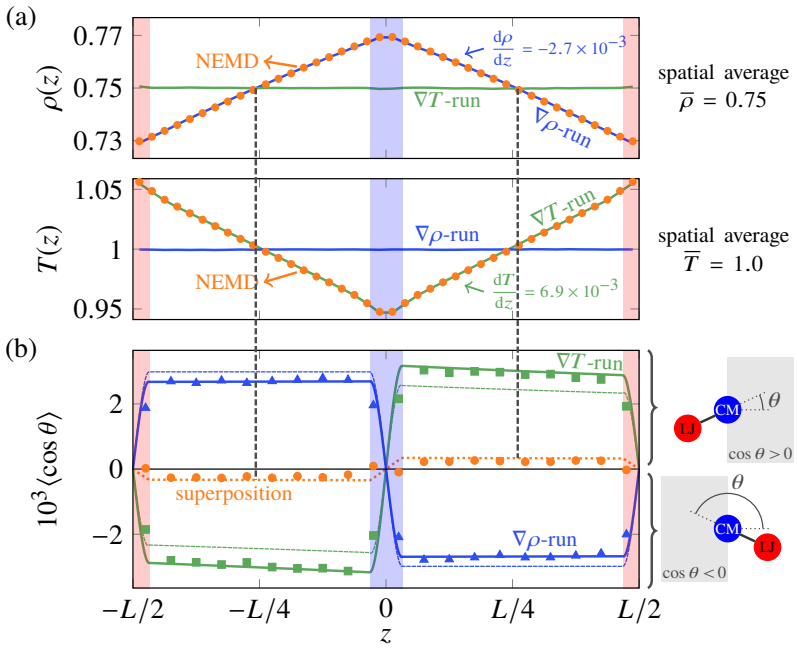

Figure 5.2: Off-centre LJ ($p^2 = 0$ and $L = 31.45$). (a) Density and temperature profiles for NEMD-, $\nabla\rho$- and ∇T-runs with reservoirs highlighted (shaded regions). (b) Mean orientation from simulation (symbols) and theoretical predictions (solid lines). Dashed coloured lines correspond to incorrect attachment sites of $f_{\text{ext}}^{\text{id}}$. Points at which force superposition (dotted line) is expected to perform well are indicated by dashed vertical lines. Symbols are larger than error bars.

to $\nabla\rho$ acts on the centre of mass ($f_{\text{cm}}^{(\nabla\rho)} = -f_{\text{ext}}^{\text{id}}$), and the term proportional to ∇T acts on the LJ site (so that $f_{\text{cm}}^{(\nabla T)} = 0$). The force-balance argument [Eq. (5.2)] thus gives

$$f_{\text{LJ}} = -f_{\text{ext}} + \begin{cases} \frac{k_{\text{B}}T}{\rho}\frac{\mathrm{d}\rho}{\mathrm{d}z} & \text{for } \nabla\rho\text{-runs,} \\ 0 & \text{for } \nabla T\text{-runs.} \end{cases} \tag{5.8}$$

Using this expression and fits to the sampled temperature and density profiles, we employ Eq. (5.6) to obtain a theoretical estimate of $\langle\cos\theta\rangle$.

We show the theoretical prediction and simulation data for a representative thermodynamic state in Fig. 5.2b, alongside alternative predictions with the attachment sites of $f_{\text{ext}}^{\text{id}}$ swapped (dashed lines), demonstrating that our choice of attachment sites in Eq. (5.8) is correct. Theoretical predictions agree remarkably well with simulation data in the regions outside the reservoirs. In the vicinity of the reservoirs, the agreement is worse; this may be due to the discontinuous nature of the employed thermostat, which creates an interface and likely violates our assumption of local equilibrium. Interestingly, the density gradient induces a rotation of the LJ centre towards lower densities, while the temperature gradient has the opposite effect. In each case, the alignment is an order of magnitude higher than in the full NEMD case. These individual gradients also allow us to estimate the full NEMD result

for the points at which ρ and T agree in all three runs, i.e. at $z = \pm L/4$, where $\rho = \overline{\rho}$ and $T = \overline{T}$. To this end, we summed the two forces in Eq. (5.8) and employed Eq. (5.6) together with the full NEMD temperature and density profiles. We show in Fig. 5.2b that the superposition estimate is in rather good agreement with the simulation result not only for $z = \pm L/4$, but everywhere outside the reservoirs. The near quantitative agreement with simulation results demonstrates that our theory captures the underlying physics accurately in the non-polar case and suggests that the assumptions underlying our theoretical treatment are reasonable.

5.2.2 Off-centre Stockmayer particles

Next, we studied the behaviour of an off-centre Stockmayer fluid for different dipole strengths $p^2 \in [0, 3]$. To make comparisons meaningful, we chose a reference state of $\overline{T} = 1.25$ and $\overline{\rho} = 0.82$, at which an equilibrium Stockmayer fluid is a liquid for all dipole strengths considered[113]. We imposed the same temperature gradient in all NEMD-runs by fixing the reservoir temperatures while letting the induced density vary freely as a function of p^2 (Appendix D.3). To rule out the presence of a nematic or ferrofluidic phase, we measured the correlation functions $h_{110}(r)$ and $h_{220}(r)$ and verified that both vanish in the limit $r \to \infty$[114]. As in the non-polar case, the crucial quantity for our theory is f_{LJ}, whose estimation is now complicated by electrostatic dipole–dipole interactions. The dipole is located at the centre of mass, and any dipole-induced isotropic force contribution is assumed to attach to that site, adding to f_{cm}.

Suppose $f_{\mathrm{ext}}(p^2)$ is the external force that generates the target density gradient in a $\nabla\rho$-run with dipole strength p^2. This force differs from that required to generate the same density gradient in the non-polar case by $\Delta f_{\mathrm{dip}}(p^2) = f_{\mathrm{ext}}(p^2) - f_{\mathrm{ext}}(0)$. Since all other parameters are kept fixed, we can attribute the entirety of this force to the presence of the dipole. An analogous result holds for the ∇T-run, where the force difference is evaluated for a fixed temperature gradient at constant density. In order to employ the force-balance argument [Eq. (5.2)] to compute f_{LJ}, we also need to determine where the ideal forces [Eq. (5.7)] attach. In the non-polar case, the ideal force proportional to $\nabla\rho$ acted at the centre of mass. We do not expect this behaviour to change for $p^2 \neq 0$. However, the situation is less clear for the ∇T contribution, which we initially assigned solely to the LJ site. It is not unreasonable to assume that for sufficiently large p^2, because the dipole moment site is at the centre of mass, some part of this balancing ideal force will also act at this site, but the dipole strength at which this shift becomes relevant to our theory is not obvious. For a Stockmayer system, a dipole strength of $p^2 = 0.25$ constitutes an almost negligible

thermodynamic contribution to pure LJ[115], and we do not therefore expect the behaviour to change qualitatively in this case. However, electrostatic contributions increase rapidly with p^2[115]; we thus assume that for $p^2 \geq 1$, the ideal balancing force is split equally between f_{LJ} and f_{cm}. As we lack further insight into the precise mechanism by which this process occurs, our choice is rather arbitrary, and, for completeness, we also provide the results for an alternative choice in Appendix D.2. Gathering all contributions and assuming force-balance [Eq. (5.2)], we find

$$f_{\mathrm{LJ}}(p^2) = -f_{\mathrm{ext}}(0) + \begin{cases} \frac{k_{\mathrm{B}}T}{\rho}\frac{\mathrm{d}\rho}{\mathrm{d}z} & \text{for } \nabla\rho\text{-runs,} \\ 0 & \text{for } \nabla T\text{-runs if } p^2 < 1, \\ \frac{1}{2}k_{\mathrm{B}}\frac{\mathrm{d}T}{\mathrm{d}z} & \text{for } \nabla T\text{-runs if } p^2 \geq 1. \end{cases} \tag{5.9}$$

Apart from the behaviour of the ideal force, this result is identical to Eq. (5.8). The difference between $f_{\mathrm{LJ}}(p^2)$ and $f_{\mathrm{LJ}}(0) \equiv f_{\mathrm{LJ}}$ is that all terms are evaluated for a different thermodynamic state, since the density profile changes with dipole strength (Appendix D.3).

We compare simulation results to the theoretical estimates obtained with Eqs (5.6) and (5.9) (Fig. 5.3). For the $\nabla\rho$- and ∇T-runs, the magnitude of the alignment is maximal for $p = 0$ and decreases quickly with p due to the energetically unfavourable interaction with the total electric field. For the highest dipole strength ($p^2 = 3$),

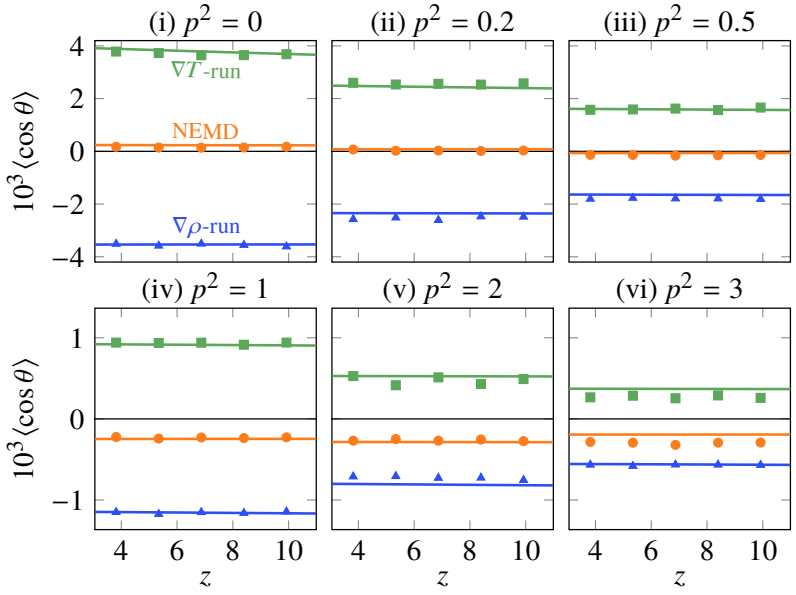

Figure 5.3: Mean orientation for an off-centre Stockmayer liquid at varying dipole strength. $L = 30.53$. Symbols represent simulation results and solid lines correspond to theoretical predictions. Only the region between the reservoirs is shown for compactness. Simulation results were averaged over both halves of the simulation box to improve statistics.

the induced alignment is approximately an order of magnitude lower than in the non-polar case ($p^2 = 0$). Intriguingly, the presence of the dipole flips the sign of the orientation in the NEMD-run, a feature not observed for size-asymmetric polar dumbbell molecules[34]. The zero-crossing happens close to $p^2 = 0.2$, where the alignment due to the density gradient is almost exactly compensated by the temperature gradient. Furthermore, the full NEMD result remains largely unchanged for $p^2 \geq 1$, perhaps indicating that the effect becomes saturated. Overall, our theoretical prediction agrees very well with the simulation data. By construction, absolute errors in the predictions for the individual gradient contributions propagate to the prediction for the full NEMD result because we superimpose the forces. This point is well illustrated for $p^2 = 3$, where the $\sim$20% error in the prediction of the ∇T-run result causes the estimate for the NEMD-run to be shifted by the same constant. Nevertheless, despite this limitation, these results suggest that our mean-field theory captures the essential physics underlying this non-equilibrium phenomenon very well.

5.3 Predicting the steady-state force

So far, we have treated f_{LJ} as an input parameter of the theory and we determined it numerically to either match or eliminate a density gradient. However, we may be able to predict the force acting on the LJ site from the LJ equation of state (EOS). Although we do not have an exact expression for this EOS, accurate fits exist[116,117] and can readily be implemented. Starting from the Gibbs–Duhem relation, we find an explicit expression for the external force in terms of the chemical potential μ (Appendix D.2),

$$f_{\mathrm{ext}} = \left(\frac{\partial \mu}{\partial \rho}\right)_T \frac{\mathrm{d}\rho}{\mathrm{d}z} + \left[s + \left(\frac{\partial \mu}{\partial T}\right)_\rho\right] \frac{\mathrm{d}T}{\mathrm{d}z}. \tag{5.10}$$

At local equilibrium, this force will be exactly balanced by a pressure-gradient force

$$f_{\mathrm{balance}} = f_{\mathrm{cm}} + f_{\mathrm{LJ}} = -\frac{1}{\rho}\left[\left(\frac{\partial P}{\partial T}\right)_\rho \frac{\mathrm{d}T}{\mathrm{d}z} + \left(\frac{\partial P}{\partial \rho}\right)_T \frac{\mathrm{d}\rho}{\mathrm{d}z}\right], \tag{5.11}$$

so that the sum of both forces vanishes. For $\nabla\rho$-runs, all terms in Eq. (5.10) that involve a temperature gradient vanish, and vice versa for ∇T-runs, so the external force can be written as

$$f_{\mathrm{ext}}(0) = \begin{cases} (\partial\mu/\partial\rho)_T \, (\mathrm{d}\rho/\mathrm{d}z) & \text{for } \nabla\rho\text{-runs,} \\ \left[s + (\partial\mu/\partial T)_\rho\right](\mathrm{d}T/\mathrm{d}z) & \text{for } \nabla T\text{-runs.} \end{cases} \tag{5.12}$$

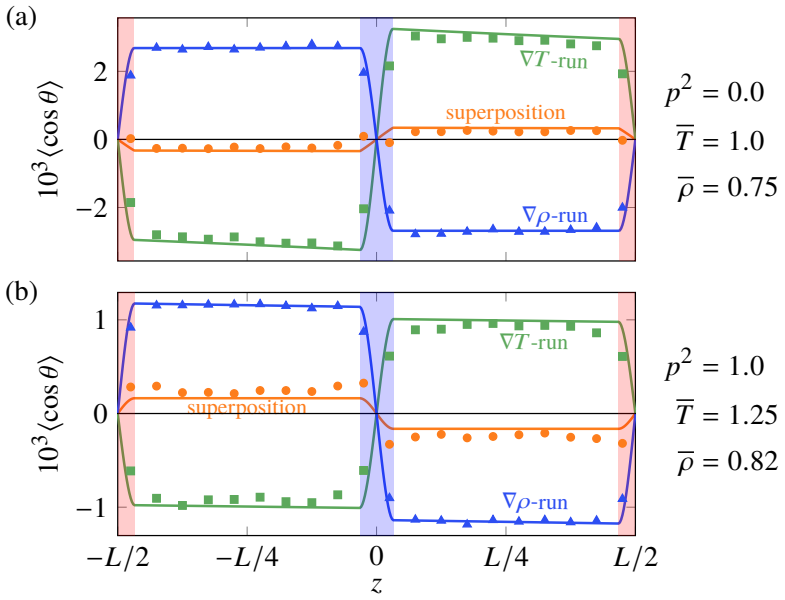

Figure 5.4: Mean orientation from simulation (symbols) and theoretical predictions (solid lines) using an EOS-derived estimate of f_{LJ}. Symbols are larger than error bars. (a) State corresponding to Fig. 5.2. (b) State corresponding to Fig. 5.3iv.

Therefore, to generate for example a density gradient, instead of manually adjusting the external force until we get agreement with NEMD results, we can use the Johnson EOS[116] and Eq. (5.12) to *predict* it by multiplying the derivative of the chemical potential by the density gradient we wish to match. For suitably large system sizes, we find the simulation result to be in excellent agreement with the target value with a deviation of less than 1%. The prediction of the force to cancel the gradient in ∇T-runs is less accurate, with a deviation of ∼2.5%.

A comparison of simulation results with the theoretical prediction of Eqs (5.6) and (5.12) using the Johnson EOS[116] is shown in Fig. 5.4. For off-centre LJ (Fig. 5.4a), the predictions are almost as accurate as the ones obtained with the numerically determined force (Fig. 5.2b). The agreement is excellent for the $\nabla\rho$-run and exhibits only a slight deviation of approximately 5% for the ∇T-run. Superposition of the forces yields again an accurate estimate for the NEMD result with a deviation of only ∼20%. For the polar case (Fig. 5.4b), the EOS estimate yields very accurate predictions for the $\nabla\rho$-run and overestimates the alignment in the ∇T-run only slightly. The prediction for the NEMD-run is shifted by the same constant and is off by approximately 30% compared to the simulation result. Although the estimates are not quite as accurate as the original ones (Fig. 5.3), we find it remarkable that such good agreement can be achieved solely based on the LJ EOS. While not perfect, such a route can provide a particularly facile back-of-the-envelope estimate of the degree of molecular alignment without the need to perform any simulations at all.

5.4 Conclusions

We have proposed a mean-field theory to explain the thermo-orientation and -polarisation effects exhibited by an off-centre Stockmayer liquid. Our theoretical predictions are in almost quantitative agreement with simulation results for a range of dipole strengths, including in the absence of any dipole. In line with previous work[30], we find that the two effects are caused by the same underlying physical mechanism. Differences in the predicted alignment as a function of the dipole strength are mainly caused by the energetic penalty for forming an electric field and the behaviour of ideal forces when dipoles are present. By separating temperature and density gradients using an applied body force, we found that the individual contributions lead to an alignment of opposite sign, which can be rationalised by the requirement for overall force balance in the non-equilibrium steady state. Finally, we demonstrated that very reasonable predictions can be obtained solely based on the equation of state for LJ and the non-equilibrium temperature and density profiles. In future work, it will be interesting to see whether our theory can be extended to water, where quadrupolar interactions are known to play an important role in thermal polarisation[35,36].

6

Summary and conclusions

In this thesis, we investigated the phenomenon of thermally induced polarisation using a combination of theory and simulation. We first proposed a new thermostatting algorithm, the eHEX algorithm, for NEMD simulations of thermal gradients. This algorithm is very well suited to the simulation of a physical system to which energy is supplied at a constant rate, such as a metal NP heated by a laser. To resolve the severe energy drift exhibited by the HEX algorithm, on which the eHEX algorithm is based, we derived the lowest-order truncation error of the numerical integration scheme and eliminated it through an additional coordinate integration step. This procedure fixed the energy loss entirely; even in very long simulations, involving 10^8 timesteps, we have not observed any appreciable energy loss compared to an equilibrium simulation. In future work, it would be interesting to extend the algorithm to account for rotational degrees of freedom in the thermostatting, so as to enable the algorithm to be fully compatible with rigid-body integration schemes.

Using the eHEX algorithm, we then studied the behaviour of water under the influence of a strong temperature gradient. We focused primarily on the treatment of electrostatic interactions, which were truncated using the Wolf method in most of the previous work on the TP effect. Our simulation results for Ewald summation suggest that the induced electric field was previously overestimated due to this truncation, and is, in fact, an order of magnitude weaker than assumed. Moreover, we showed that truncation of electrostatic interactions can flip the sign of molecular orientations and therefore lead to artefacts in the dipole density. By considering two different multipole expansions, we showed that, for inhomogeneous polarisations, the quadrupole contribution can be significant and even outweigh the dipole contribution to the electric field. Finally, we proposed a more accurate way of calculating the electrostatic potential and the field. In particular, we showed that averaging the microscopic field analytically to obtain the macroscopic Maxwell field reduces the

error bars by up to an order of magnitude. As a consequence, the simulation times required to reach a given statistical accuracy decrease by up to two orders of magnitude. We think that our general approach could also be of benefit to other systems with a quasi one-dimensional geometry and a similar signal-to-noise ratio.

Quadrupolar contributions to the thermal polarisation of water complicate the theoretical study of thermally induced monopoles. To probe this interesting theory numerically, we therefore devised an off-centre Stockmayer model that exhibits the TP effect while particles carry only a dipole moment. We then performed NEMD simulations of a pair of heated/cooled colloidal particles immersed in such a liquid. Our simulation results clearly demonstrate that the molecular dipoles are well aligned with the electric field generated by two virtual charges, in agreement with the theoretical prediction. We can therefore describe the overall net electrostatic interaction between the colloidal particles by two Coulomb charges of opposite sign, representing a hugely simplified picture compared to the original non-equilibrium problem. However, it turns out that the effect is very small and may therefore be challenging to observe experimentally. More work is necessary to identify suitable observables for comparison with experiments and to map out parameters which maximise the thermo-charge.

Exploring the TP effect numerically requires very long simulations and is computationally expensive due to the presence of long-range electrostatic interactions. To avoid this bottleneck, we therefore devised a mean-field theory to predict the TP effect exhibited by an off-centre Stockmayer liquid theoretically. Unlike previous theories that are based either on phenomenological equations or on scaling arguments, our approach does not require any fitting parameters. Given an equation of state and assuming local equilibrium, we constructed an effective Hamiltonian for computing local Boltzmann averages. This simple theoretical treatment predicts molecular orientations that are in very good agreement with simulation results for the range of dipole strengths investigated. By decomposing the overall alignment into contributions from the temperature and density gradients, we shed further light on how the non-equilibrium result arises from the competition between the two gradients. While not perfect, our theoretical predictions can be hugely beneficial for screening large regions of the phase diagram to find thermodynamic states that maximise the TP effect. An interesting extension for future work would be the inclusion of quadrupolar interactions, so that our theory can be applied to water and used as a guide for experimentalists in their search for the effect.

Finally, most of the past research on the TP effect has focused primarily on understanding the scaling and the magnitude of the effect using computer simulations.

Based on the promising theoretical advances due to mean-field approaches, we hope that future investigations will focus on improving the theoretical description to shed further light on the physical mechanism underlying this curious non-equilibrium effect.

Appendix A

Heat exchange algorithm

A.1 Reduced units

In the following, ε is the LJ well depth, σ is the LJ particle diameter, k_B is the Boltzmann constant, ε_0 is the electric constant and m is the particle mass. We non-dimensionalise all quantities in terms of these basic units, as shown in the table below.

Reduced quantity	Definition
distance ℓ^*	ℓ/σ
number density ρ^*	$\rho\sigma^3$
force f^*	$f\sigma/\varepsilon$
time t^*	$t/\sqrt{\sigma^2 m/\varepsilon}$
temperature T^*	$k_\mathrm{B}T/\varepsilon$
dipole moment p^*	$p/\sqrt{4\pi\varepsilon_0\varepsilon\sigma^3}$

A.2 Exact solution

We would like to show that the rescaling step

$$\boldsymbol{v}_i(t) = \xi\boldsymbol{v}_i(0) + \big(1-\xi\big)\boldsymbol{v}_\Gamma(0) \tag{A.1}$$

of the HEX algorithm is the exact solution of

$$\dot{\boldsymbol{v}}_i = \frac{\mathcal{F}}{2\mathcal{K}}(\boldsymbol{v}_i - \boldsymbol{v}_\Gamma), \tag{A.2}$$

where $\mathcal{K}$ is given by Eq. (2.1) and ξ by Eq. (2.3). We will first show that $\mathcal{F}/2\mathcal{K}$ is independent of the particle velocities and only a function of time. This can be seen

easily by considering the time evolution of the internal kinetic energy, which is given by

$$\frac{\mathrm{d}\mathcal{K}}{\mathrm{d}t} = \sum_{i\in\gamma} m_i \left(\boldsymbol{v}_i - \boldsymbol{v}_\Gamma\right) \cdot \left(\dot{\boldsymbol{v}}_i - \dot{\boldsymbol{v}}_\Gamma\right) \tag{A.3a}$$

$$= \mathcal{F} \tag{A.3b}$$

and therefore we can write $\mathcal{K}(t) = \mathcal{K}(0) + \mathcal{F}t$. We note that we can exchange the order of taking the time derivative and the summation, because the particle positions are fixed during this operation. At the same time, it is easy to see that the centre of mass velocity is constant in time since

$$\frac{\mathrm{d}\boldsymbol{v}_\Gamma}{\mathrm{d}t} = \frac{1}{m_\Gamma} \sum_{i\in\gamma} m_i \dot{\boldsymbol{v}}_i \tag{A.4}$$

$$= \frac{1}{m_\Gamma} \sum_{i\in\gamma} m_i \left[\frac{\mathcal{F}}{2\mathcal{K}} \left(\boldsymbol{v}_i - \boldsymbol{v}_\Gamma\right)\right] \tag{A.5}$$

$$= 0. \tag{A.6}$$

In order to solve Eq. (A.2) analytically, it is advantageous to carry out a variable transformation first. Let us consider the transformation $\boldsymbol{v}_i \mapsto \bar{\boldsymbol{v}}_i = \boldsymbol{v}_i - \boldsymbol{v}_\Gamma$. With the definition

$$\lambda(t) = \frac{\mathcal{F}}{2\left[\mathcal{K}(0) + \mathcal{F}t\right]}, \tag{A.7}$$

we can express the time evolution of the new velocities as

$$\dot{\bar{\boldsymbol{v}}}_i = \lambda \bar{\boldsymbol{v}}_i. \tag{A.8}$$

The solution of this equation is then given by

$$\bar{\boldsymbol{v}}_i(t) = \mathrm{e}^{\int_0^t \mathrm{d}t' \ \lambda(t')} \bar{\boldsymbol{v}}_i(0) = \xi \bar{\boldsymbol{v}}_i(0). \tag{A.9}$$

If we substitute the old variables back, we recover Eq. (A.1) which proves the assertion.

A.3 Splitting error

In this section, we sketch the derivation of the leading-order error term of the coordinate integration arising from the operator splitting in the HEX algorithm. To

this end, we evaluate the expression

$$\mathcal{E}r_{i,\alpha} = \left(\frac{1}{12}\big[iL_2,[iL_2,iL_1]\big] - \frac{1}{24}\big[iL_1,[iL_1,iL_2]\big]\right) r_{i,\alpha} \tag{A.10}$$

for the operators

$$iL_1 = \sum_{j=1}^{N} \sum_{\beta\in\{x,y,z\}} \frac{\eta_{j,\beta}}{m_j} \frac{\partial}{\partial v_{j,\beta}}, \tag{A.11a}$$

$$iL_2 = \sum_{j=1}^{N} \sum_{\beta\in\{x,y,z\}} \left[\frac{f_{j,\beta}}{m_j} \frac{\partial}{\partial v_{j,\beta}} + v_{j,\beta} \frac{\partial}{\partial r_{j,\beta}}\right]. \tag{A.11b}$$

For the first term in Eq. (A.10) we find

$$\begin{aligned}
&\big[iL_2,[iL_2,iL_1]\big] r_{i,\alpha} \\
&= -2\sum_{j=1}^{N}\sum_{\beta} \left[\frac{f_{j,\beta}}{m_j} \frac{\partial}{\partial v_{j,\beta}} + v_{j,\beta} \frac{\partial}{\partial r_{j,\beta}}\right] \frac{\eta_{i,\alpha}}{m_i} && \text{(A.12a)} \\
&= -\frac{2}{m_i} \sum_{j\in\gamma_{k(\boldsymbol{r}_i)}} \sum_{\beta} \frac{f_{j,\beta}}{m_j} \frac{\partial \eta_{i,\alpha}}{\partial v_{j,\beta}}, && \text{(A.12b)}
\end{aligned}$$

omitting summation bounds for β for readibility. In the last step we assumed that particles do not cross reservoir boundaries, in which case $\eta_{i,\alpha}$ depends only on the velocities of particles within the reservoir $\Gamma_{k(\boldsymbol{r}_i)}$. For the second term in Eq. (A.10) we find

$$\big[iL_1,[iL_1,iL_2]\big] r_{i,\alpha} = \frac{1}{m_i} \sum_{j\in\gamma_{k(\boldsymbol{r}_i)}} \sum_{\beta} \frac{\eta_{j,\beta}}{m_j} \frac{\partial \eta_{i,\alpha}}{\partial v_{j,\beta}} \tag{A.13}$$

and combining the two expressions we get

$$\mathcal{E}r_{i,\alpha} = -\frac{1}{6m_i} \sum_{j\in\gamma_{k(\boldsymbol{r}_i)}} \sum_{\beta} \frac{1}{m_j} \left(f_{j,\beta} + \frac{\eta_{j,\beta}}{4}\right) \frac{\partial \eta_{i,\alpha}}{\partial v_{j,\beta}}. \tag{A.14}$$

It is straightforward to compute the derivative

$$\begin{aligned}
\frac{\partial \eta_{i,\alpha}}{\partial v_{j,\beta}} = \frac{m_i \mathcal{F}_{\Gamma_{k(\boldsymbol{r}_i)}}}{2\mathcal{K}_{\Gamma_{k(\boldsymbol{r}_i)}}} \Bigg[&\delta_{\alpha,\beta}\left(\delta_{i,j} - \frac{m_j}{m_{\Gamma_{k(\boldsymbol{r}_i)}}}\right) \\
&- \frac{m_j}{\mathcal{K}_{\Gamma_{k(\boldsymbol{r}_i)}}} \Big(v_{j,\beta} - v_{\Gamma_{k(\boldsymbol{r}_i)},\beta}\Big)\Big(v_{i,\alpha} - v_{\Gamma_{k(\boldsymbol{r}_i)},\alpha}\Big)\Bigg],
\end{aligned} \tag{A.15}$$

where $\delta_{i,j}$ is the Kronecka delta. The final result, Eq. (2.20), is then recovered by substituting the derivative in Eq. (A.14) with the expression above.

Appendix B

Electrostatics

B.1 One-dimensional kernels

B.1.1 Wolf method

Our goal is to integrate G_{W} over the entire cutoff sphere in order to obtain $G_{\mathrm{1D,W}}$. To this end we have to evaluate the integral

$$G_{\mathrm{1D,W}}(z) = \int_{-\frac{L_x}{2}}^{\frac{L_x}{2}} \mathrm{d}x \int_{-\frac{L_y}{2}}^{\frac{L_y}{2}} \mathrm{d}y \; G_{\mathrm{W}}(x,y,z) \tag{B.1a}$$

$$= 2\pi \int_0^{s_{\mathrm{c}}(z)} \mathrm{d}s \; s \left[\frac{\operatorname{erfc}(\zeta\sqrt{s^2+z^2})}{\sqrt{s^2+z^2}} - \frac{\operatorname{erfc}(\zeta r_{\mathrm{c}})}{r_{\mathrm{c}}} \right], \tag{B.1b}$$

where $r^2 = x^2 + y^2 + z^2 = s^2 + z^2$. We first consider the integral

$$I(z) = \int_0^{s_{\mathrm{c}}(z)} \mathrm{d}s \; s \frac{\operatorname{erfc}(\zeta\sqrt{s^2+z^2})}{\sqrt{s^2+z^2}} \tag{B.2}$$

and use the substitution $\tau(s,z) = \sqrt{s^2+z^2}$ to rewrite the expression as

$$I(z) = \int_{\tau(0,z)}^{\tau(s_{\mathrm{c}}(z),z)} \mathrm{d}\tau \; \operatorname{erfc}(\zeta\tau). \tag{B.3}$$

Using integration by parts it is easy to show that the result is

$$I(z) = r_\mathrm{c}\,\mathrm{erfc}(\zeta r_\mathrm{c}) - |z|\,\mathrm{erfc}(\zeta|z|) + \frac{\mathrm{e}^{-\zeta^2 z^2} - \mathrm{e}^{-\zeta^2 r_\mathrm{c}^2}}{\sqrt{\pi}\zeta} \tag{B.4}$$

for $|z| \leq r_\mathrm{c}$ and zero otherwise. The integration of the second term in Eq. (B.1b) is trivial and the averaged kernel is given by

$$\begin{aligned}\frac{G_\mathrm{1D,W}(z)}{2\pi} = \quad & \frac{r_\mathrm{c}}{2}\,\mathrm{erfc}(\zeta r_\mathrm{c}) - |z|\,\mathrm{erfc}(\zeta|z|) \\ & + \frac{\mathrm{e}^{-\zeta^2 z^2} - \mathrm{e}^{-\zeta^2 r_\mathrm{c}^2}}{\sqrt{\pi}\zeta} + \frac{z^2\,\mathrm{erfc}(\zeta r_\mathrm{c})}{2r_\mathrm{c}}\end{aligned} \tag{B.5}$$

for $|z| \leq r_\mathrm{c}$ and it vanishes otherwise. The first three derivatives of this function are

$$\frac{G'_\mathrm{1D,W}(z)}{2\pi} = -\,\mathrm{sgn}(z)\,\mathrm{erfc}(\zeta|z|) + \frac{z\,\mathrm{erfc}(\zeta r_\mathrm{c})}{r_\mathrm{c}}, \tag{B.6a}$$

$$\begin{aligned}\frac{G''_\mathrm{1D,W}(z)}{2\pi} = & -2\delta(z)\,\mathrm{erfc}(\zeta|z|) \\ & + \frac{2\zeta}{\sqrt{\pi}}\,\mathrm{sgn}(z)^2\mathrm{e}^{-\zeta^2 z^2} + \frac{\mathrm{erfc}(\zeta r_\mathrm{c})}{r_\mathrm{c}},\end{aligned} \tag{B.6b}$$

$$\begin{aligned}\frac{G'''_\mathrm{1D,W}(z)}{2\pi} = & -2\delta'(z)\,\mathrm{erfc}(\zeta|z|) \\ & + \frac{2\zeta}{\sqrt{\pi}}\,\mathrm{sgn}(z)\mathrm{e}^{-\zeta^2 z^2}\Big[-2\zeta^2|z| + 6\delta(z)\Big],\end{aligned} \tag{B.6c}$$

respectively.

B.1.2 Ewald summation

Instead of integrating the kernel G_E (Eq. (3.11)) directly, we replace it by G_PBC (Eq. (3.9)) in order to simplify the problem. The sum in Eq. (3.9) is only conditionally convergent, which is why we are formally not allowed to change the order of integration and summation. However, if we ignore this fact we arrive at the same result that we

would have obtained by considering G_{E} directly. This yields

$$G_{\mathrm{1D,E}}(z) = \int_{-\frac{L_x}{2}}^{\frac{L_x}{2}} \mathrm{d}x \int_{-\frac{L_y}{2}}^{\frac{L_y}{2}} \mathrm{d}y \; G_{\mathrm{PBC}}(x,y,z) \tag{B.7a}$$

$$= \int_{-\frac{L_x}{2}}^{\frac{L_x}{2}} \mathrm{d}x \int_{-\frac{L_y}{2}}^{\frac{L_y}{2}} \mathrm{d}y \frac{1}{L_x L_y L_z} \sum_{\boldsymbol{k}\neq\boldsymbol{0}} \frac{4\pi}{k^2} \mathrm{e}^{i\boldsymbol{k}\cdot\boldsymbol{r}} \tag{B.7b}$$

$$= \frac{1}{L_z} \sum_{k_z\neq 0} \frac{4\pi}{k_z^2} \mathrm{e}^{ik_z z}. \tag{B.7c}$$

In the last step, we make use of the fact that the integration eliminates all terms in the summation for which $k_x \neq 0$ or $k_y \neq 0$. The inverse Fourier transform in Eq. (B.7c) is

$$G_{\mathrm{1D,E}}(z) = 2\pi \left(-|z| + \frac{z^2}{L_z} + \frac{L_z}{6} \right) \tag{B.8}$$

and the first three derivatives of this expression are given by

$$G'_{\mathrm{1D,E}}(z) = 2\pi \left(-\operatorname{sgn}(z) + \frac{2z}{L_z} \right), \tag{B.9a}$$

$$G''_{\mathrm{1D,E}}(z) = 2\pi \left(-2\delta(z) + \frac{2}{L_z} \right), \tag{B.9b}$$

$$G'''_{\mathrm{1D,E}}(z) = -4\pi\delta'(z), \tag{B.9c}$$

respectively.

B.2 Exact averaging

The aim is to average the one-dimensional kernel analytically for any bin j of width $\Delta z = z_{j,2} - z_{j,1}$ to obtain

$$\bar{G}_{\mathrm{1D},j}(z') = \frac{1}{\Delta z} \int_{z_{j,1}}^{z_{j,2}} \mathrm{d}z \; G_{\mathrm{1D}}(z - z') \tag{B.10}$$

taking into account the periodicity. As mentioned in Sec. 3.2, in our notation we understand the argument $z - z'$ to be mapped back to the interval $[-\frac{L_z}{2}, \frac{L_z}{2}]$ implicitly. The interesting case, where the separation of the charge at z' and the bin covering

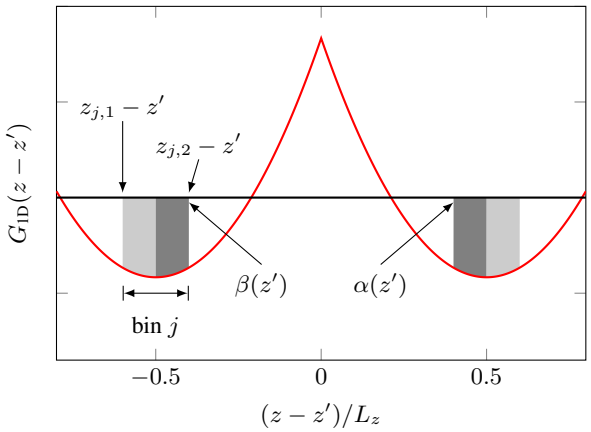

Figure B.1: Integration of the spatially averaged kernel for the case where the separation of the charge at z' and the bin j covering the interval $[z_{j,1}, z_{j,2}]$ is such that periodicity has to be taken into account. $\alpha_j(z')$ and $\beta_j(z')$ are the nearest images of the bin boundaries.

the interval $[z_{j,1}, z_{j,2}]$ is such that periodicity has to be taken into account in the integration, is illustrated in Fig. B.1.

The first step is to map the distances from z' to the bin boundaries back into the reference interval using the function

$$\mathrm{pbc}(z) = z - L_z \,\mathrm{round}\left(\frac{z}{L_z}\right), \tag{B.11}$$

where round(z) gives the nearest integral number to z. Applying this function yields the shortest distances to the nearest images which we label with

$$\alpha_j(z') = \mathrm{pbc}(z_{j,1} - z'), \tag{B.12a}$$
$$\beta_j(z') = \mathrm{pbc}(z_{j,2} - z'), \tag{B.12b}$$

respectively. For the case shown in Fig. B.1, where $\beta_j(z') < \alpha_j(z')$, we can split the original expression into the two integrals

$$\bar{G}_{1\mathrm{D},j}(z') = \frac{1}{\Delta z}\left[\int_{-\frac{L_z}{2}}^{\beta_j(z')} \mathrm{d}z\; G_{1\mathrm{D}}(z) + \int_{\alpha_j(z')}^{\frac{L_z}{2}} \mathrm{d}z\; G_{1\mathrm{D}}(z)\right]. \tag{B.13}$$

In order to simplify the integration further, we focus on the case of Ewald summation. Application of the procedure to the Wolf method is omitted for brevity, because the integration is tedious. We know that the average of $G_{1\mathrm{D,E}}$ over the reference interval vanishes because the term corresponding to $k_z = 0$ in Eq. (B.7c) is absent. Therefore,

the special case shown in Fig. B.1 reduces to the ordinary case

$$\bar{G}_{\mathrm{1D,E},j}(z') = \frac{1}{\Delta z} \int\limits_{\alpha_j(z')}^{\beta_j(z')} \mathrm{d}z \; G_{\mathrm{1D,E}}(z), \tag{B.14}$$

in which the entire bin is located inside the reference box. All possible scenarios are therefore taken into account by straightforward integration of Eq. (B.8), which yields

$$\begin{aligned} \frac{\bar{G}_{\mathrm{1D,E},j}(z')}{2\pi} = & \quad \frac{\alpha_j(z')|\alpha_j(z')| - \beta_j(z')|\beta_j(z')|}{2\Delta z} \\ & + \frac{\beta_j^3(z') - \alpha_j^3(z')}{3L_z\Delta z} \\ & + \frac{L_z\big(\beta_j(z') - \alpha_j(z')\big)}{6\Delta z}. \end{aligned} \tag{B.15}$$

Likewise, we find

$$\frac{\bar{G}'_{\mathrm{1D,E},j}(z')}{2\pi} = \frac{|\alpha_j(z')| - |\beta_j(z')|}{\Delta z} + \frac{\beta_j^2(z') - \alpha_j^2(z')}{\Delta z L_z} \tag{B.16}$$

for the average of the derivative. Equations (B.15) and (B.16) along with Eqs (B.12a–b) can be substituted into Eqs (3.19) and (3.20) to calculate the exact averages of the potential and the field, respectively.

B.3 Validation

In this section, we compare the oxygen-oxygen pair correlation function, $g(r)$, the oxygen-oxygen velocity autocorrelation function, VACF(t), a cumulative estimate of the dielectric constant, $\epsilon(t)$, and the distance-dependent Kirkwood g-factor, $G_{\mathrm{K}}(r)$. We refer to Refs 7 and 118 for a detailed discussion and the relevant formulae. All quantities were sampled during 2 ns *NVE* simulations before imposing the temperature gradients.

The results are shown in Figs B.2a–d. As we can see, all sets of parameters lead to excellent agreement for $g(r)$ and VACF(t) (Figs B.2a–b). The dielectric constant (Fig. B.2c) is well reproduced by the Wolf method with strong damping, whereas weak damping leads to an overestimation. More insight about the structural properties can be gained by looking at $G_{\mathrm{K}}(r)$ in Fig. B.2d. For very short distances both sets of parameters for the Wolf method yield a good agreement with Ewald summation. We note that for the weak damping the agreement extends a bit further than for strong damping, which is consistent with our observations for the model

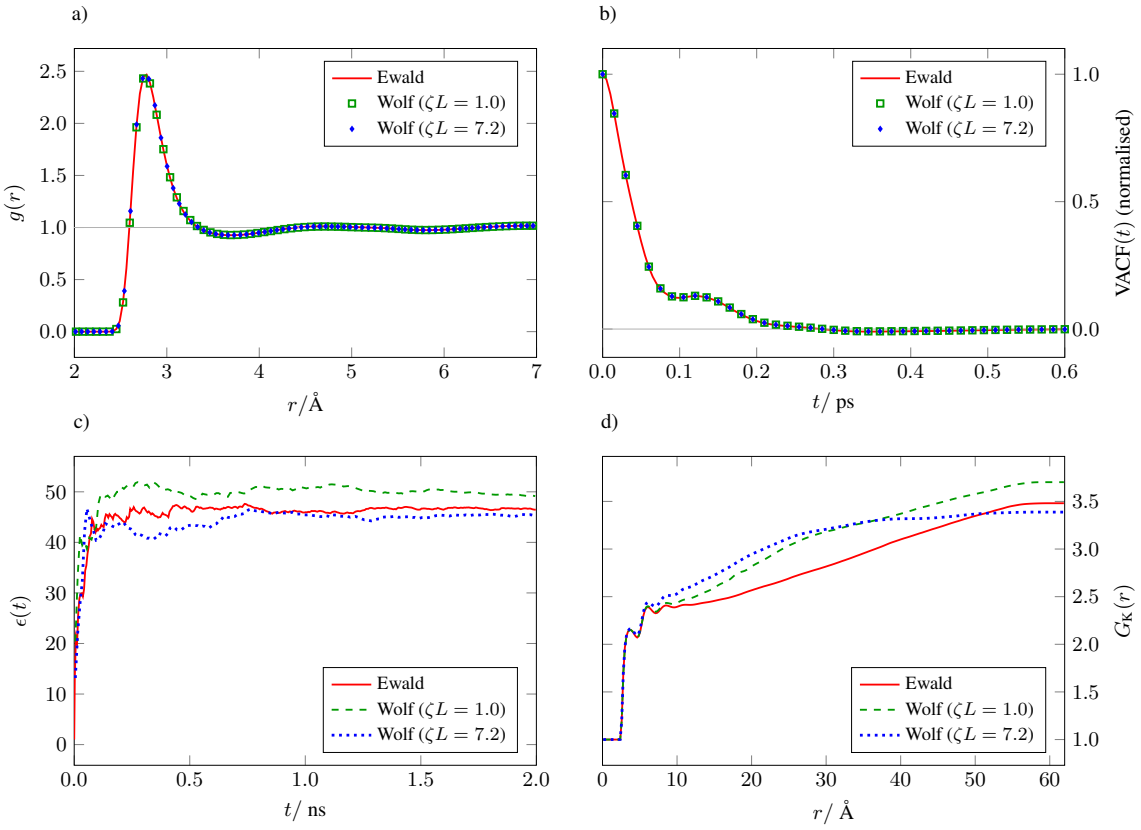

Figure B.2: The comparison comprises (a) the oxygen-oxygen pair correlation function, (b) the oxygen-oxygen VACF, (c) a cumulative estimate of the dielectric constant and (d) the distance-dependent Kirkwood g-factor.

system. We also note that the shape of $G_{\mathrm{K}}(r)$ looks different for our elongated box compared to a cubic box.

B.4 Mechanical equilibrium

In this section, we show that the average acceleration vanishes in the regions outside the reservoirs (mechanical equilibrium)[3]. To this end, we measured the spatial variation of the pressure tensor, as implemented in LAMMPS (version 9Dec14), along the direction of the temperature gradient. We note that an exhaustive investigation of this topic is outside the scope of this demonstration and refer to other literature for details on derivation and computation of the pressure. In particular, Ref. 119 explains how the virial contribution to the pressure can be evaluated in terms of forces acting on atoms. A derivation of the long-range contribution to the pressure for Ewald summation is given in Ref. 120, its decomposition using the Harasima path is summarised in Ref. 121, and an extension to PPPM is provided in Ref. 122.

The results for Ewald summation are shown in Fig. B.3. We only present the

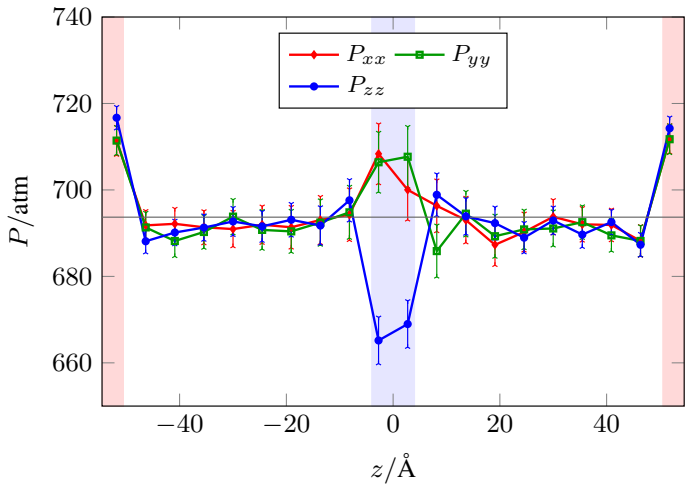

Figure B.3: Comparison of the diagonal components of the pressure tensor for Ewald summation. The horizontal line corresponds to the box average of the trace.

diagonal components of the pressure tensor because the off-diagonal ones are negligible on this scale. We can clearly see that all three components change significantly within the reservoirs. Although we have not investigated this behaviour further, we think that it may be related to discontinuities created by the thermostat. More importantly, however, the component P_{zz} exhibiting the largest variation changes only by approximately 1% outside the reservoirs. In atomistic simulations, pressure differences on this scale are typically considered small and we do not expect them to have a significant effect on the results. We therefore conclude that mechanical equilibrium holds reasonably well in the regions of interest.

Appendix C

Monopoles

C.1 Analytical model for the field

In this section we derive the analytical model proposed in Eq. (4.5). To this end, we first show how the spatial average of the three-dimensional field, $\langle E_z(z) \rangle$, calculated from the full charge density, $\rho(\boldsymbol{r})$, is related to the one-dimensional field, $E_{1\mathrm{D}}(z)$, calculated from the spatially averaged charge density, $\rho_{1\mathrm{D}}(z)$. The subscript $_{\mathrm{TP}}$ used in the main text is dropped for notational convenience. We consider PBCs and understand that this is implicitly taken into account whenever an expression of the form $\boldsymbol{r} - \tilde{\boldsymbol{r}}$ is evaluated.

For an arbitrary charge distribution, the field can be calculated as

$$\boldsymbol{E}(\boldsymbol{r}) = -\kappa \nabla_{\boldsymbol{r}} \int_{\Omega} \mathrm{d}^3\tilde{r}\; G(\boldsymbol{r} - \tilde{\boldsymbol{r}}) \rho(\tilde{\boldsymbol{r}}), \tag{C.1}$$

where $\kappa = (4\pi\epsilon_0)^{-1}$ with ϵ_0 being the vacuum permittivity, $\nabla_{\boldsymbol{r}} = (\partial_x, \partial_y, \partial_z)$ is the gradient in Cartesian coordinates, Ω denotes the orthogonal simulation box of volume $V = L_x L_y L_z$ and $G(\boldsymbol{r} - \tilde{\boldsymbol{r}})$ is a modified kernel that takes into account periodicity[36]. Averaging the z-component of the field over planes perpendicular to the z-axis yields[36,104]

$$\langle E_z(z)\rangle = \frac{1}{L_x L_y}\int_{-\frac{L_x}{2}}^{\frac{L_x}{2}}\int_{-\frac{L_y}{2}}^{\frac{L_y}{2}} \mathrm{d}x\mathrm{d}y\; E_z(\boldsymbol{r}) \tag{C.2a}$$

$$= -\kappa\frac{\partial}{\partial z}\int_{-\frac{L_z}{2}}^{\frac{L_z}{2}} \mathrm{d}\tilde{z}\; \underbrace{\frac{1}{L_x L_y}\int_{-\frac{L_x}{2}}^{\frac{L_x}{2}}\int_{-\frac{L_y}{2}}^{\frac{L_y}{2}} \mathrm{d}\tilde{x}\mathrm{d}\tilde{y}\; \rho(\tilde{\boldsymbol{r}})}_{=\,\rho_{1\mathrm{D}}(\tilde{z})} \underbrace{\int_{-\frac{L_x}{2}}^{\frac{L_x}{2}}\int_{-\frac{L_y}{2}}^{\frac{L_y}{2}} \mathrm{d}x\mathrm{d}y\; G(\boldsymbol{r}-\tilde{\boldsymbol{r}})}_{=\,G_{1\mathrm{D}}(z-\tilde{z})} \tag{C.2b}$$

$$= -\kappa\int_{-\frac{L_z}{2}}^{\frac{L_z}{2}} \mathrm{d}\tilde{z}\; G'_{1\mathrm{D}}(z-\tilde{z})\rho_{1\mathrm{D}}(\tilde{z}) \tag{C.2c}$$

$$= \frac{1}{\epsilon_0}\int_{-\frac{L_z}{2}}^{z} \mathrm{d}\tilde{z}\; \rho_{1\mathrm{D}}(\tilde{z}) + \frac{1}{\epsilon_0}\underbrace{\frac{1}{L_z}\int_{-\frac{L_z}{2}}^{\frac{L_z}{2}} \mathrm{d}\tilde{z}\; \tilde{z}\rho_{1\mathrm{D}}(\tilde{z})}_{=P_z} \tag{C.2d}$$

$$= E_{1\mathrm{D}}(z), \tag{C.2e}$$

where

$$G_{1\mathrm{D}}(z) = 2\pi\left[-|z| + \frac{z^2}{L_z} + \frac{L_z}{6}\right] \tag{C.3}$$

is the spatially averaged kernel for PBCs and P_z the z-component of the average box dipole density.

Next, we work out the averaged charge density and compute the field from Eq. (C.2d). The colloids are modelled by two homogeneously charged, spherical shells of radius R (in the main text we refer to this quantity as R_{TP}). Since all equations involved are linear, we can decompose the problem and focus on a single colloid. If we centre the charge distribution of this colloid around the origin, we can formulate the charge density as

$$\rho^{(1)}(\boldsymbol{r}) = \frac{q}{4\pi R^2}\delta(r-R), \tag{C.4}$$

where $q = \int_\Omega \mathrm{d}^3 r \rho^{(1)}(\boldsymbol{r})$ is the total charge, r the distance from the origin and $\delta(r-R)$ the Dirac delta function. Let us assume that $2R < L_x = L_y \leq L_z$ such that the charge distribution is fully contained within the reference box. We then have the

freedom to integrate over the largest inscribed cylinder and obtain

$$\rho_{\mathrm{1D}}^{(1)}(z) = \frac{1}{L_x L_y} \int_{-\frac{L_x}{2}}^{\frac{L_x}{2}} \int_{-\frac{L_y}{2}}^{\frac{L_y}{2}} \mathrm{d}x\mathrm{d}y \; \rho^{(1)}(\boldsymbol{r}) \tag{C.5a}$$

$$= \frac{q}{2R^2 L_x L_y} \int_0^{L_x/2} s\mathrm{d}s \; \delta\left(\sqrt{s^2+z^2} - R\right), \tag{C.5b}$$

where $r = \sqrt{s^2+z^2}$. Employing a second transformation, $\tau = \sqrt{s^2+z^2}$ with $s\mathrm{d}s = \tau\mathrm{d}\tau$, it is straightforward to solve the above integral to find

$$\rho_{\mathrm{1D}}^{(1)}(z) = \begin{cases} \frac{q}{2RA} & \text{if } |z| < R, \\ 0 & \text{otherwise,} \end{cases} \tag{C.6}$$

where $A = L_x L_y$ is the cross-sectional area. The averaged charge density taking into account both colloids centred around z_{h} and z_{c}, respectively, is therefore given by the piecewise constant function

$$\rho_{\mathrm{1D}}(z) = \frac{q}{2RA} \begin{cases} +1 & \text{if } |z - z_{\mathrm{h}}| < R, \\ -1 & \text{if } |z - z_{\mathrm{c}}| < R, \\ 0 & \text{otherwise.} \end{cases} \tag{C.7}$$

If we plug this result into Eq. (C.2d) and carry out the integration, we obtain the final result

$$\frac{\langle E_z(z) \rangle}{\tilde{E}} = \begin{cases} -1 & \text{if } |z| > z_{\mathrm{c}} + R, \\ +1 & \text{if } |z| < z_{\mathrm{c}} - R, \\ (z - z_{\mathrm{h}})/R & \text{if } |z - z_{\mathrm{h}}| \leq R, \\ (z_{\mathrm{c}} - z)/R & \text{otherwise,} \end{cases} \tag{C.8}$$

where $\tilde{E} = q/(2\epsilon_0 A)$ is the constant field value for the region between the two colloids.

The quantity $\tilde{E}$ can be understood easily by applying Gauss's theorem to the blue control volume shown in Fig. C.1. The charge q in the centre represents the thermally induced charge of the hot colloid. Let us denote the surface of this volume by $\partial\Gamma$, the union of the two faces highlighted in blue by $\partial\Gamma_{\parallel}$, and the union of the remaining faces by $\partial\Gamma_{\perp}$. According to Gauss's theorem the total charge enclosed by

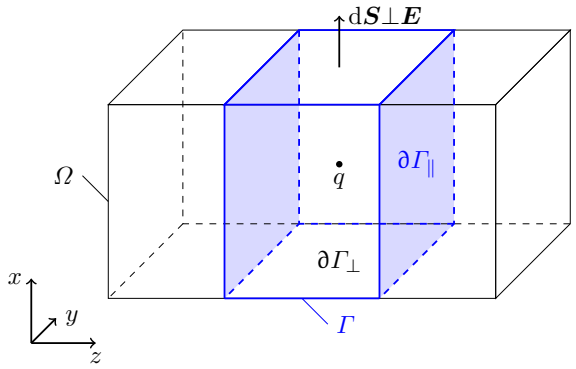

Figure C.1: Application of Gauss's theorem. Illustration of the simulation box Ω containing a charge q located at the centre of a control volume Γ (solid and dashed blue lines) to which we apply Gauss's theorem. For the two faces of Γ denoted by $\partial\Gamma_\parallel$ (highlighted in blue) the field $\boldsymbol{E}$ has a contribution parallel to the surface normal vector $\mathrm{d}\boldsymbol{S}$, whereas it is orthogonal to it on all other faces denoted by $\partial\Gamma_\perp$.

$\partial\Gamma$ is related to the field flux through $\partial\Gamma$ such that

$$\oiint_{\partial\Gamma} \boldsymbol{E}(\boldsymbol{r}) \cdot \mathrm{d}\boldsymbol{S} = \frac{q}{\epsilon_0}, \tag{C.9}$$

where $\mathrm{d}\boldsymbol{S}$ is the surface normal vector. If we decompose the surface integral and recall that the surface normal vector is perpendicular to the field on $\partial\Gamma_\perp$ due to the periodic setup, we find

$$\oiint_{\partial\Gamma} \boldsymbol{E}(\boldsymbol{r}) \cdot \mathrm{d}\boldsymbol{S} = \iint_{\partial\Gamma_\parallel} \boldsymbol{E}(\boldsymbol{r}) \cdot \mathrm{d}\boldsymbol{S} + \underbrace{\iint_{\partial\Gamma_\perp} \boldsymbol{E}(\boldsymbol{r}) \cdot \mathrm{d}\boldsymbol{S}}_{=0} = \langle E_{z,\parallel} \rangle 2A = \frac{q}{\epsilon_0}. \tag{C.10}$$

Rearranging terms, we find

$$\tilde{E} = \langle E_{z,\parallel} \rangle = \frac{q}{2\epsilon_0 A}, \tag{C.11}$$

which is our final result.

We note that the value of $\tilde{E}$ is constant and does not change if we move the surfaces $\partial\Gamma_\parallel$ along the z-axis as long as they enclose the charge entirely. Finally, we note that the presence of the opposite charge $-q$ is already taken into account implicitly, which is indicated by the multiplication by twice the cross-sectional area A in Eq. (C.10). Equivalently, we can think of the result as the sum of two equal contributions, half from the charge q and the other half from $-q$.

C.2 Off-centre Stockmayer model

Displacing the LJ centre from the location of the point dipole leads to modified forces and torques compared to the original Stockmayer model[110]. We note that electrostatic contributions are not affected by this modification and refer to Ref. 123 for the relevant expressions. All modifications of short-ranged interactions related to the perturbation of the LJ centre are governed by a single parameter α and summarised in this section.

Let us consider the short-ranged, pairwise interactions between two solvent particles as illustrated in Fig. C.2. The point dipoles are located at the positions $\boldsymbol{r}_i$ and $\boldsymbol{r}_j$, respectively. The mass of a particle ($m^* = 1$) is distributed homogeneously over a ball of radius $R_I = \sigma/2$ such that the moment of inertia is given by $I = 2mR_I^2/5$, which corresponds to $I^* = 0.1$ in reduced units. The LJ centre is denoted by $\boldsymbol{\xi}$ and displaced from the position of the dipole by a vector $\Delta\boldsymbol{r} = \boldsymbol{\xi} - \boldsymbol{r} = \alpha\hat{\boldsymbol{\mu}}$, where $\hat{\boldsymbol{\mu}}$ is the unit vector of the dipole moment $\boldsymbol{\mu}$. The quantity α allows us to control the level of asymmetry, i.e. the perturbation to the original Stockmayer model, and we employed a value of $\alpha = -\sigma/4$ in all our simulations.

We recall that the radially symmetric, pairwise LJ potential is given by

$$u(r) = 4\varepsilon\left[\left(\frac{\sigma}{r}\right)^{12} - \left(\frac{\sigma}{r}\right)^{6}\right], \tag{C.12}$$

where ε is the unit of energy. For performance reasons, we employed a cutoff of $r_\mathrm{c} = 8\sigma$ for all short-ranged interactions based on the centre of mass separation $\boldsymbol{r}_{ij} = \boldsymbol{r}_j - \boldsymbol{r}_i$. The energy contribution for the two particles shown in Fig. C.2 is therefore given by $u_{ij} = u(\xi_{ij})\Theta(r_\mathrm{c} - r_{ij})$, where $\Theta(r)$ is the Heaviside function and $\boldsymbol{\xi}_{ij} = \boldsymbol{\xi}_j - \boldsymbol{\xi}_i$.

Taking the negative gradient of the energy with respect to $\boldsymbol{\xi}_i$ and applying a

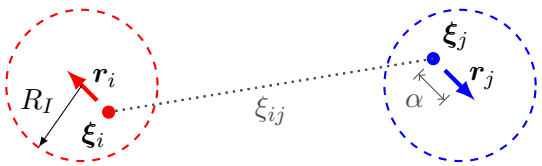

Figure C.2: Off-centre Stockmayer model. Two solvent particles with dipoles (coloured arrows) located at $\boldsymbol{r}_i$ and $\boldsymbol{r}_j$, respectively, and displaced LJ centres, $\boldsymbol{\xi}_i$ and $\boldsymbol{\xi}_j$, separated by a distance of ξ_{ij}. The mass of a solvent particle is distributed homogeneously over a ball of radius R_I, as illustrated by the dashed circles. The asymmetry in the short-ranged interactions, compared to the Stockmayer model, is controlled by the parameter α.

cutoff, we obtain the force

$$\boldsymbol{f}_{ij} = \Theta(r_{\mathrm{c}} - r_{ij}) 24\sigma\varepsilon \left[\left(\frac{\sigma}{\xi_{ij}} \right)^6 - 2 \left(\frac{\sigma}{\xi_{ij}} \right)^{12} \right] \frac{\boldsymbol{\xi}_{ij}}{\xi_{ij}^2} \tag{C.13}$$

acting on particle i with the corresponding force $\boldsymbol{f}_{ji} = -\boldsymbol{f}_{ij}$ acting on particle j. The short-ranged contributions to the torques acting on these particles are then simply given by

$$\boldsymbol{\tau}_{ij} = \alpha \hat{\boldsymbol{\mu}}_i \times \boldsymbol{f}_{ij} \tag{C.14}$$

and

$$\boldsymbol{\tau}_{ji} = \alpha \hat{\boldsymbol{\mu}}_j \times \boldsymbol{f}_{ji}, \tag{C.15}$$

respectively, where $\times$ denotes the cross product between two vectors. In the limit $\alpha \to 0$ these torque contributions vanish such that we recover the original Stockmayer model.

C.3 Statistical accuracy

The size of each error bar in Fig. 4.2C represents twice the standard deviation of the mean value which was calculated as the difference between the non-equilibrium and the equilibrium averages. For the individual production run we computed field averages according to the following protocol: at regular time intervals of $\delta t = 50\Delta t$ we computed $\langle E_{z,\mathrm{TP}}(z) \rangle$ according to Eq. (4.6), excluding dipoles within a distance of R_{TP} from the colloid centres. We then averaged $\langle E_{z,\mathrm{TP}}(z) \rangle$ over slabs of width $\Delta z = L/24$ which are centred around the points $z_i = -L/2 + (i - 1/2)\Delta z$, where $i = 1, \ldots, 24$. The resulting instantaneous spatial averages are denoted by E_i^m, where $m = 1, \ldots, M$ indexes the simulation time according to $t^m = m\delta t$ and $M = 1.5 \times 10^6$ is the total number of configurations considered. From the resulting time series $\{E_i^1, \ldots, E_i^M\}$ we computed the mean value, $\bar{E}_i$, for each bin and estimated its standard deviation, $\bar{\sigma}_i$, using block average analysis. Errors for the final results $\bar{E}_{i,\mathrm{TP}} = \bar{E}_{i,\mathrm{NEMD}} - \bar{E}_{i,NVE}$ shown in the plot were calculated as the square root of the total variance $\bar{\sigma}^2_{i,\mathrm{NEMD}} + \bar{\sigma}^2_{i,NVE}$, assuming that the production runs were statistically independent. The quantity $\tilde{E}$, appearing in Eq. (4.5), was computed from the slabs with index $j \in \{1, 2, 11, 12, 13, 14, 23, 24\}$ using the relation $\tilde{E} = -1/8 \sum_j |\bar{E}_{j,\mathrm{TP}}|$. These slabs correspond to the region of constant average field between the colloids. Errors were propagated assuming that the terms in the sum are statistically independent such that the error $\sigma_{\tilde{E}}$ is given by the square root of $1/8 \sum_j \bar{\sigma}^2_{j,\mathrm{TP}}$. The estimate of q_{TP} follows from multiplication of $\tilde{E}$ by the

constant factor $2A\epsilon_0$. The error bar for the estimate of q_{TP} obtained with Eq. (4.4) is omitted since we do not have error estimates for the temperature contour lines shown in Fig. 4.1A. The computation of S_{TP} involves additional simulation data and is explained in Appendix C.4.

C.4 Estimation of S_{TP}

We estimated the thermo-polarisation coefficient using the relation

$$S_{\mathrm{TP}}(z) = \frac{\langle E_{z,\mathrm{TP}}(z)\rangle}{\partial_z \langle T(z)\rangle}, \tag{C.16}$$

where $\partial_z\langle T(z)\rangle$ denotes the gradient of the temperature averaged over planes perpendicular to the z-axis (see Fig. C.3).

The simulation data reveals a perfectly linear profile in the vicinity of the origin, such that $\beta \equiv \partial_z\langle T(z)\rangle$ is constant. We recall that the field value is $\tilde{E}$ in that region (see Fig. 4.2C), implying that S_{TP} is effectively a constant. Propagating the errors of $\tilde{E}^* = (-1.96 \pm 0.20) \times 10^{-3}$ and $\beta^* = (-9.09 \pm 0.03) \times 10^{-3}$ according to

$$\sigma_S = \frac{1}{|\beta|}\sqrt{\sigma_{\tilde{E}}^2 + S_{\mathrm{TP}}^2 \sigma_\beta^2}, \tag{C.17}$$

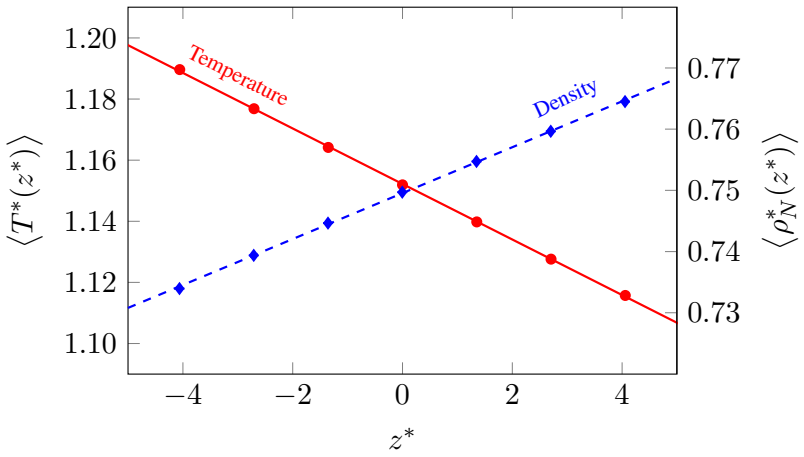

Figure C.3: Planar averages of temperature and density. Temperature (red circles) and solvent number density (blue diamonds) were averaged over slabs perpendicular to the z-axis in the vicinity of the origin. The width of each slab is $\Delta z^* = L^*/31$ and all error bars are smaller than the symbol sizes. To estimate errors of the linear fit coefficients for the interval shown in the plot, we first divided the NEMD trajectory into 1500 blocks and performed individual fits for each block average. We then calculated the mean values and standard deviations of the resulting coefficients using block average analysis. The results are $\langle T^*(z^*)\rangle = (-9.09 \pm 0.03) \times 10^{-3} z^* + (1.1522 \pm 0.0002)$ (solid red line) and $\langle \rho_N^*(z^*)\rangle = (3.76 \pm 0.02) \times 10^{-3} z^* + (0.74952 \pm 0.00005)$ (dashed blue line).

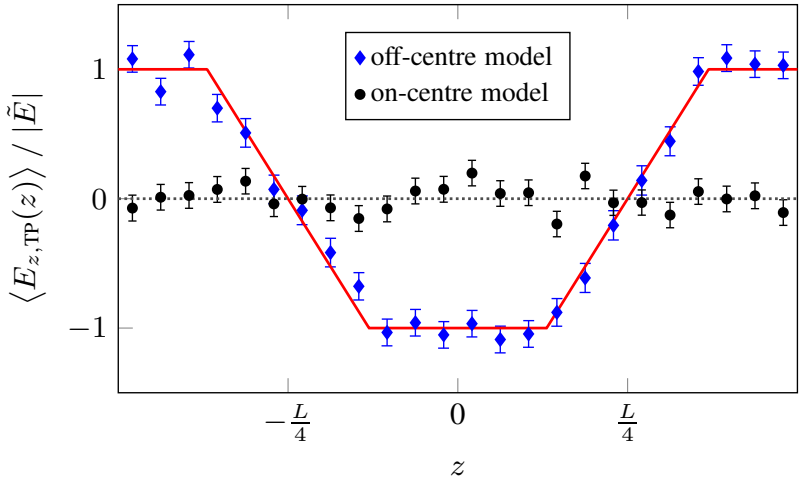

Figure C.4: Induced electric field for the off-centre and the on-centre Stockmayer model. The results for the on-centre model (black circles) are compared to the ones for the off-centre case (blue diamonds and solid red line) shown in Fig. 4.2C. The dotted horizontal line was added to guide the eye and to highlight the symmetry of the induced field.

we obtain an estimate of $S^*_{\mathrm{TP}} = 0.216 \pm 0.022$ for our model in the temperature and density regions shown in Fig. C.3.

C.5 Comparison with on-centre Stockmayer model

A microscopic theory that accounts for the alignment of off-centre Stockmayer particles in a thermal gradient is at present lacking, but recent studies on dumbbell molecules suggest that a shape or mass asymmetry is required for the effect[30,31,33]. In our model shape asymmetry is introduced by choosing a non-zero value for α (Fig. C.2). The thermo-molecular orientation is expected to vanish for the on-centre case where α is zero. To illustrate this behaviour, we carried out additional simulations with the on-centre Stockmayer model[110] following the same protocol as in the off-centre case, apart from minor differences in the thermostat settings ($\mathcal{F} = 49.58\epsilon/\tau$). The comparison of the induced electric field, shown in Fig. C.4, suggests that on-centre Stockmayer particles indeed do not align in a thermal gradient.

C.6 Comparison of temperature and electric potential

The results shown in Fig. 4.1 suggest that the electric field lines are aligned perpendicular to the temperature isosurfaces, implying that the electric field is parallel to the temperature gradient field. A direct quantitative comparison of the three-

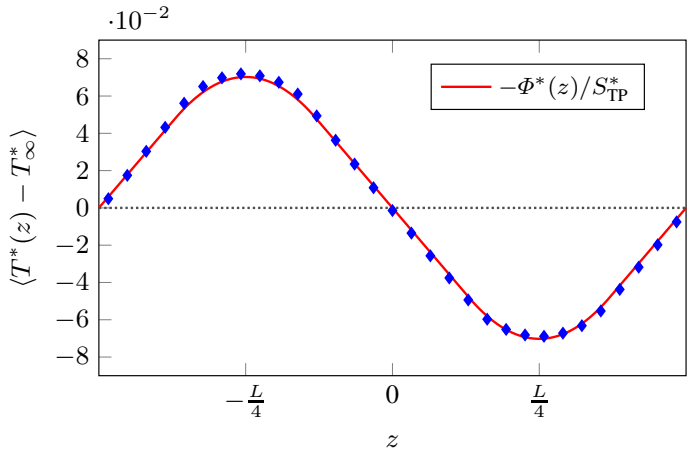

Figure C.5: Planar averages of temperature and electric potential. The temperature (blue diamonds) was averaged over slabs perpendicular to the z-axis and the bulk value T_∞ was subtracted for comparison with the averaged electric potential $\Phi(z)$ (red, solid line), which was computed according to Eq. (C.18) and normalised by $-S_{\mathrm{TP}}$. The dotted horizontal line is a guide to the eye and highlights the symmetry of both quantities. Uncertainties in the temperature values are smaller than the symbol size.

dimensional fields is difficult for the following reasons: Firstly, statistical fluctuations in the computed electric field are relatively large, which is why we considered planar averages in Fig. 4.2C. Secondly, computation of the temperature gradient field requires taking numerical derivatives of the simulation data thereby increasing the error. We therefore explore an alternative route and compare the averaged electric potential, $\langle \Phi(z) \rangle$, to the averaged temperature deviation from the bulk value, $\langle T(z) - T_\infty \rangle$. To facilitate the comparison, we integrate the analytical solution for the electric field [Eq. (4.5)], which we have already shown to be in good agreement with the simulation data (Fig. 4.2C), such that

$$\langle \Phi(z) \rangle = -\int_{-L/2}^{z} \langle E_z(z') \rangle \mathrm{d}z' = \frac{\tilde{E}L}{2} + \tilde{E} \times \begin{cases} z & \text{if } z < z_\mathrm{h} - R_{\mathrm{TP}}, \\ z_\mathrm{h} - R_{\mathrm{TP}}/2 - \frac{(z-z_h)^2}{2R_{\mathrm{TP}}} & \text{if } |z - z_\mathrm{h}| \leq R_{\mathrm{TP}}, \\ 2z_\mathrm{h} - z & \text{if } |z| < z_\mathrm{c} - R_{\mathrm{TP}}, \\ 2z_\mathrm{h} - z_\mathrm{c} + R_{\mathrm{TP}}/2 + \frac{(z-z_\mathrm{c})^2}{2R_{\mathrm{TP}}} & \text{if } |z - z_\mathrm{c}| \leq R_{\mathrm{TP}}, \\ 2(z_\mathrm{h} - z_\mathrm{c}) + z & \text{otherwise.} \end{cases} \tag{C.18}$$

The comparison of both quantities is shown in Fig. C.5 and reveals excellent agreement throughout the entire domain.

C.7 Estimate for water

An accurate estimate of the thermally induced charge for water would require additional simulations with a realistic model. We can, however, get a rough idea of the order of magnitude using an estimate of $S_{\mathrm{TP}} \approx 0.1$ mV/K for SPC/E water around room temperature[35,36]. Let us assume that the temperature gradient is sufficiently weak such that we are in the linear regime where $\boldsymbol{E} = S_{\mathrm{TP}} \nabla T$ holds and quadrupole contributions to the electric field can be neglected. For a spherical colloid of radius $R = 500$ nm which is heated by 20 K with respect to T_∞, we can then employ Eq. (4.4) to obtain an estimate of $q_{\mathrm{TP}} \approx 0.7 q_e$ for the thermally induced charge, where q_e is the charge of an electron.

Colloidal particles can also carry a charge due to the dissociation of ionisable groups at the surface[124]. For example, polystyrene spheres of radius $R = 66$ nm, in aqueous colloidal suspensions, were found to carry effective charges of almost $10^3 q_e$ which is much larger than the one we are trying to measure[124,125]. To single out the thermally induced charge, we therefore think that it would be better to consider sterically stabilised colloids that are, on average, uncharged and possibly use electrophoresis to select those particles that carry the least charge. It is, however, not immediately obvious which system would be a good model candidate to study.

Appendix D

Mean-field theory

D.1 Simulation details

We used the LAMMPS simulation package[54] (version 11Aug17) to perform all molecular dynamics simulations presented in this work. In all cases, we employed a fully periodic, prismatic simulation box with dimensions $3L_x = 3L_y = L_z \equiv L$ containing 5832 off-centre Stockmayer particles[37]. We set the cutoff radius to 7σ for all types of interaction and specified a relative accuracy of approximately 10^{-5} for the computation of long-range forces along with tin-foil boundary conditions[65,91,123].

To equilibrate our systems, we followed the protocol outlined in Ref. 37. We first generated a lattice structure with random dipole orientations and equilibrated it in an NVT-simulation for at least $2 \times 10^3\tau$, where $\tau = \sigma\sqrt{m/\varepsilon}$ is the unit of time. In NVT simulations, we set the relaxation time of the Nosé–Hoover thermostat[56,57] to 0.5τ. We employed a timestep of $\Delta t = 0.005\tau$ for the discrete time integration for the simulations corresponding to Fig. 5.2 and $\Delta t = 0.004\tau$ for the ones corresponding to Fig. 5.3. In $\nabla\rho$-runs, we employed a body force to each particle during this equilibration run in order to establish the desired density gradient. Subsequently, we performed the production run retaining this body force, and we sampled spatial profiles for temperature, density and molecular orientation. For ∇T-runs and full NEMD-runs, we adjusted velocities of the last configuration of the NVT simulation so that the total energy matched the average energy sampled[39]. We then equilibrated the system for another $2 \times 10^3\tau$ in an NVE simulation before imposing either a heat flux using the eHEX algorithm[39] or a temperature gradient by applying two Gaussian thermostats locally to adjust the non-translational kinetic energy inside the reservoirs appropriately. The former approach is suitable when imposing a constant heat flux (e.g. the results presented in Fig. 5.2), while the latter is better suited when a constant temperature gradient is desired (e.g. the results presented in Fig. 5.3).

We waited for at least $2 \times 10^3 \tau$ for a steady state to become fully established and for any transient behaviour to vanish before starting production runs. For ∇T-runs, we employed a body force both during the steady-state equilibration and in the production run in order to remove the density gradient. Production runs were simulated for between $1 \times 10^5 \tau$ and $5 \times 10^5 \tau$; we stopped simulations when the statistics for $\langle \cos\theta \rangle$ were sufficiently converged. Even for the longest simulation (the NEMD-run in Fig. 5.2), we did not observe any energy loss with the eHEX algorithm. As pointed out in Ref. 36, the piecewise constant profile for $\langle \cos\theta \rangle$ is established fairly quickly, but because there is no energetic penalty for having a net dipole moment with tinfoil boundary conditions, long simulation times may be required for $\langle \cos\theta \rangle$ to be centred around zero perfectly. Since the constant term $(1/L) \int_L \langle \cos\theta(z) \rangle \, \mathrm{d}z$ is very small and must vanish by symmetry for an infinitely long run, we are justified in subtracting it from the sampled profile $\langle \cos\theta(z) \rangle$ to reduce the computational cost.

Imposing a piecewise constant force proportional to $\mathrm{sgn}(z)\hat{\boldsymbol{z}}$ leads to a serious drift in the total energy in *NVE* simulations. We found this problem to be related to the discontinuity of the force at the origin when a piecewise constant force was applied. The problem was only observable in *NVE* simulations or in combination with the eHEX algorithm, because in all other cases the lost energy is re-supplied by the thermostat. To resolve it, we fitted third-order polynomials inside the reservoirs so that the resulting force profile was continuously differentiable. This procedure eliminated the energy drift completely.

D.2 Force derivation

In this section, we derive the analytical force expressions provided in Eqs (5.7)–(5.9). We start from the fundamental equation for the internal energy E,

$$\mathrm{d}E = T\,\mathrm{d}S - P\,\mathrm{d}V + F\,\mathrm{d}z + \mu\,\mathrm{d}N, \tag{D.1}$$

where S is the entropy, P the pressure, V the volume, F is a force acting on the system, μ the chemical potential and N the number of particles. The Gibbs energy is given by $G = E - TS + PV = \mu N$, so its total differential can be written as

$$\mathrm{d}G = F\,\mathrm{d}z + \mu\,\mathrm{d}N - S\,\mathrm{d}T + V\,\mathrm{d}P = N\,\mathrm{d}\mu + \mu\,\mathrm{d}N. \tag{D.2}$$

After division by N, we obtain the Gibbs–Duhem analogue

$$\mathrm{d}\mu = f\,\mathrm{d}z - s\,\mathrm{d}T + v\,\mathrm{d}P, \tag{D.3}$$

where $v = 1/\rho$. Since $\mu = \mu(T, \rho)$ and $P = P(T, \rho)$, we can write the total differentials of both functions as

$$\mathrm{d}\mu = \left(\frac{\partial\mu}{\partial\rho}\right)_T \mathrm{d}\rho + \left(\frac{\partial\mu}{\partial T}\right)_\rho \mathrm{d}T \tag{D.4}$$

and

$$\mathrm{d}P = \left(\frac{\partial P}{\partial T}\right)_\rho \mathrm{d}T + \left(\frac{\partial P}{\partial\rho}\right)_T \mathrm{d}\rho. \tag{D.5}$$

Temperature and density vary only with z and their total differentials are given by

$$\mathrm{d}\rho = \frac{\mathrm{d}\rho}{\mathrm{d}z}\,\mathrm{d}z \qquad \text{and} \qquad \mathrm{d}T = \frac{\mathrm{d}T}{\mathrm{d}z}\,\mathrm{d}z. \tag{D.6}$$

Combining Eqs (D.3)–(D.6) and comparing coefficients of the differentials, we find that the force per particle can be expressed as

$$\begin{aligned} f = &\underbrace{\left(\frac{\partial\mu}{\partial\rho}\right)_T \frac{\mathrm{d}\rho}{\mathrm{d}z} + \left[s + \left(\frac{\partial\mu}{\partial T}\right)_\rho\right]\frac{\mathrm{d}T}{\mathrm{d}z}}_{f_{\mathrm{ext}}} \\ &\underbrace{-\frac{1}{\rho}\left[\left(\frac{\partial P}{\partial T}\right)_\rho \frac{\mathrm{d}T}{\mathrm{d}z} + \left(\frac{\partial P}{\partial\rho}\right)_T \frac{\mathrm{d}\rho}{\mathrm{d}z}\right]}_{f_{\mathrm{balance}}}. \end{aligned} \tag{D.7}$$

The overall thermodynamic force acting on a particle vanishes at equilibrium, i.e. $f = 0$. If we identify the force f_{ext} as an externally applied force, at equilibrium, it must therefore be compensated exactly by the balancing force f_{balance}.

D.3 Ideal force

We can express the chemical potential as the sum of an ideal and an excess contribution, $\mu = \mu^{\mathrm{id}} + \mu^{\mathrm{ex}}$. This implies that we can also split the external force [Eq. (D.7)] into an ideal and an excess contribution,

$$f_{\mathrm{ext}} = f_{\mathrm{ext}}^{\mathrm{id}} + f_{\mathrm{ext}}^{\mathrm{ex}}. \tag{D.8}$$

Our goal in this section is to relate the ideal force $f_{\mathrm{ext}}^{\mathrm{id}}$ to the average force

experienced by a particle in simulation,

$$\langle f_i \rangle = \left\langle f_{\text{ext}} + \sum_j f_{ij} \right\rangle, \tag{D.9}$$

where f_{ij} is the pairwise force that is exerted on particle i by particle j. Because μ^{id} is derived from the kinetic term in the canonical partition function, and therefore also applies to an ideal gas, we cannot interpret $f_{\text{ext}}^{\text{id}}$ as the gradient of a potential energy. Therefore, $\langle \sum_j f_{ij} \rangle$ will only be able to balance the *excess* contribution of the external force, and

$$\langle f_i \rangle = f_{\text{ext}}^{\text{id}} = \left(\frac{\partial \mu^{\text{id}}}{\partial \rho} \right)_T \frac{\mathrm{d}\rho}{\mathrm{d}z} + \left[s^{\text{id}} + \left(\frac{\partial \mu^{\text{id}}}{\partial T} \right)_\rho \right] \frac{\mathrm{d}T}{\mathrm{d}z}. \tag{D.10}$$

We can straightforwardly evaluate the right-hand side of the above equation using the ideal chemical potential $\mu^{\text{id}} = k_{\text{B}} T \ln(\rho \Lambda^3)$, where Λ is the de Broglie thermal wavelength. The first term yields

$$\left(\frac{\partial \mu^{\text{id}}}{\partial \rho} \right)_T \frac{\mathrm{d}\rho}{\mathrm{d}z} = \frac{k_{\text{B}} T}{\rho} \frac{\mathrm{d}\rho}{\mathrm{d}z}. \tag{D.11}$$

For the second term, we also use the Sackur–Tetrode expression for the ideal entropy,

$$s^{\text{id}} = \frac{5 k_{\text{B}}}{2} - k_{\text{B}} \ln(\rho \Lambda^3), \tag{D.12}$$

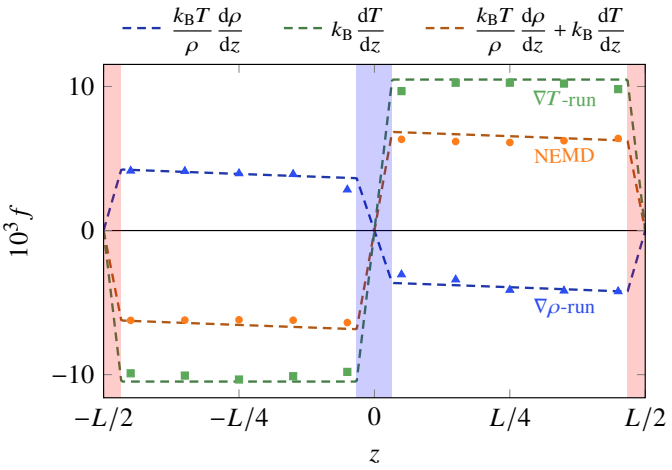

Figure D.1: Residual force measured in simulation (symbols) for the off-centre Stockmayer system with $p^2 = 1$ alongside the predicted ideal contributions from Eq. (D.14) (dashed lines). Symbols are larger than error bars.

and thus we can evaluate

$$s^{\mathrm{id}} + \left(\frac{\partial \mu^{\mathrm{id}}}{\partial T}\right)_{\rho} = k_{\mathrm{B}}, \tag{D.13}$$

giving an overall expression of

$$f_{\mathrm{ext}}^{\mathrm{id}} = \frac{k_{\mathrm{B}}T}{\rho}\frac{\mathrm{d}\rho}{\mathrm{d}z} + k_{\mathrm{B}}\frac{\mathrm{d}T}{\mathrm{d}z}. \tag{D.14}$$

In $\nabla\rho$-runs, the second term is zero, whilst in ∇T-runs, the first term is zero, giving the result we used in the main text. We note that, although our particles have orientational degrees of freedom, contributions to the ideal force due to ideal rotational motion evaluate to zero. Furthermore, $\langle f_i \rangle$ being non-zero does not imply a continual net acceleration of the particle, because this force is balanced by the ideal pressure $P^{\mathrm{id}} = \rho k_{\mathrm{B}} T$ [Eq. (D.7)].

To test Eq. (D.10) numerically, we sampled $\langle f_i \rangle$ during the production runs and compared it to the analytical expression [Eq. (D.14)], as shown in Fig. (D.1). We can see that the simulation results are in excellent agreement with the theoretical expression.

D.4 Supplemental figures

In this section, we present additional results supporting Fig. 5.3. As outlined in the main text, for $p^2 \geq 1$, we assigned half the temperature-gradient-induced ideal force to the centre of mass. To highlight the consequences of this physically motivated but to some extent arbitrary choice, we also present results for an alternative treatment in which the entire force acts on the LJ site (Fig. D.2). The ideal force only has a small effect on the results for $p^2 \geq 1$ (dotted lines), but splitting the force across the LJ and centre of mass sites yields better agreement with the simulation data (solid lines).

Figure D.3 shows the density and temperature profiles for the comparison in Fig. 5.3. We fixed the temperatures of the hot and cold slabs to match the temperature profiles in all NEMD- and ∇T-runs. The resulting density gradient increases with dipole strength. We note the onset of a non-linear behaviour for $p^2 = 3$. Numerical values for the density gradients are summarised in the table below.

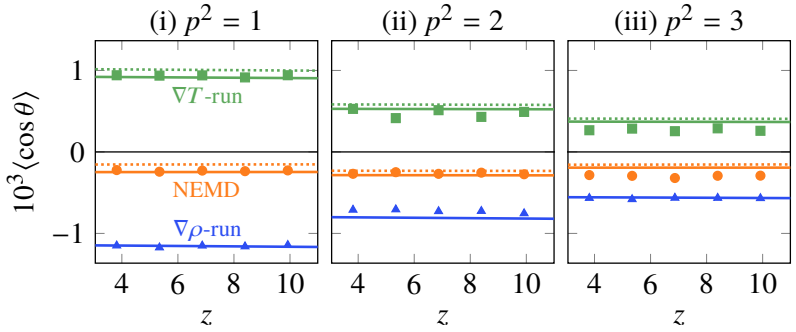

Figure D.2: Mean orientation for an off-centre Stockmayer liquid at varying dipole strength for an alternative choice of ideal attachment sites. Symbols represent simulation results and solid lines correspond to theoretical predictions as discussed in the main text. Dotted lines give an alternative set of theoretical predictions where the ideal balancing force acts entirely on the LJ site for the ∇T-runs.

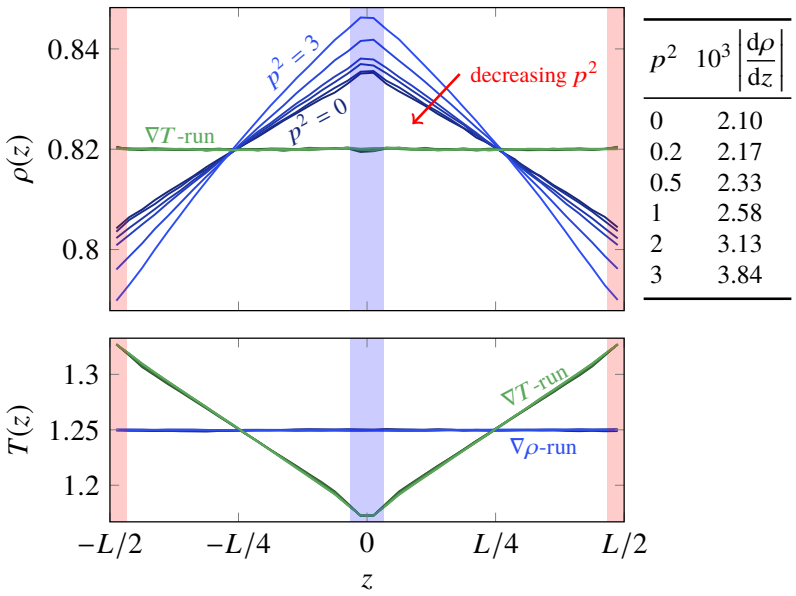

p^2	$10^3\left\lvert\frac{d\rho}{dz}\right\rvert$
0	2.10
0.2	2.17
0.5	2.33
1	2.58
2	3.13
3	3.84

Figure D.3: Density and temperature gradients for the off-centre Stockmayer system considered in the main text (with p^2 values of 0, 0.2, 0.5, 1, 2 and 3). The temperature gradients do not change as a function of p^2, but the density gradients do. The profiles become slightly non-linear for large dipole moments; the mean values of the absolute values of the density gradients are given. The mean temperature gradient is $|dT/dz| = 0.010$ for ∇T-runs at all values of p^2.

D.5 Pressure and chemical potential

In this section, we present additional simulation results for the pressure and the chemical potential. We first show that the Johnson EOS yields good analytical estimates for the pressure (Fig. D.4). The theoretical result was computed solely based on the temperature and density profiles and yields a very accurate prediction for the $\nabla\rho$- and ∇T-runs. However, we notice a small error in the prediction of

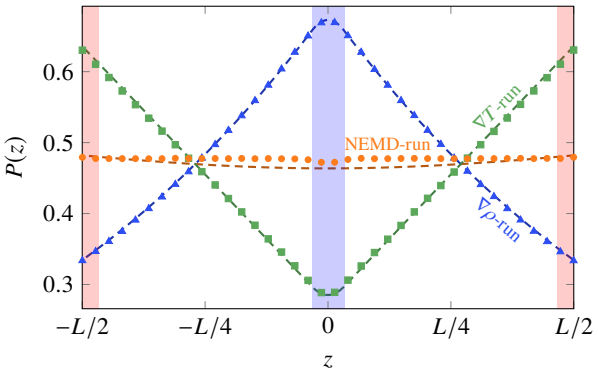

Figure D.4: Pressure measured in simulation (symbols) for an off-centre LJ system with $\overline{T} = 1.25$, $\overline{\rho} = 0.65$, $|\mathrm{d}T/\mathrm{d}z| = 0.009$ and $|\mathrm{d}\rho/\mathrm{d}z| = 0.004$, alongside the predicted pressure using the Johnson EOS (dashed lines). Symbols are larger than error bars.

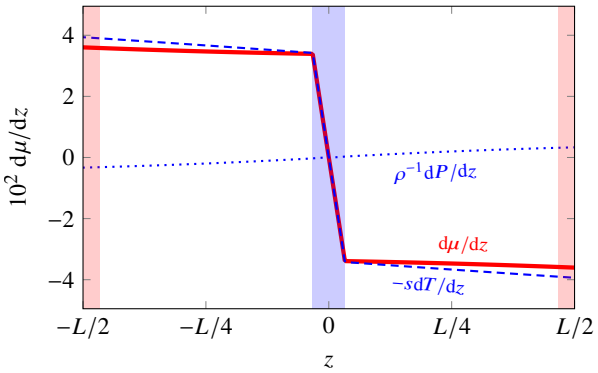

Figure D.5: Chemical potential (solid line) and its individual contributions (dashed and dotted lines) computed using the Johnson EOS for the NEMD-run shown in Fig. D.4.

the pressure for the NEMD-run. Although the simulation result clearly shows that the pressure is constant throughout the domain, the EOS predicts a small pressure gradient. Compared to the pressure gradients observed in the $\nabla\rho$- and ∇T-runs, however, this error is small, so that we consider the quality of agreement reasonable.

Finally, we demonstrate that the NEMD-run exhibits a gradient in the chemical potential. For a system in mechanical and local equilibrium, we expect the gradient in the chemical potential to be given by [Eq. (D.3)]

$$\frac{\mathrm{d}\mu}{\mathrm{d}z} = -s\frac{\mathrm{d}T}{\mathrm{d}z}. \tag{D.15}$$

Figure D.5 shows that, apart from the small erroneously predicted pressure gradient (Fig. D.4), this is indeed the case for the NEMD-run. This system therefore exhibits a gradient in the chemical potential while the pressure is approximately constant.

References

[1] C. F. W. Ludwig, Sitzungsber. Akad. Wiss. Wien, Math.-Naturwiss. Kl. **20**, 539 (1856).

[2] C. Soret, Arch. Sci. Phys. Nat. **2**, 48 (1879).

[3] S. R. de Groot and P. Mazur, *Non-equilibrium thermodynamics* (Dover Publications, New York, 1984).

[4] S. Duhr and D. Braun, Proc. Natl. Acad. Sci. U. S. A. **103**, 19678 (2006).

[5] S. J. Ebbens and J. R. Howse, Soft Matter **6**, 726 (2010).

[6] A. Würger, Rep. Prog. Phys. **73**, 126601 (2010).

[7] D. Frenkel and B. Smit, *Understanding Molecular Simulation*, 2nd ed. (Academic Press, San Diego, 2002).

[8] H.-R. Jiang, N. Yoshinaga, and M. Sano, Phys. Rev. Lett. **105**, 268302 (2010).

[9] M. Yang, A. Wysocki, and M. Ripoll, Soft Matter **10**, 6208 (2014).

[10] T. Bickel, A. Majee, and A. Würger, Phys. Rev. E **88**, 012301 (2013).

[11] A. Ly, A. Majee, and A. Würger, arXiv , 1703.03281 (2017).

[12] A. Barreiro, R. Rurali, E. R. Hernández, J. Moser, T. Pichler, L. Forró, and A. Bachtold, Science **320**, 775 (2008).

[13] L. Bocquet and E. Charlaix, Chem. Soc. Rev. **39**, 1073 (2010).

[14] R. Ganti, Y. Liu, and D. Frenkel, Phys. Rev. Lett. **119**, 038002 (2017).

[15] A. O. Govorov, W. Zhang, T. Skeini, H. Richardson, J. Lee, and N. A. Kotov, Nanoscale Res. Lett. **1**, 84 (2006).

[16] A. O. Govorov and H. H. Richardson, Nano Today **2**, 30 (2007).

[17] G. Baffou and R. Quidant, Laser Photonics Rev. **7**, 171 (2013).

[18] P. Keblinski, S. R. Phillpot, S. U. S. Choi, and J. A. Eastman, Int. J. Heat Mass Transfer **45**, 855 (2002).

[19] J. A. Eastman, S. U. S. Choi, S. Li, W. Yu, and L. J. Thompson, Appl. Phys. Lett. **78**, 718 (2001).

[20] J. Garg, B. Poudel, M. Chiesa, J. B. Gordon, J. J. Ma, J. B. Wang, Z. F. Ren, Y. T. Kang, H. Ohtani, J. Nanda, G. H. McKinley, and G. Chen, J. Appl. Phys. **103**, 074301 (2008).

[21] R. Prasher, P. Bhattacharya, and P. E. Phelan, Phys. Rev. Lett. **94**, 025901 (2005).

[22] P. Keblinski, J. A. Eastman, and D. G. Cahill, Mater. Today **8**, 36 (2005).

[23] C. Kleinstreuer and Y. Feng, Nanoscale Res. Lett. **6**, 229 (2011).

[24] L. E. Bell, Science **321**, 1457 (2008).

[25] A. Würger, Phys. Rev. Lett. **101**, 108302 (2008).

[26] F. Bresme, A. Lervik, D. Bedeaux, and S. Kjelstrup, Phys. Rev. Lett. **101**, 020602 (2008).

[27] A. Majee and A. Würger, Phys. Rev. Lett. **108**, 118301 (2012).

[28] J. A. Armstrong and F. Bresme, J. Chem. Phys. **139**, 014504 (2013).

[29] A. Majee and A. Würger, Soft Matter **9**, 2145 (2013).

[30] A. A. Lee, Soft Matter **12**, 8661 (2016).

[31] F. Römer, F. Bresme, J. Muscatello, D. Bedeaux, and J. M. Rubí, Phys. Rev. Lett. **108**, 105901 (2012).

[32] J. Muscatello, F. Römer, J. Sala, and F. Bresme, Phys. Chem. Chem. Phys. **13**, 19970 (2011).

[33] C. D. Daub, P.-O. Åstrand, and F. Bresme, Phys. Chem. Chem. Phys. **16**, 22097 (2014).

[34] C. D. Daub, P.-O. Åstrand, and F. Bresme, Mol. Phys. **114**, 3249 (2016).

[35] J. Armstrong and F. Bresme, Phys. Rev. E **92**, 060103 (2015).

[36] P. Wirnsberger, D. Fijan, A. Šarić, M. Neumann, C. Dellago, and D. Frenkel, J. Chem. Phys. **144**, 224102 (2016).

[37] P. Wirnsberger, D. Fijan, R. A. Lightwood, A. Šarić, C. Dellago, and D. Frenkel, Proc. Natl. Acad. Sci. U. S. A. **114**, 4911 (2017).

[38] D. Frenkel, J. Phys. Chem. B **120**, 5987 (2016).

[39] P. Wirnsberger, D. Frenkel, and C. Dellago, J. Chem. Phys. **143**, 124104 (2015).

[40] D. J. Evans and W. G. Hoover, Annu. Rev. Fluid Mech. **18**, 243 (1986).

[41] R. Kubo, J. Phys. Soc. Jpn. **12**, 570 (1957).

[42] D. J. Evans, Phys. Lett. A **91**, 457 (1982).

[43] W. T. Ashurst, in *Advances in Thermal Conductivity: 13th International Conference on Thermal Conductivity, Lake Ozark, Nov. 1973, Papers* (University of Missouri-Rolla, Rolla, MO, 1976) pp. 89–98.

[44] A. Baranyai, Phys. Rev. E **54**, 6911 (1996).

[45] G. Ciccotti and A. Tenenbaum, J. Stat. Phys. **23**, 767 (1980).

[46] T. Ikeshoji and B. Hafskjold, Mol. Phys. **81**, 251 (1994).

[47] F. Müller-Plathe, J. Chem. Phys. **106**, 6082 (1997).

[48] S. Kuang and J. D. Gezelter, J. Chem. Phys. **133**, 164101 (2010).

[49] S. Kuang and J. D. Gezelter, Mol. Phys. **110**, 691 (2012).

[50] B. Hafskjold, T. Ikeshoji, and S. K. Ratkje, Mol. Phys. **80**, 1389 (1993).

[51] F. Bresme, B. Hafskjold, and I. Wold, J. Phys. Chem. **100**, 1879 (1996).

[52] M. Bugel and G. Galliero, Chem. Phys. **352**, 249 (2008).

[53] S. Aubry, D. J. Bammann, J. J. Hoyt, R. E. Jones, C. J. Kimmer, P. A. Klein, G. J. Wagner, E. B. Webb III, and J. A. Zimmerman, "A robust, coupled approach for atomistic-continuum simulation," Tech. Rep. (Sandia National Laboratories, 2004).

[54] S. Plimpton, J. Comput. Phys. **117**, 1 (1995).

[55] S. Toxvaerd and J. C. Dyre, J. Chem. Phys. **134**, 081102 (2011).

[56] S. Nosé, J. Chem. Phys. **81**, 511 (1984).

[57] W. G. Hoover, Phys. Rev. A **31**, 1695 (1985).

[58] M. Tuckerman, B. J. Berne, and G. J. Martyna, J. Chem. Phys. **97**, 1990 (1992).

[59] G. Strang, SIAM J. Numer. Anal. **5**, 506 (1968).

[60] R. J. LeVeque and J. Oliger, Math. Comput. **40**, 469 (1983).

[61] H. J. C. Berendsen, J. R. Grigera, and T. P. Straatsma, J. Phys. Chem. **91**, 6269 (1987).

[62] J.-P. Ryckaert, G. Ciccotti, and H. J. C. Berendsen, J. Comput. Phys. **23**, 327 (1977).

[63] H. C. Andersen, J. Comput. Phys. **52**, 24 (1983).

[64] J. Armstrong, A. Lervik, and F. Bresme, J. Phys. Chem. B **117**, 14817 (2013).

[65] P. P. Ewald, Ann. Phys. **369**, 253 (1921).

[66] C. J. Fennell and J. D. Gezelter, J. Chem. Phys. **124**, 234104 (2006).

[67] D. Wolf, P. Keblinski, S. R. Phillpot, and J. Eggebrecht, J. Chem. Phys. **110**, 8254 (1999).

[68] J. Armstrong, C. D. Daub, and F. Bresme, J. Chem. Phys. **143**, 036101 (2015).

[69] P. J. Steinbach and B. R. Brooks, J. Comput. Chem. **15**, 667 (1994).

[70] D. Zahn, B. Schilling, and S. M. Kast, J. Chem. Phys. B **106**, 10725 (2002).

[71] X. Wu and B. R. Brooks, J. Chem. Phys. **122**, 44107 (2005).

[72] V. H. Elvira and L. G. MacDowell, J. Chem. Phys. **141**, 164108 (2014).

[73] I. Fukuda, Y. Yonezawa, and H. Nakamura, J. Chem. Phys. **134**, 164107 (2011).

[74] I. Fukuda, J. Chem. Phys. **139**, 174107 (2013).

[75] M. Lamichhane, J. D. Gezelter, and K. E. Newman, J. Chem. Phys. **141**, 134109 (2014).

[76] Y.-G. Chen and J. D. Weeks, Proc. Natl. Acad. Sci. U. S. A. **103**, 7560 (2006).

[77] G. S. Fanourgakis, J. Phys. Chem. B **119**, 1974 (2015).

[78] T. Darden, D. York, and L. Pedersen, J. Chem. Phys. **98**, 10089 (1993).

[79] M. Deserno and C. Holm, J. Chem. Phys. **109**, 7678 (1998).

[80] M. Neumann and O. Steinhauser, Mol. Phys. **39**, 437 (1980).

[81] H. Schreiber and O. Steinhauser, Biochemistry **31**, 5856 (1992).

[82] S. E. Feller, R. W. Pastor, A. Rojnuckarin, S. Bogusz, and B. R. Brooks, J. Phys. Chem. **100**, 17011 (1996).

[83] J. M. Rodgers and J. D. Weeks, Proc. Natl. Acad. Sci. U. S. A. **105**, 19136 (2008).

[84] E. Spohr, J. Chem. Phys. **107**, 6342 (1997).

[85] D. van der Spoel and P. J. van Maaren, J. Chem. Theory Comput. **2**, 1 (2006).

[86] G. A. Cisneros, M. Karttunen, P. Ren, and C. Sagui, Chem. Rev. **114**, 779 (2014).

[87] J. Muscatello and F. Bresme, J. Chem. Phys. **135**, 234111 (2011).

[88] F. Noé Mendoza, J. López-Lemus, G. A. Chapela, and J. Alejandre, J. Chem. Phys. **129**, 024706 (2008).

[89] K. Z. Takahashi, T. Narumi, and K. Yasuoka, J. Chem. Phys. **134**, 174112 (2011).

[90] J. M. Rodgers and J. D. Weeks, J. Phys.: Condens. Matter **20**, 494206 (2008).

[91] S. W. de Leeuw, J. W. Perram, and E. R. Smith, Proc. R. Soc. London, Ser. A **373**, 27 (1980).

[92] M. Neumann, O. Steinhauser, and G. S. Pawley, Mol. Phys. **52**, 97 (1984).

[93] C. D. Wick, L. X. Dang, and P. Jungwirth, J. Chem. Phys. **125**, 024706 (2006).

[94] M. A. Wilson, A. Pohorille, and L. R. Pratt, J. Chem. Phys. **88**, 3281 (1988).

[95] I.-C. Yeh and M. L. Berkowitz, J. Chem. Phys. **111**, 3155 (1999).

[96] J. N. Glosli and M. R. Philpott, Electrochim. Acta **41**, 2145 (1996).

[97] G. Hummer, L. R. Pratt, A. E. García, and M. Neumann, AIP Conf. Proc. **492**, 84 (1999).

[98] G. Hummer, N. Grønbech-Jensen, and M. Neumann, J. Chem. Phys. **109**, 2791 (1998).

[99] M. A. Wilson, A. Pohorille, and L. R. Pratt, J. Chem. Phys. **90**, 5211 (1989).

[100] W. Smith, CCP5 Newsl. **46**, 18 (1998).

[101] J. D. Jackson, *Classical electrodynamics*, 3rd ed. (Wiley, 1998).

[102] N. A. Spaldin, J. Solid State Chem. **195**, 2 (2012).

[103] W. C. Swope, H. C. Andersen, P. H. Berens, and K. R. Wilson, J. Chem. Phys. **76**, 637 (1982).

[104] I.-C. Yeh and A. Wallqvist, J. Chem. Phys. **134**, 055109 (2011).

[105] M. Neumann, Mol. Phys. **57**, 97 (1986).

[106] C. J. F. Böttcher, *Dielectrics in static fields*, 2nd ed. (Elsevier Science, 1973).

[107] V. P. Sokhan and D. J. Tildesley, Mol. Phys. **92**, 625 (1997).

[108] M. Stengel, N. A. Spaldin, and D. Vanderbilt, Nat. Phys. **5**, 304 (2008).

[109] C. Zhang and M. Sprik, Phys. Rev. B **93**, 144201 (2016).

[110] W. H. Stockmayer, J. Chem. Phys. **9**, 398 (1941).

[111] I. Iriarte-Carretero, M. A. Gonzalez, J. Armstrong, F. Fernandez-Alonso, and F. Bresme, Phys. Chem. Chem. Phys. **18**, 19894 (2016).

[112] Z. Wang and C. Holm, J. Chem. Phys. **115**, 6351 (2001).

[113] C. Kriebel, A. Müller, J. Winkelmann, and J. Fischer, Fluid Ph. Equilibria **119**, 67 (1996).

[114] J. J. Weis and D. Levesque, Phys. Rev. E **48**, 3728 (1993).

[115] G. Stell, J. C. Rasaiah, and H. Narang, Mol. Phys. **23**, 393 (1972).

[116] J. K. Johnson, J. A. Zollweg, and K. E. Gubbins, Mol. Sim. **78**, 591 (1993).

[117] M. Thol, G. Rutkai, A. Köster, R. Lustig, R. Span, and J. Vrabec, J. Phys. Chem. Ref. Data **45**, 023101 (2016).

[118] M. Neumann, J. Chem. Phys. **85**, 1567 (1986).

[119] A. P. Thompson, S. J. Plimpton, and W. Mattson, J. Chem. Phys. **131**, 154107 (2009).

[120] D. M. Heyes, Phys. Rev. B **49**, 755 (1994).

[121] J. Sonne, F. Y. Hansen, and G. H. Peters, J. Chem. Phys. **122**, 124903 (2005).

[122] T. W. Sirk, S. Moore, and E. F. Brown, J. Chem. Phys. **138**, 064505 (2013).

[123] A. Toukmaji, C. Sagui, J. Board, and T. Darden, J. Chem. Phys. **113**, 10913 (2000).

[124] L. Bocquet, E. Trizac, and M. Aubouy, J. Chem. Phys. **117**, 8138 (2002).

[125] Y. Monovoukas and A. P. Gast, J. Colloid Interface Sci. **128**, 533 (1989).